STATIC AND DYNAMIC DEFORMATION BEHAVIOR OF COMBINED GEOMETRY AISI 304L STAINLESS STELL SHELLS

A Thesis Submitted to
the Graduate School of Engineering and Sciences of
İzmir Institute of Technology
in Partial Fulfillment of the Requirements for the Degree of

MASTER OF SCIENCE

in Mechanical Engineering

by
Selim ŞAHİN

July 2015
İZMİR

We approve the thesis of **Selim ŞAHİN**

Examining Committee Members:

Assoc. Prof. Dr. Alper TAŞDEMİRCİ
Department of Mechanical Engineering, İzmir Institute of Technology

Assoc. Prof. Dr. Buket OKUTAN BABA
Department of Mechanical Engineering, Celal Bayar University

Assist. Prof. Dr. H. Seçil ARTEM
Department of Mechanical Engineering, İzmir Institute of Technology

9 July 2015

Assoc. Prof. Dr. Alper TAŞDEMİRCİ
Supervisor, Department of
Mechanical Engineering
İzmir Institute of Technology

Prof. Dr. Mustafa GÜDEN
Co-Supervisor, Department of
Mechanical Engineering
İzmir Institute of Technology

Prof. Dr. Metin TANOĞLU
Head of the Department of
Mechanical Engineering

Prof. Dr. Bilge KARAÇALI
Dean of the Graduate School of
Engineering and Sciences

ACKNOWLEDGEMENTS

First of all I would like to thank to my supervisor Assoc. Professor Alper TAŞDEMİRCİ for giving me the chance of being a member of his research team in Dynamic Testing and Modeling Laboratory. I also thank to my supervisor for his instructive comments, guidance and supports throughout my thesis study.

I thank to my co-supervisor Professor Mustafa GÜDEN for his help and supporting ideas during my thesis study.

I would also like to thank to The Scientific and Technological Research Council of Turkey (TUBITAK) for financially supporting 112M141 project.

Thanks to all members of DTM lab; Ali KARA, Kıvanç TURAN, Kutlay ODACI, Atacan YÜCESOY, Fulya AKBULUT for their endless support and collaboration during my working period.

Finally, I would like to thank my family; my father Yıldız ŞAHİN, my mother Sadiye ŞAHİN and my brother Serhat ŞAHİN for their financial and moral supports. I specially thank to my fiancée Selin ERGÜL for her patience, support and endless love during this hard working period. I also thank to my mother Emine ERGÜL for her support and love. I thank to everyone who helped me during my thesis study, without your supports this study would have never been finished.

ABSTRACT

STATIC AND DYNAMIC DEFORMATION BEHAVIOR OF COMBINED GEOMETRY AISI 304L STAINLESS STEEL SHELLS

In this study, the static and dynamic crushing behavior of combined geometry shells consisting of hemi-spherical and cylindrical segments were studied both experimentally and numerically. The proposed geometries were manufactured by deep drawing. Due to the nature of the deep drawing process, specimens inherited significant amount of residual stress/strain and thickness variation along the cross-section was observed. Thus, the manufacturing process was also numerically modeled explicitly. Quasi-static compression and dynamic drop weight tests were conducted both experimentally and numerically. The plastic deformation of the combined geometry shells started with the inward dimpling of the hemi-spherical segment and progressively continued deforming with the asymmetric or axisymmetric folding in cylindrical segment depending on the radius to thickness ratios and strain rates. The failure/fracture was observed in the thicker specimens at dynamic strain rates and that caused decreases in specific absorbing energy (SAE) levels. In addition, the energy partitions between the hemi-spherical segments increased at higher loading rates. Furthermore, the inertia and rate sensitivity influenced the crushing response of cylindrical segment more than that of hemi-spherical segment and inertia effect was more pronounced than the rate sensitivity at higher loading rates. Considering the thermal effects in the crushing behavior of the combined geometry shells, it was shown that the mean crushing load lowered as the temperature increased. Additionally, the percentages of increase in the crushing load were limited at lower temperatures for varying loading rates. It was shown that as the absolute temperature increased the percentage of increase in crushing load was significantly increased due to the change in deformation mode.

ÖZET

BİRLEŞİK GEOMETRİLİ AISI 304L PASLANMAZ ÇELİK KABUK YAPILARIN STATİK VE DİNAMİK DAVRANIŞLARI

Bu çalışmada, yarı küresel ve silindirik geometriden meydana gelen kombine geometrili kabuk yapıların ezilme davranışları deneysel ve nümerik olarak incelenmiştir. Söz konusu geometriler derin çekme metodu kullanılarak elde edilmiştir. Derin çekme işleminin doğasından dolayı, numuneler üzerinde artık gerilme/gerinim ve kesit alanı boyunca kalınlık değişimi gözlemlenmiştir. Bu sebeple üretim prosesi de nümerik olarak ayrıca modellenmiştir. Statik ezilme ve dinamik düşen ağırlık testleri deneysel ve nümerik olarak gerçekleştirilmiştir. Kombine geometrili kabuk yapılar plastik deformasyonlarına yarı-küresel bölgelerinin içe doğru çukurlaşması ile başlamaktadır ve sonrasında yarıçapın kalınlığa oranına ve şekil değiştirme hızına bağlı olarak silindrik bölgelerinde asimetrik veya eksenel simetrik katlanma yaparak deformasyonunu sürdürmektedir. Dinamik şekil değiştirme hızlarında kalın numunelerin üzerinde kırılmalar görülmektedir ve bu numunelerin özgül enerji emme kapasitesinde azalmaya sebep olmaktadır. Buna ek olarak, numunelerin yarı-küresel bölgelerinin enerji emilimine katılımları yüksek yükleme hızlarında artmaktadır. Buna ek olarak, atalet ve şekil değiştirme hızı hassasiyetinin silindirik bölgelerin ezilme tepkilerine yarı-küresel bölgelere nazaran daha etkili olduğu görülmektedir ve yüksek deformasyon hızlarında atalet etkisinin şekil değiştirme hızı hassasiyetine göre daha baskın olduğu bulunmuştur. Sıcaklığın, kombine geometrili kabuk yapıların ezilme davranışlarına etkisi düşünüldüğünde, ortalama kuvvet değerinin sıcaklığın artması ile azaldığı görülmüştür. Ayrıca, ezilme kuvvetinin yüzdelik artışı düşük sıcaklık değerlerinde değişen yükleme hızları için sınırlıdır. Mutlak sıcaklığın artması ile ezilme kuvvetinin yüzdelik artışı deformasyon modunun değişmesinden dolayı önemli ölçüde artmaktadır.

TABLE OF CONTENTS

LIST OF FIGURES

LIST OF TABLES

Table **Page**

CHAPTER 1

INTRODUCTION

1.1. Energy Absorbing Structures

Energy absorbing structures are widely used in many applications such as aerospace, automotive, defense industries and industrial machines. The fundamental principles of energy absorbing structure are to minimize transmitted force and convert the kinetic energy into irreversible strain energy with progressively large deformation. Utilization of the energy absorbing structures have been improving as the needs of modern world rising. As the technology improves, demands for the application area of the energy absorbing structure has been expanding, as well. For instance, today there have been lots of terrible traffic accidents resulting in many death or injuries. Furthermore, as the weapon technology improves, development of armor systems is unavoidable in order to protect civilians. Using of energy absorbing structures requires engineering approaches to obtain optimum values for transmitted force or acceleration histories. Energy absorbing structures can be made of various base materials. Metals and composite with or without foam filling are used to obtain thin walled structures for the energy absorption. Additionally, honeycombs, foams and balsa wood are used as cellular materials for the same purpose. Polymer matrix composites are utilized to absorb energy having high stiffness/weight ratio in many structures. The first groups consisting metals and composites are commonly used having high perimeter to thickness ratio as a common feature of thin-walled structures. Furthermore, sandwich structures consist of two components. The first is the low density core material and the other one is the high density face skins; can be composites or metals. Balsa wood, honeycomb and foam can be utilized as low density core material of sandwich structures and truss, web and corrugated structural geometries can generally be used in sandwich structures, as well. Sandwich structures are generally used in energy absorption applications due to their aforementioned features.

The crushing response of structures is very important and must be determined to evaluate their energy absorption capability. The main aim is to absorb adequate energy by transmitting minimum force with desired weight.

Many structures used as energy absorbing structures were offered in the literature. The crushing behavior of thin walled structures is influenced by its material properties, applied force/deformation rate and especially geometry. Utilizing different geometrical shape with using same material can result in different crushing behavior. Thus, there are lots of experiments and studies for different geometries. The examples of that may include square, cylindrical, cone, spherical and combination of them. The crushing of tube differs for lateral and combined loading conditions. The radius to thickness ratio can affect both deformation mode and the history of load carrying capacity. In addition to this, application of square or cone shape geometries as used in automobile crash boxes increase in automotive industry to absorb energy efficiently in case of accidents. The crushing responses of square or cone geometry are function of their geometrical parameters such as semi apical angle, and the height to thickness ratio. The spherical geometries are also widely used in civil engineering applications, pressure vessels, and fuel tanks. The radius, thickness and height are also fundamental geometrical parameters affecting on the crushing load of the structure.

There are a lot of researches carried on crushing behavior of tubes having different cross section with different number of edges. It was shown in the literature that collapse of tubes having even number of edges was more regular than tubes having odd number of edges (Zhang and Huh 2010). In another study, multi-cell tubes with triangular and Kagome lattices (Figure 1.1) were investigated analytically and numerically in terms of their energy absorption. The absorbed energy increased as the thickness of cell walls decreased with increasing in number of fold formation. (Hong et al. 2014).

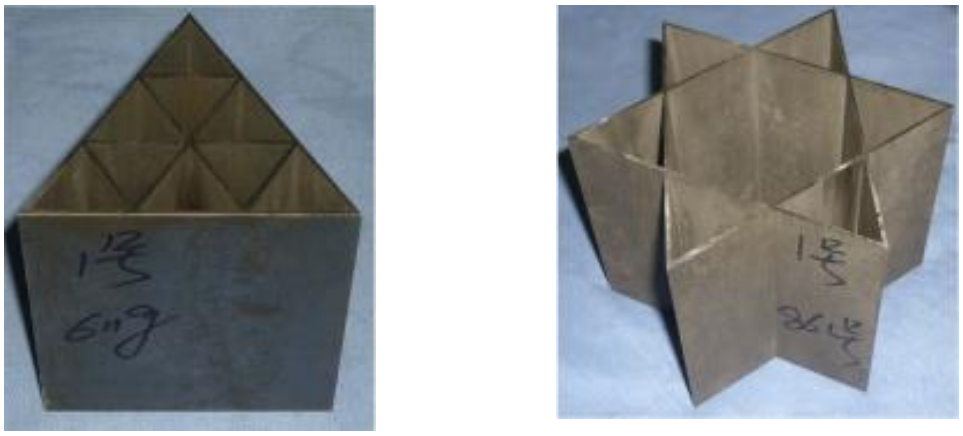

(a) (b)

Figure 1.1. Multi-cell tube with (a) triangular, (b) Kagome lattices
(Source: Hong et al. 2014)

Thin-walled structures can be made of cellular materials. The dynamic crushing behavior of the conical tubes filled with foam was investigated in terms of wall thickness, apical angle and impact velocity. It was reported that the higher foam density, wall thickness and apical angle resulted an increase in mean crushing force (Ahmad and Thambiratnam 2009). In addition, the crushing response of the foam-filled aluminum tube was studied at static and dynamic strain rates and it was presented that as the foam density increased, the compressive loading capacity increased. (Duarte et al. 2015). Furthermore, the energy absorbing capability of single, double and multi-wall square and circular cross sectional tubes were studied with and without including aluminum foam and it was represented that the foam-filled tube and double, multi-wall tubes both square and cylinders have higher energy absorbing capability. The circular cross sectional tubes were higher energy absorbing capability than the square cross sectional tubes (Goel 2015).

The utilization of the composite material has been increasing day by day due to their high stiffness/weight ratio and anisotropy. There are lots of applications of composite material as energy absorbing structures in the literature. The square cross sectional (Mamalis et al. 2006), cylindrical (Abosbaia et al. 2003, Abosbaia et al. 2005, Guden et al. 2007) and conical (Alkateb et al. 2004, Mahdi et al. 2006, Obradovic, Boria, and Belingardi 2012, Kathiresan, Manisekar, and Manikandan 2014) geometry shells were researched. The crashworthiness of composite conical tubes was studied in terms of ply orientation, thickness and semi-apical angle. It was reported that the energy absorption capacity increased as semi-apical angle increased (Kathiresan, Manisekar, and

Manikandan 2014). In addition, the crushing behavior of tubes made of different composite material (segmented and non-segmented) was studied for in-plane and laterally loading. It was represented the segmented composite tubes were better than the non-segmented composite tubes for energy absorption capacity and load-carrying capacity (Abosbaia et al. 2003, Abosbaia et al. 2005). The elliptical cross sectional conical composite tubes were studied with varying semi-apical angles. It was reported that the average crushing force increased as the semi-apical angle increased. The failure mode changed for different semi-apical angles, Figure 1.2 (Alkateb et al. 2004).

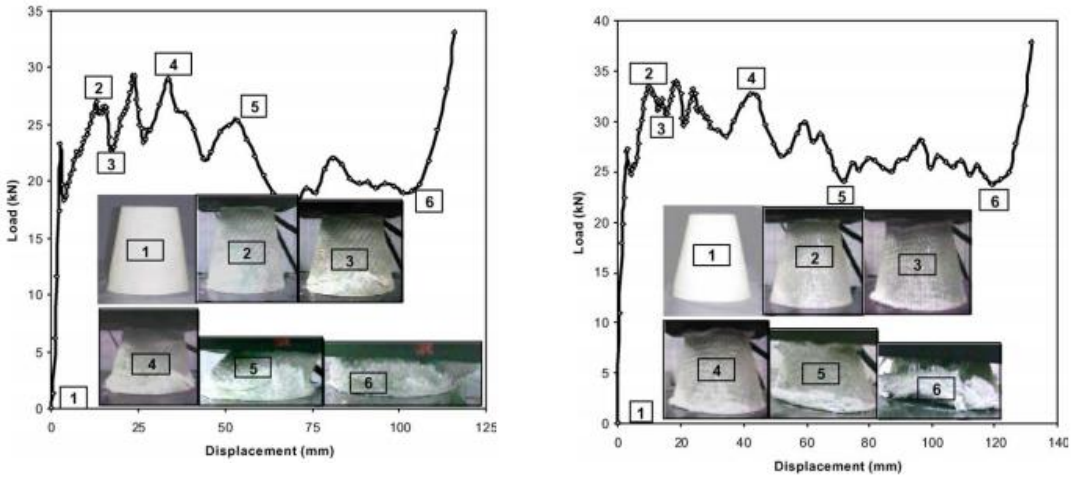

(a) (b)

Figure 1.2. Deformation histories of axially loaded elliptical cone with apical angle of (a) 18°, and (b) 24° (Source: Alkateb et al. 2004)

The crushing behavior of composite tube filled with aluminum closed cell foam and thin-walled hybrid aluminum tube filled with polyester was studied. It was presented that foam filled composite tubes deformed progressively. Additionally, the load carrying capacity of aluminum/composite tube was higher than the sum of empty aluminum tube and empty composite tube due to the interaction effect, Figure 1.3, (Guden et al. 2007). Moreover, the complex geometry composite tubes were utilized as a crush box in automotive industry (Obradovic, Boria, and Belingardi 2012).

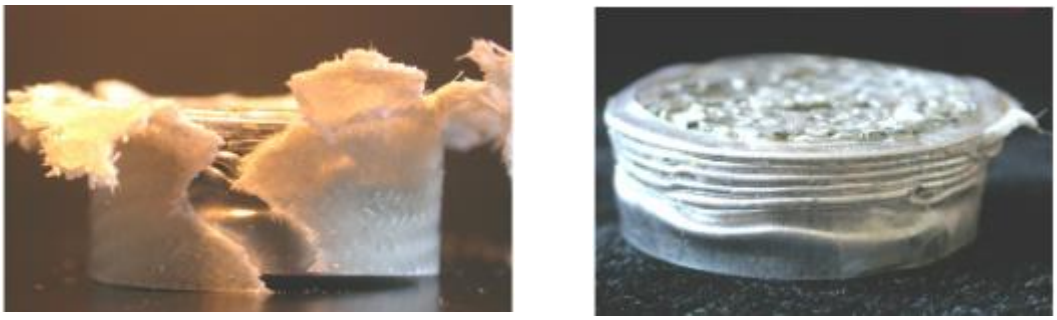

(a) (b)

Figure 1.3. Image of (a) a crushed foam-filled hybrid tube and (b) folding of Al tube in foam-filled hybrid tube (Source: Guden et al. 2007).

There are lots of investigations in lattice core sandwich structures subjected to static and dynamic loading. It was reported that the pyramidal lattice core presented progressive buckling during collapse (Wadley et al. 2008) and their deformation behavior changed at different strain rates due to the micro inertia effects (Lee et al. 2006). Furthermore, the effect of foam filling in pyramidal lattice core was studied and it was concluded that the load carrying capacity of foam filled pyramidal lattice was higher than the sum of only lattice and foam. However, the utilizing of lattice core filling with foam was ineffective way at lower strain rates in terms of specific absorption energy due to the increase in mass (Zhang et al. 2014). The impact strength of tetrahedral lattice truss made of rate insensitive material was studied at static and dynamic strain rates and it was resulted that micro inertia caused different crushing forces (Liu et al. 2014). The effects of having number of cells and the angle between edges were examined for honeycomb structures at static and dynamic strain rates (Zhang, Zhang, and Wen 2014). The collapse of trapezoidal aluminum corrugated core sandwich structure was studied experimentally and numerically at static and dynamic strain rates. The increase in buckling stress resulted from increase in bending force due to the micro inertia effect (Kılıçaslan et al. 2014). The mechanical behavior of the cellular materials was researched in the literature. The ballistic performance of aluminum and Teflon foam interlayer implemented in the composite armor was investigated experimentally and numerically. It was reported that using of Teflon and aluminum foam resulted decrease in transmitted stress to backing plate with a sufficient delay (Tasdemirci, Tunusoglu, and Güden 2012). In addition , strain rate dependency of the Teflon foam was found to be significant (Tasdemirci, Turan, and Guden 2012). Balsa and Teflon foam core were implemented in the composite sandwich

structures and the energy absorbing capacity were investigated with varying impact energies (Atas and Sevim 2010).

Figure 1.4. The deformed radome of aircraft due to internal structural failure (Source: Welbes 2008).

Moreover, energy absorbing capacity of thin walled structure consisting of different geometric types has to be considered. New type geometry is simply called combined geometry. They can resist to applied force by deforming with combination of their crushing behaviors of geometries. In many applications, the combined geometry which consists of spherical, conical or cylindrical geometric shape can be used in rocket warhead, radome of aircraft, fuel tank, projectiles and crush boxes. The combined geometry has a good crushing behavior at various strain rates due to their progressive buckling without any discontinuity and representing various deformation types of their different geometric segments. The combined geometry consisting of spherical and cone segments can be good example as can be seen in Figure 1.4 (radome in aerospace application). The investigation of crushing behavior at static and dynamic strain rates is necessary for design criteria in order to apply in new energy absorbing structures.

Structures should be designed in ideal according to their purpose. However, the manufacturing method influences the crushing behavior of structure. In this study, the specimens were manufactured by deep drawing at first. In order to examine the crushing

response of proposed geometries in detail, the manufacturing effects on the crashworthiness should be studied.

1.2. Aim and Scope of the Study

Thin-walled structures especially cylindrical, spherical and conical geometries are widely used as energy absorbing structures due to the high energy absorbing efficiency. There have been many studies about crushing phenomenon of these kinds of geometries. However, the investigation of crushing behavior of the combination of cylindrical, spherical or conical geometries is limited in literature. That the combined geometries present superior energy absorption characteristics than those of their constituents procreates new research areas.

In this thesis, the static and dynamic crushing behavior of AISI 304L stainless steel of combined geometry shells consisting of spherical and cylindrical portions were investigated with varying ratios of radius to thickness at different strain rates both experimentally and numerically. The energy absorbing capacity of combined geometry shells was also determined experimentally and numerically at static and dynamic strain rates.

The specimens were manufactured by deep drawing. Thus, there was significant amount of residual stress and strain and also a thickness variation occurred through the cross sections of the specimen. For these reasons, the manufacturing route was needed to be explicitly modeled throughout the study.

The thesis enclosed the main chapters as following. Some examples of energy absorbing structure were briefly explained in the first chapter. The second chapter includes the literature survey about crushing behavior of varying geometry of thin walled structure in particular cylindrical, spherical and combined geometry shells. Furthermore, the influence of manufacturing process on the crushing response of the structure was given with data from the literature. In the third chapter, the manufacturing and the testing of proposed combined geometry shells were explained in detail. The details of numerical approach for both manufacturing and crushing simulations at low and high strain rates of specimens were given simultaneously in chapter fourth. In the fifth chapter, the crushing behavior of combined geometries was presented. In addition, inertia and rate sensitivity

effects and crushing responses at different thermal conditions were also examined in detail. Subsequently the conclusions and the future work were given.

CHAPTER 2

LITERATURE SURVEY

2.1. Static and Dynamic Crushing Behavior of Thin Walled Structures

Thin walled structures are widely used due to their low cost and high energy absorbing capacity in several industrial areas. The improved energy absorbing capacities of thin walled structures through experimental, analytical and numerical studies have made them attractive for many industrial applications. In order to support the industry demand and academic research in this area, the crushing behavior of combined geometry shells consisted of hemispherical and cylindrical geometric segments were manufactured and their mechanical responses at static and dynamic loading cases were investigated both experimentally and numerically in this thesis study. The literature of thin walled structures related with this study can be divided into groups according to geometric aspects as follows.

2.1.1. Crushing Behavior of Cylindrical Geometry Shells

Karagiozova et al. investigated the axisymmetric deformation behavior of cylinder tubes subjected to axial impact and also explained the parameters effecting buckling response of cylindrical tubes. The dynamic plastic buckling of cylindrical tubes was mainly effected by the variation of speed of the plastic stress propagation due to strain hardening. High strain hardening modulus increases the tendency of buckle in the cylindrical tubes. The stress at the impact end of the tubes can be defined as a function of yield stress, strain hardening modulus and impact velocity using the Von Mises flow formula as depicted in Eqn. 2.1.

$$\mathbf{P_{I,max} = 2\pi Rh\left(\sigma_y + V_0\sqrt{\rho E_h}\right)^2/\sqrt{3}} \qquad (2.1)$$

Furthermore, increasing of impact velocity with constant kinetic energy reduced the total deformation of tube due to the axial compression due to the inertia effect. Thus,

the energy absorption of tube increased as the impact velocity increased. That resulted in higher energy absorption for smaller displacement. The deformation mode was affected by impact velocity, Figure 2.1. The total displacement decreased while the velocity increased due to the compressive deformation before the progressive plastic buckling. On the other hand, the mean crushing force decreased as impact masses increased for the same initial kinetic energy, Figure 2.1 (Karagiozova, Alves, and Jones 2000).

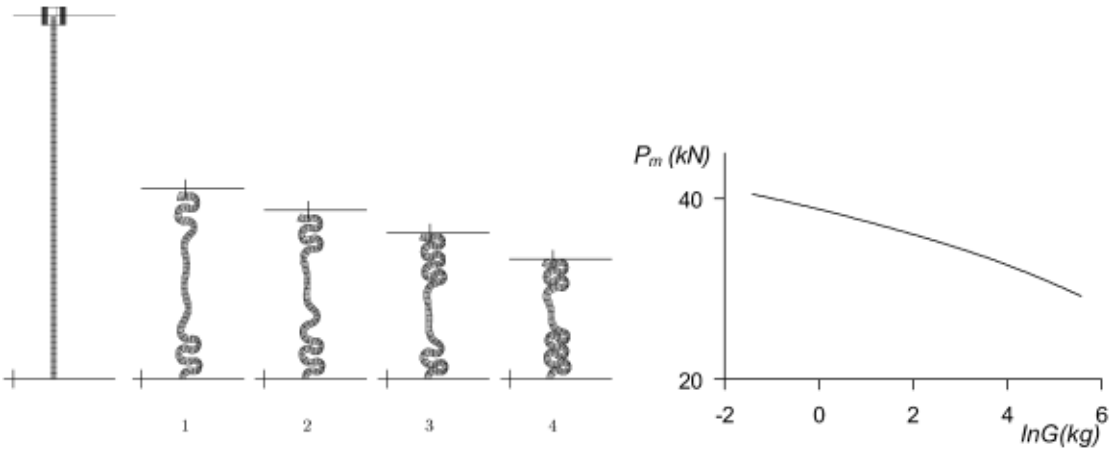

(a) (b)

Figure 2.1. Performance of shell S1 subjected to an impact energy of 2.1 kJ and different combinations of the striking mass and the impact velocity; (a) final buckling shapes, (b) Variation of the mean crushing force with the striking mass (Source: Karagiozova, Alves, and Jones 2000).

Singace and El-Sobky investigated the influence of different boundary conditions on the crushing response of mild steel and aluminum tube. The radial inward and outward constrains caused the concertina and diamond mode during collapse. It was reported that the initial peak in the load-displacement history was vanished in condition where the tube entirely constrained for each ends (Singace and El-Sobky 2001).

Al Galib and Limam studied the axially crashworthiness of thin walled circular aluminum tube at static and dynamic strain rates. Axisymmetric and mix mode were observed obviously even though the load and boundary condition were the same. It was presented that the initial peak of crushing response of tube was higher than the other peaks for axisymmetric deformation since the formation of subsequent peaks were affected by initial peak due to the initializing the local bending at the plastic hinges level. On the other hand the mixed mode resulted in asymmetric deformation with higher energy absorption capacity but, the axisymmetric deformation type was better than mixed mode due to providing progressive buckling even though energy absorption capacity was not

proper. It was found that the imperfection effected on the deformation mode and mean collapse load of collapse. (Al Galib and Limam 2004).

Tasdemirci worked on the crushing response of 3003-H14 aluminum tubes experimentally and numerically with various types of end constraining. It was presented that the concertina deformation mode was seen in free and single-end constraint tubes. The mixed/diamond mode of deformation was observed in case of fully inward double-end constraint tube. In addition, having of the double-end inward constraining induced decreasing in the average load values with increase in the displacement, Figure 2.2 (Tasdemirci 2008).

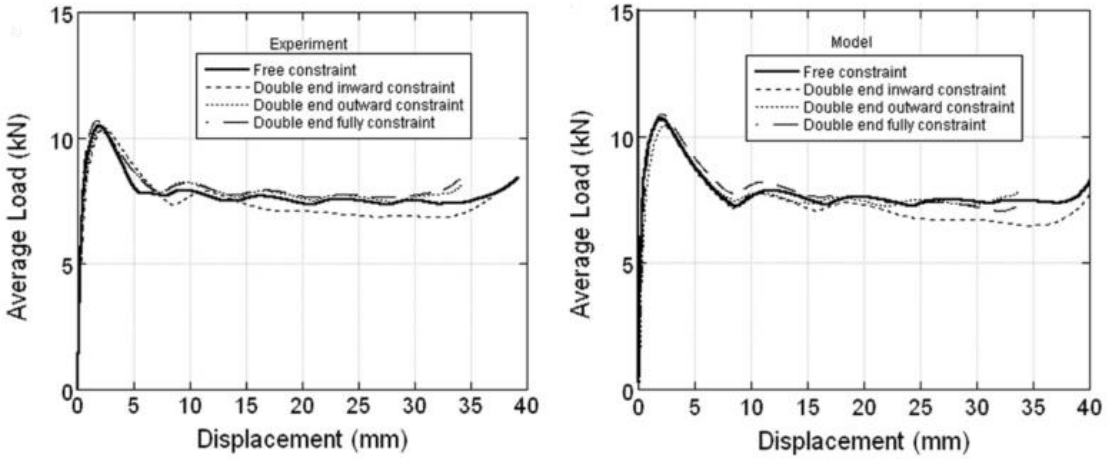

Figure 2.2. Average load vs. displacement curves of double-end constraint tubes for experiment and model (Source: Tasdemirci 2008).

Ghamarian and Abadi performed the static deformation of the end-capped thin walled aluminum tubes that were hallow or filled polyurethane foam. The dynamic crushing behavior was examined to evaluate dynamic amplification factor (*DAF*) which was the ratio of dynamic crushing force to static. It was reported that the density of foam affected on the crushing behavior of end-capped tube. Foam filling induced the lower *DAF* value than without foam filling, Figure 2.3. It resulted an insignificant increase in energy absorption.

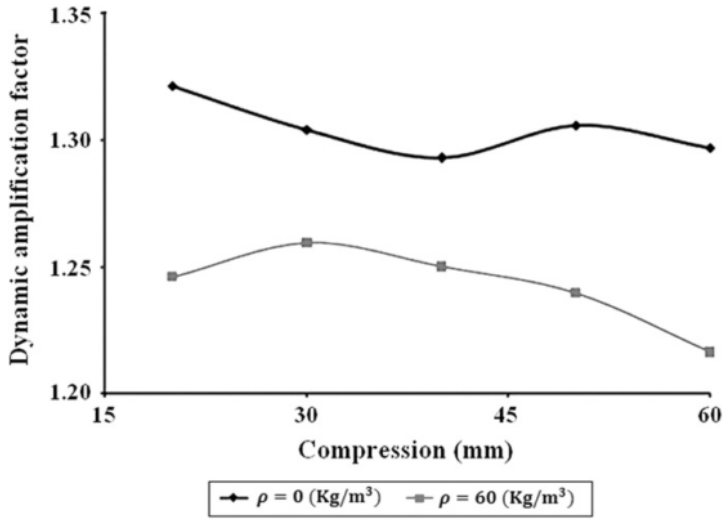

Figure 2.3. Comparison of dynamic amplification factor vs. crush distance for hollow and foam-filled tubes; t=1mm, D=49.8 mm, H=98.5 mm, V=20 m/s, m=20 kg (Source: Ghamarian and Abadi 2011).

It was also presented that using end-capped was an efficient way to decrease the initial peak in the load-displacement curves, Figure 2.4. Further the initial peak value was a function of radius of fillet and foam density (Ghamarian and Abadi 2011).

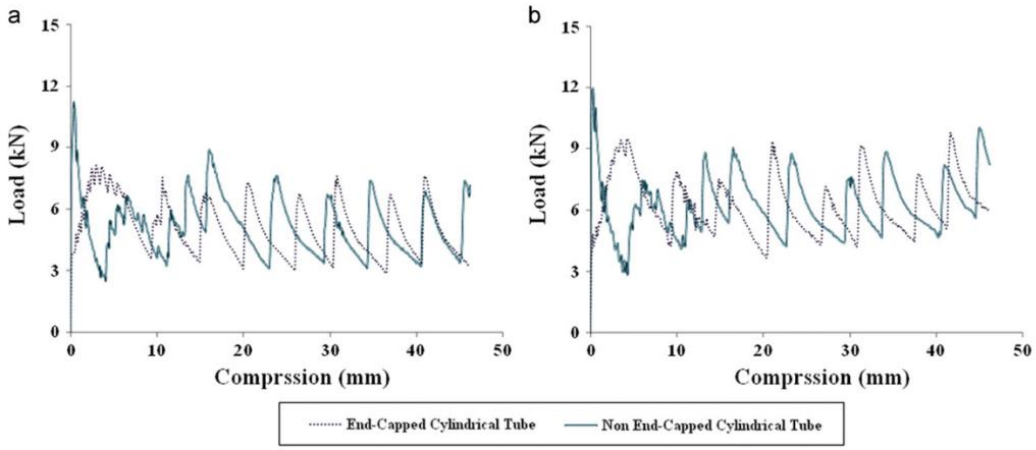

(a) (b)

Figure 2.4. Load–compression curves for end-capped and non-capped circular tubes for (a) hollow and (b) foam-filled tubes (Source: Ghamarian and Abadi 2011).

The energy absorption characteristic of tailor-made aluminum tube consisting of segments having different thickness along length was examined by Shahi and Marzbanrad analytically and numerically. The results suggested that the utilization of tailor-made tube was more convenient method thanks to higher energy absorption per unit weight than the

simple tube having constant thickness under the same condition. Moreover, the variation of thickness along the length revealed that the maximum crushing force that occurred at the end of the tube, Figure 2.5 (Shahi and Marzbanrad 2012).

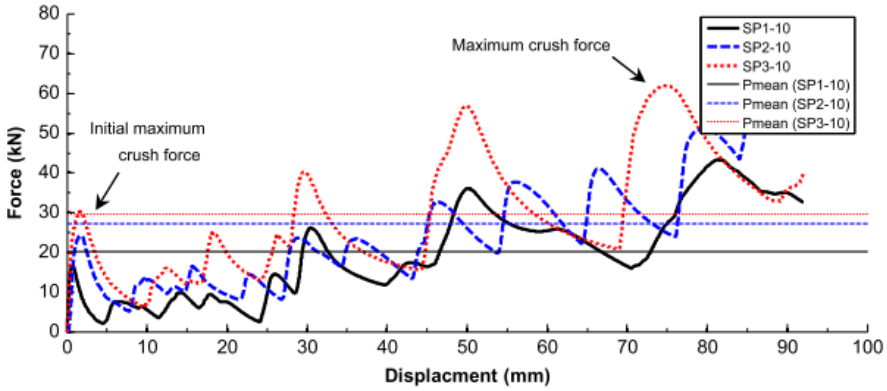

Figure 2.5. Typical force-displacement curves of tailor-made tubes (Source: Shahi and Marzbanrad 2012).

Higuchi et al. worked on the dynamic crushing behavior of thin walled aluminum circular tubes under impact loading. As can be seen in Figure 2.6, the total deformation of tube decreased as the velocity increased due to the increase in average load with constant kinetic energy.

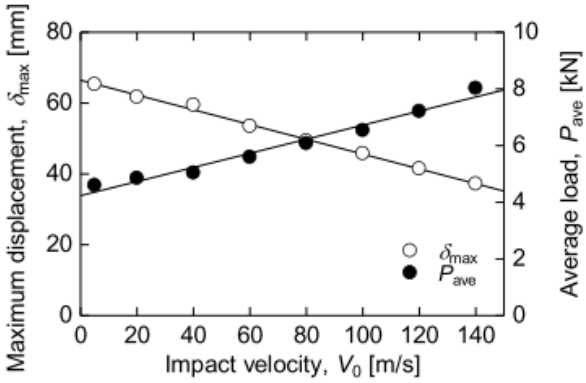

Figure 2.6. Relation between maximum displacement, average load, and initial impact velocity (Source: HIGUCHI et al. 2012).

The finite element code was applied in order to illustrate the reaction forces and the absorbing energies of fixed and impact ends. The results showed that the initial peak of impact end was significantly higher than the initial peak of fixed end. The increase in the force at impact side was theoretically estimated by Eqn. 2.1. Figure 2.7 represents the

peak and average forces with various loading velocities. Furthermore, the absorbed energy increased in bilinear shape as seen in Figure 2.8. That caused from the compressive deformation of tube. The bilinear form is obviously seen between 0 and 10 mm deformation at higher impact velocity. The crushing force of fixed end initialized with a time delay due to the propagation of elastic stress wave (HIGUCHI et al. 2012).

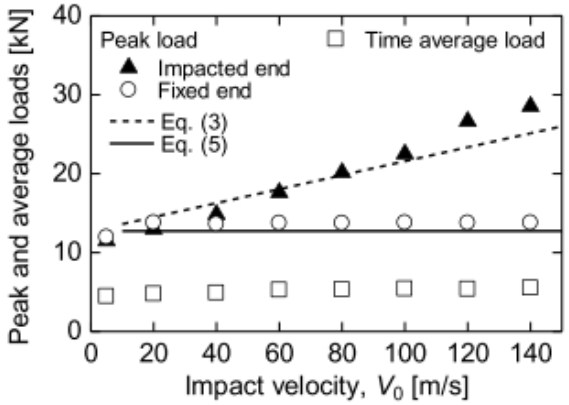

Figure 2.7. The histories of impulses at impacted and fixed ends for initial impact velocity, V_0 = 100 m/s (Source: HIGUCHI et al. 2012).

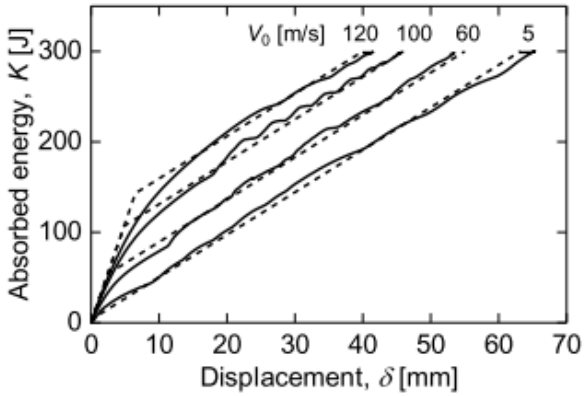

Figure 2.8. Absorbed energy-displacement curves in low-and high-velocity impacts (Source: HIGUCHI et al. 2012).

2.1.2. Crushing Behavior of Spherical Geometry Shells

The nature of buckling of spherical geometries has been researched analytically, experimentally and numerically for a long time. As technology improves, the analytical approaches, test methods and in particular numerical studies develops by scientist. The

fundamental effects on the crushing response of spherical geometry are represented from the literatures.

Updike studied the analytical approach of crushing behavior of spherical loading between two flat plates. The solution was valid one tenth the shell radius of distance between these plates and several tests were conducted in order to confirm the theory. According to study, the crushing force was not a function of spherical radius as can be seen in Eqn. 2.2. Further the absorbed energy by spherical shell was estimated by integrating the force with respect to displacement, Eqn. 2.3. Once the deformation mode changed to asymmetric from axisymmetric, the number of lobes was observed. This induced that the critical buckling load decreased to that of 5 percent of axisymmetric buckling load (Updike 1972).

$$\mathbf{P = 2\pi\sqrt{3}\sigma_0 t^{3/2}\Delta^{1/2}} \qquad (2.\ 2)$$

$$\boldsymbol{W = 7.26\sigma_0 t^{3/2}\Delta^{3/2}} \qquad (2.\ 3)$$

Where;

P = Load

σ_0 = Yield stress

t = Thickness of the shell

Δ = Displacement

Deoliveira and Wierzbicki worked on the mechanism of crushing response of spherical shells subjected to different loading types. In this research, the buckling load subjected to point loading was represented analytically as can be seen in Eqn. 2.4 and the crushing behavior of spherical shell between rigid platen was also analyzed as can be seen in Eqn. 2.5. (Deoliveira and Wierzbicki 1982).

$$\frac{\mathbf{P}}{\mathbf{2\pi M_0}} = \mathbf{2} + \left(\frac{\mathbf{14}}{\mathbf{45}}\right)\left(\frac{\mathbf{w}}{\mathbf{h}}\right)^{\mathbf{2}} \qquad (2.\ 4)$$

$$\frac{\mathbf{w}}{\mathbf{h}} = \left(\frac{\mathbf{1}}{\mathbf{43}}\right)\left(\frac{\mathbf{P}}{\mathbf{2\pi M_0}} + \mathbf{2}\right)^{\mathbf{2}} - \left(\frac{\mathbf{3}}{\mathbf{32}}\right)\left(\frac{\mathbf{P}}{\mathbf{2\pi M_0}} + \mathbf{2}\right) \qquad (2.\ 5)$$

Leinster et al. investigated the crushing of a spherical shell made of ductile material subjected to rigid wall impact analytically and experimentally. The ratio of mean radius to thickness was seven. Analytical approach was divided into two parts in terms of crushing mode of spherical shell as part I – pre-dimpling behavior mode and part II – dimpling behavior mode (Leinster et al. 1994).

Gupta and Venkatesh worked on the dynamic crushing behavior of thin walled aluminum spherical shells. The ratios of radius to mean thickness were between 13 and 85. It was presented that load-compression histories, energy absorbing capacity and mean collapse loads were investigated using finite element code. The spherical geometry was manufactured by spinning that caused the variation of thickness along meridian as can be seen in Figure 2.9. The thickness variation of spherical was considered to be linear in this study. It was reported that the spherical geometry having low ratios of R/t with smaller or equal to 1.5 mm thickness deformed with a formation of rolling plastic hinge. For the same thickness but higher R/t ratios, the formations of lobes were seen during the collapse. The rolling plastic hinge radius and mean load capacity increased as the strain rate increased (Gupta and Venkatesh 2004).

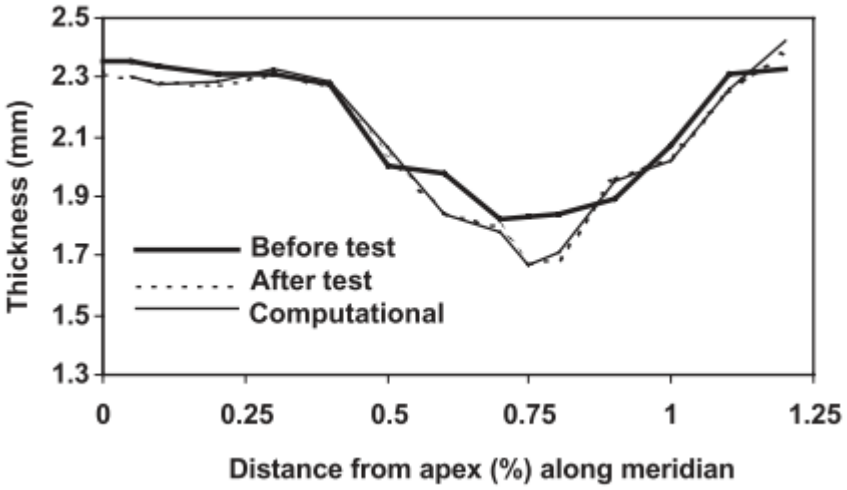

Figure 2.9. Typical variation of the shell thickness along meridian of deformed specimen (Source: Gupta and Venkatesh 2004)

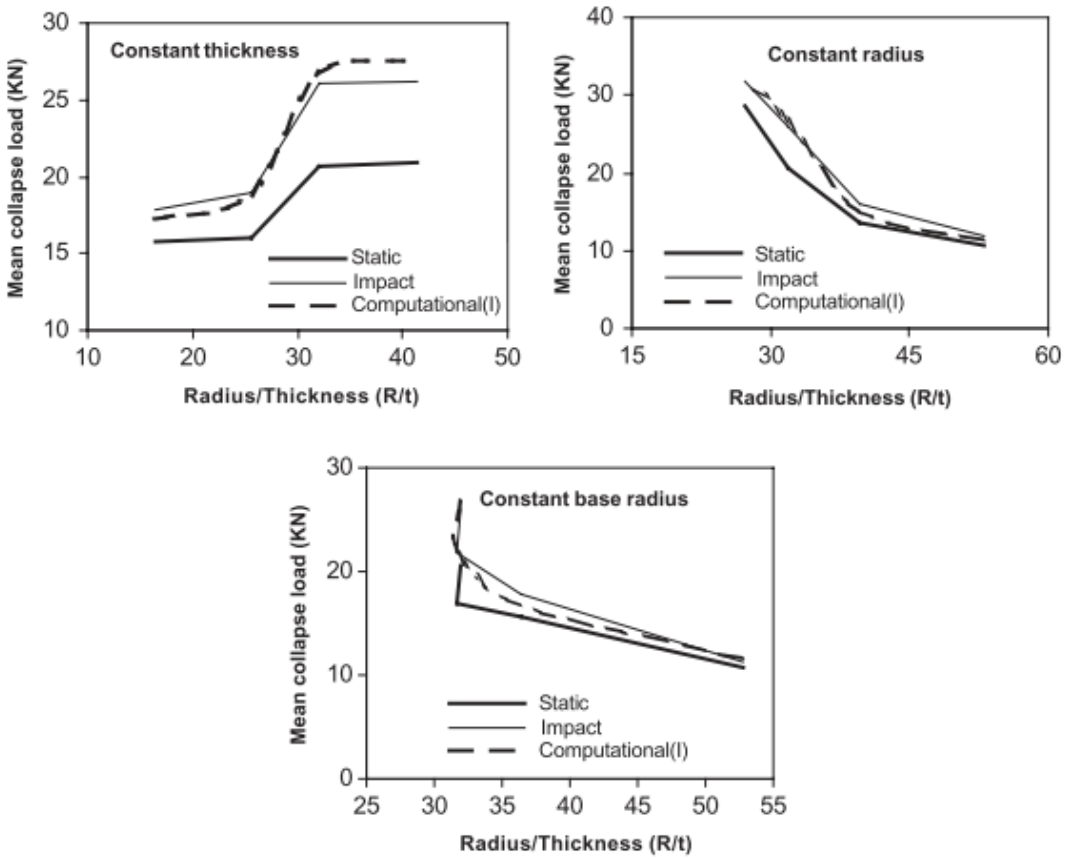

Figure 2.10. Variation of mean collapse load for shells of constant thickness, radius and depth (Source: Gupta and Venkatesh 2004).

It was reported that mean collapse load increased as radius increased with a constant thickness. When the ratio of radius to thickness ratios increased with a constant radius, mean collapse load decreased as can be seen in Figure 2.10. (Gupta and Venkatesh 2004).

Ruan et al. investigated the crushing behavior of thin walled spherical geometries using ping pong ball having uniform wall thickness and ideal material properties. The compression of spheres by point-load, rigid ball, rigid plate and rigid cap were conducted. When two ping pong balls crushed, the deformation happened contingently with deforming one of them and the other one saved their shape or deformed elastically. The deformation mode changed from type I to type II when the ping pong ball were connected by using a rigid cap. The crushing of balls occurred subsequently as crushing force increased until the other one started to deform. The crushing force was a function of diameter of the connection region (Ruan, Gao, and Yu 2006).

Gupta et al. investigated the dynamic behavior of the hemi and shallow thin walled aluminum spherical shells under impact loading. The crushing characteristics of spherical shells having different radius, height and thickness were determined. The ratios of radius to thickness were chosen between 20 and 219. The deformation modes were presented as local flattening, inward dimpling and formation of lobes at different velocities. Furthermore, as can be seen in Figure 2.11, the average crushing load increased as the thickness and radius increased. When the radius increased with a constant thickness value, the average load increased, Figure 2.12. The numbers of lobes formation were diversified depending on the R/t values and velocities, Figure 2.13. The thickness value was 1.6 mm or higher, the deformation occurred in axisymmetric mode. In Figure 2.14, the energy absorption was higher in dynamic crushing than that of static. It was reported that the mean collapse load and energy absorption capacity of hemi and shallow spherical shells were a function of thickness, radius and deformation rates (Gupta, Sheriff, and Velmurugan 2007).

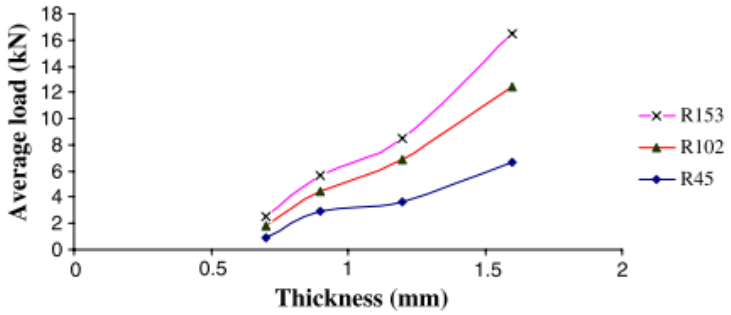

Figure 2.11. Variation of average load with thickness for various shell radius (Source: Gupta, Sheriff, and Velmurugan 2007).

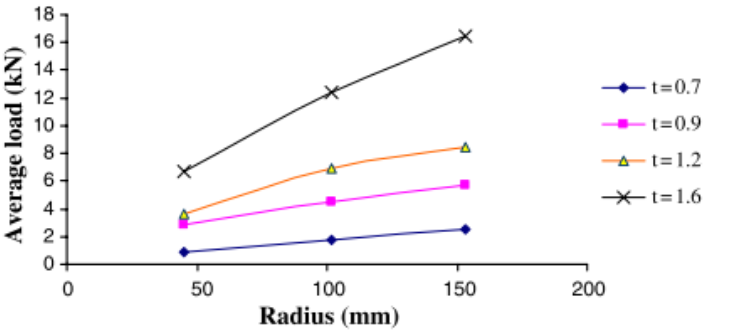

Figure 2.12. Variation of average load with radius for various shell (Source: Gupta, Sheriff, and Velmurugan 2007).

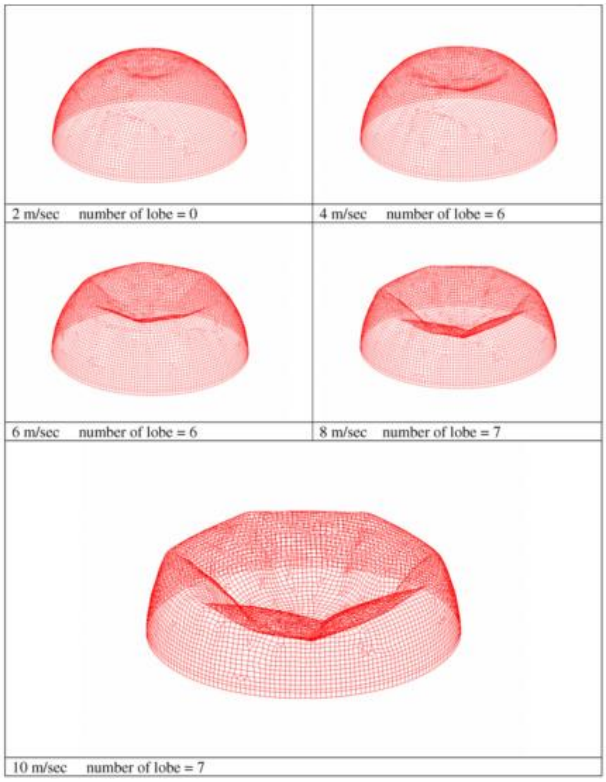

Figure 2.13. Progress of lobe formation with increase in velocity (Source: Gupta, Sheriff, and Velmurugan 2007).

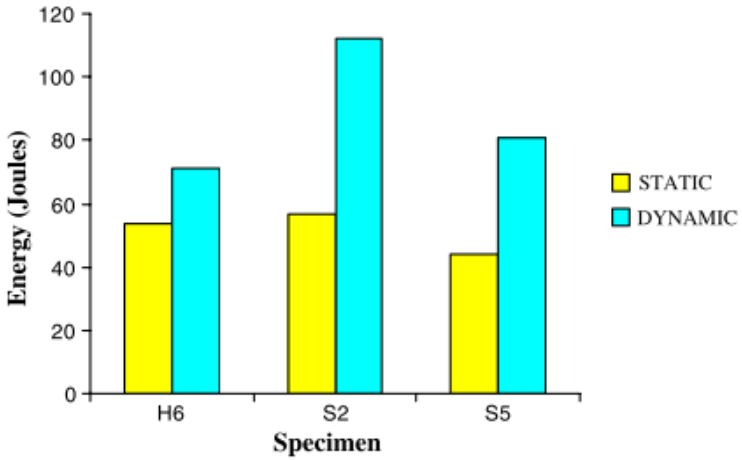

Figure 2.14. Comparison of energy absorbed values obtained in impact at 2 m/s and quasi-static tests (Source: Gupta, Sheriff, and Velmurugan 2007).

Dong et al. studied the crushing response of thin walled sphere at static and dynamic strain rates. Dynamic tests were conducted using a modified Split Hopkinson Pressure Bar (SHPB) test system. It was investigated that the deformation mode depended on the mainly impact velocities. The crushing force of sphere arrays is shown in Figure 2.15 for small deflection levels. The crushing force decreased after snap-through as the strain rate increased, Figure 2.16. The quasi-static crushing force of thin walled sphere

was higher than that of dynamic for large deflections, Figure 2.16. Additionally, the formation of lobe was affected by strain rates. Five lobe formation at quasi static compression and four lobe formations at dynamic compression can be good examples of this (Dong, Gao, and Yu 2008).

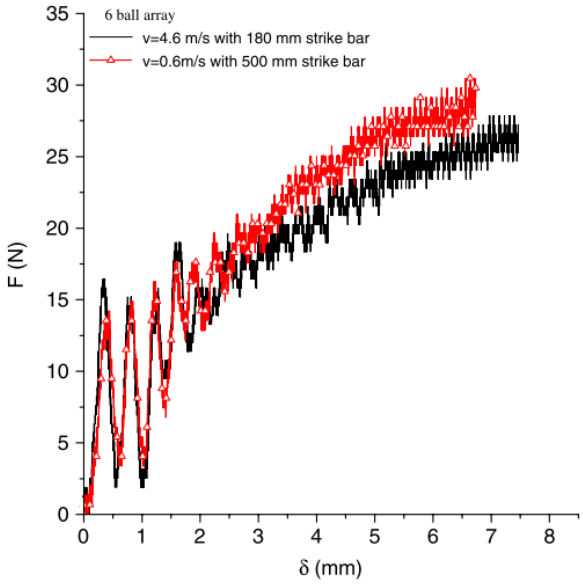

Figure 2.15. Force-deflection curves of 1-D arrays under different striker velocities (Source: Dong, Gao, and Yu 2008).

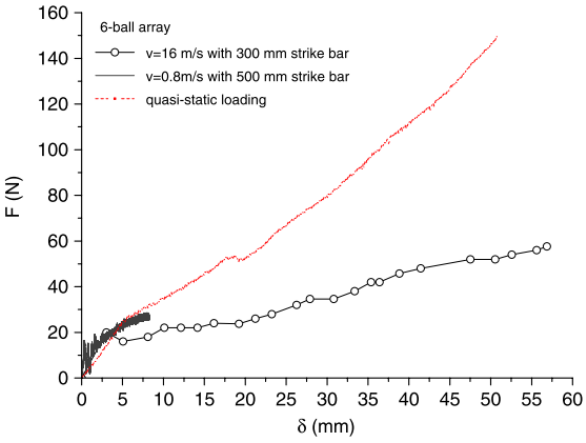

Figure 2.16. Force-deflection curves of 1-D arrays under quasi static and dynamic compression (Source: Dong, Gao, and Yu 2008).

Gupta et al. inspected the crushing behavior of thin wall spherical shells under static loading by experimentally, numerically and developed an analytical model using energy approach. The deformation mode was affected by height of compression, radius and thickness of the spherical geometry shells. The mode-jump issue was observed as a local flattening, inward dimpling and formation of non-symmetric number of lobes. It

was reported that the R/t ratios were smaller than 38.14 and the thickness was greater than 1.2 mm, the axisymmetric deformation was observed with the formation of plastic hinge. However, the number of non-symmetric lobes was generated when the R/t was higher than 50 and the thickness was smaller than 1.2 mm (Gupta, Sheriff, and Velmurugan 2008).

Gupta and Gupta studied the deformation behavior of metallic spherical shells of R/t ratios changing between 26 and 45 experimentally and numerically. The spherical shells were compressed by two rigid plates at quasi static strain rate. It was found that all spherical shells deformed in an axisymmetric mode. The increase in wall thickness resulted in higher energy absorption. The increase in R/t ratios caused decrease in energy absorbing capacity. The effects of height and interface condition were investigated in this study. It was reported that increase in height of sphere resulted increase in energy absorbing capacity. In addition, the friction coefficient between top plate and spherical shell did not have any effects on crushing response of spheres. However, the friction coefficient between bottom plate and spherical shell played a significant role in energy absorbing capacity due to boundary condition. As the friction coefficient of bottom plate ($\alpha 1$ and $\alpha 2$ were friction coefficients) increased, the energy absorbing capacity increased as seen in Figure 2.17. Additionally, the energy absorbing capacity was maximum when interface between bottom plate and spherical shells was fixed (Gupta and Gupta 2009).

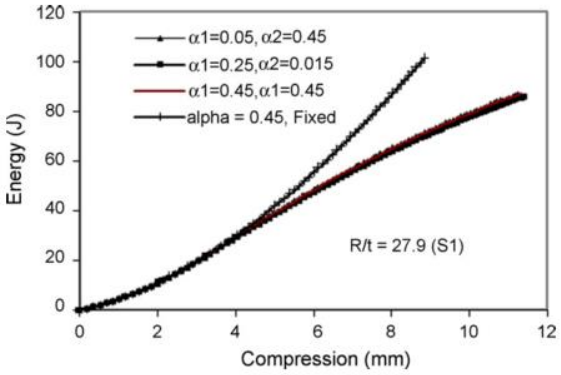

Figure 2.17. Computed energy-compression curves for specimen for 20 mm height for different shell-platen interface condition (Source: Gupta and Gupta 2009).

Dadrasi investigated the energy absorption capacity of aluminum and steel semi-spherical shells at dynamic strain rate using non-linear finite element techniques. The parameters of this study were diameters (100, 150 and 200 mm), thicknesses (0.8, 1.0, 1.2 mm), velocities (5, 7.5, 10 m/s) and impact masses (15, 20 and 25 kg). It was seen

that the diversity of load displacement curves between numerical and experimental results caused from internal defects of the material. In numerical study the material was assumed to be perfectly ideal. According to static and dynamic crushing responses of semi-spherical geometry shells, the absorbed energy increased with a constant rate 16% so dynamic crushing force was higher than that of static. For constant impact mass, the mean crushing force was only function of the thickness. The semi-spherical shells absorbed more energy when the diameter smaller for the same thickness. As wall thickness increased, the mean collapse load also increased but total deformation decreased. In addition to this when impact mass increased, mean collapse load also increased (Dadrasi 2011).

Bao and Yu worked on the dynamic response of hallow spheres subjected to collapse of rigid wall with different impact velocities experimentally and numerically. It was found that the number of lobes was function of an impact velocity. As can be seen in Figure 2.18, the number of lobes increased as impact velocity increased (Bao and Yu 2013).

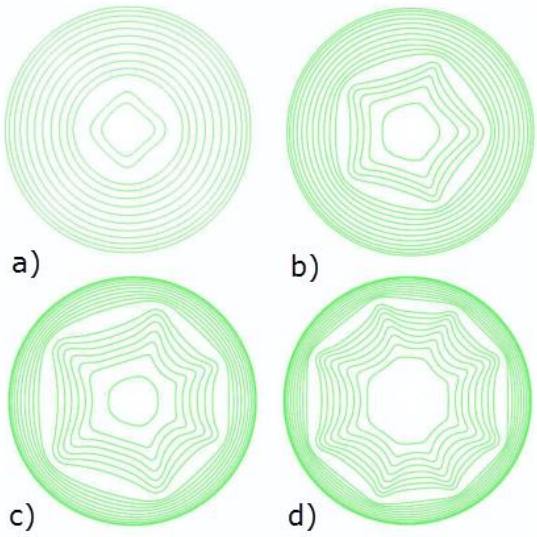

Figure 2.18. Non symmetric configuration, (a) 6 m/s (b) 15 m/s (c) 25 m/s (d) 30 m/s (Source: Bao and Yu 2013).

2.1.3. Crushing Behavior of Combined Geometry Shells

The structures consisting of two or more geometric portion were named combined geometry and this kind of structures represents the behavior of both geometric portions. That provides the combined geometries absorbing higher energies and lower transmitted

forces. Once the numerical and experimental approach improves, there are lots of valuable studies about crushing response of combined geometry shells.

Gupta et al. investigated the static and dynamic behavior of combined geometry shells which consists a conical frusta and a shallow spherical caps with various thicknesses 0.7, 0.9, 1.2 and 1.6 mm. For the spherical cap, the ratios of radius to thickness were between 27 and 218 and for the conical frusta; the ratios of mean diameter to thickness were between 79 and 190. When R/t ratios decreased, only the spherical portion deformed until the conical portion started to deform. As R/t ratios increased with the 1.2 mm or less thickness value, the specimen deformed with a deformation mode of inward dimpling and following the formation of lobes.

It was reported that deformation of combined geometry shells progressively occurred. At first deformation of spherical cap and further deformation of conical frusta were observed, Figure 2.19. Three different deformation modes were observed during crushing: formation of axisymmetric ring, inversion of cone and formation lobes. In addition, for conical portion when the ratio of mean diameter to thickness was less than 87.9 mm with 1.6 mm of thickness, the specimen deformed symmetrically. However, the ratio of mean diameter to thickness was greater than 94.89 mm with 1.2 mm or less of thickness, the collapse of structures was occurred completely non-symmetrically (Gupta, Mohamed Sheriff, and Velmurugan 2008).

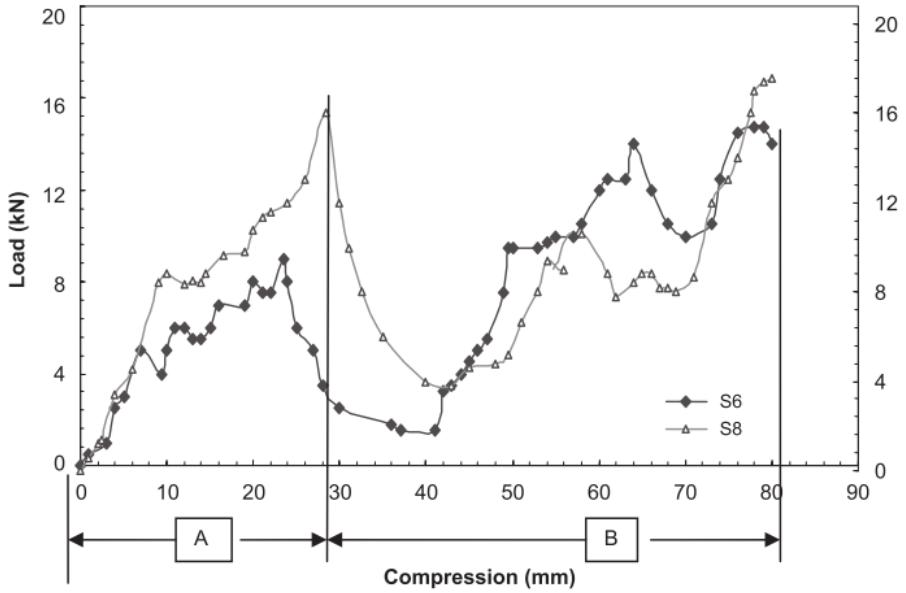

Figure 2.19. Load deformation curves under static compression for specimens S6 (1.6mm of thickness, semi apical angle= 21°, bottom diameter = 165 mm) and for specimen S8 (1.6 mm of thickness, semi apical angle = 25°, bottom diameter = 165 mm.) 'A' and 'B' show collapse zones of spherical and conical parts (Source: Gupta, Mohamed Sheriff, and Velmurugan 2008).

Gupta studied the compression of combined geometry metallic shells consisting tube and cone geometries at static strain rate. The ratio of top diameter to length for tube was 1/3 and the ratio of bottom diameter to length for cone was 2/3. The specimens were manufactured from between 1 and 5 mm aluminum sheet by spinning process and all of them were annealed at 3000 C° and cooled for 24 hours in a furnace. It was reported that the local buckling occurred at the junction of tube and cone and deformation continued with a plastic deformation of zone II and zone III as can be seen in Figure 2.20. The load-deformation and energy-deformation histories can be seen in Figure 2.21 (Gupta 2011).

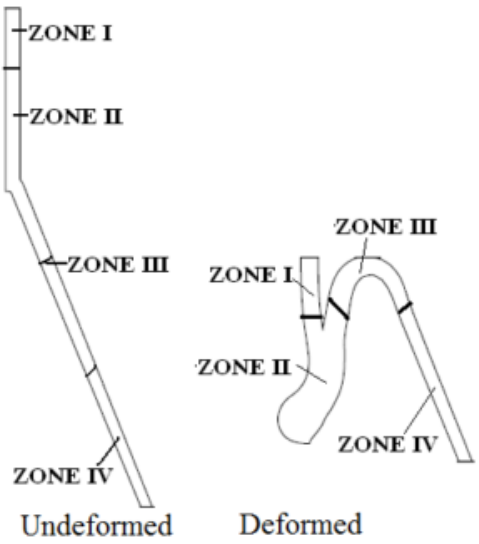

Figure 2.20. Demarcation of zones undeformed and a typically deformed shell (Source: Gupta 2011).

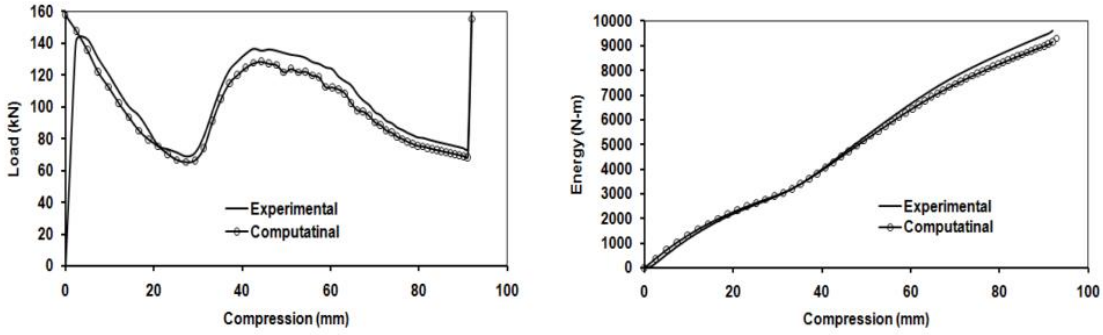

Figure 2.21. Comparison of typical load-deformation and energy-deformation curves experimentally and numerically (Source: Gupta 2011).

Gupta and Gupta developed the behavior axial crushing of combined geometry shells consisting tube and cone geometry shells with various thickness and semi apical angle of cone. After validating of numerical model of specimen of about 23° semi apical angle, specimens were modeled with 19° and 23° semi apical angle to investigate crushing responses. To understand the main mechanism of deformation, at the beginning of collapse the load-deformation history reached the initial peak value due to the uniform compression of tube and axisymmetric deformation occurred at junction of tube and cone geometry shells. After that the local buckling of the cone portion occurred during axial compression. That caused second peak value as can be seen in Figure 2.22. For different thickness values as 4, 3, 2.5 and 2 mm, the load-deformation histories are seen in Figure 2.22. It was reported that the load carrying capacity increased with higher thickness of shells. The buckling of combined geometry shell occurred at the junction of tube and cone

geometry for 2, 2.5 and 3 mm of thickness. However, the local buckling occurred at the middle of tube portion for higher wall thickness of specimens.

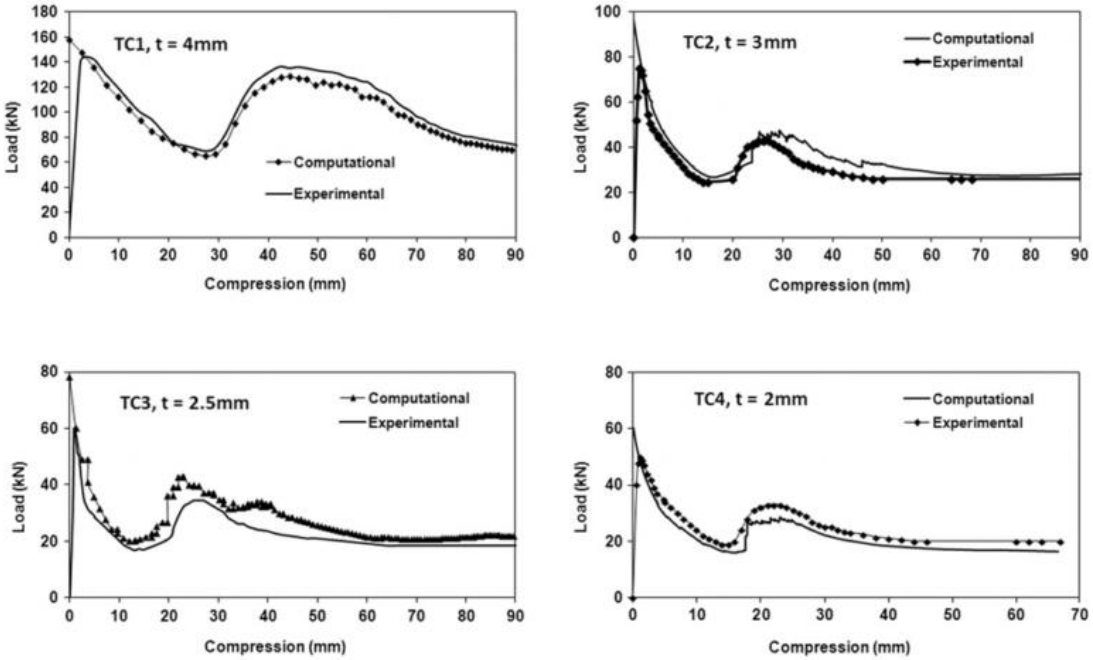

Figure 2.22. Comparison of load-deformation curves for all shells (Source: Gupta and Gupta 2013).

Numerical model was studied to observe the effect of semi apical angle on the crushing response. It was presented that when the semi apical angle was higher than 20°, the mode of collapse changed. When the semi apical angle decreased, deformation occurred with the formation of multiple concertina folds in tube portion, Figure 2.23 (Gupta and Gupta 2013).

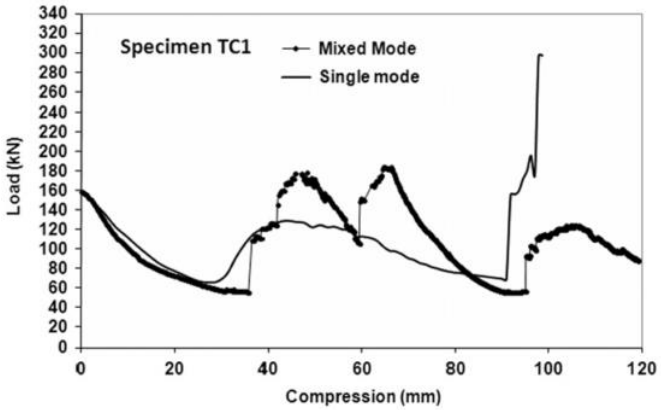

Figure 2.23. Variation of load-deformation curves for specimen collapsed in different modes (Source: Gupta and Gupta 2013).

Shojaeefard et al. investigated the energy absorption characteristics and the load carrying capacity of combined geometry shells consisting 90 x 90 mm of square and 57 mm radius of circular cross section tubes at quasi static strain rate. The initial peak value of circular cross sectional tube was found 26.4% more than that of square during collapse as can be seen in Figure 2.24; however the energy absorbing capacity of circular tube was higher (22.8%) than that of square tube, Figure 2.25. The combined geometry shells were created with a square and cylindrical cross sectional tube. It was concluded that, utilizing the combined geometry shells resulted in 4.6% and 31% lower initial peak load than only the square and circular cross sectional tube. The energy absorption of combined geometry was 18.1% higher than square and 4.7% lower than circular cross sectional tube (Shojaeefard et al. 2014).

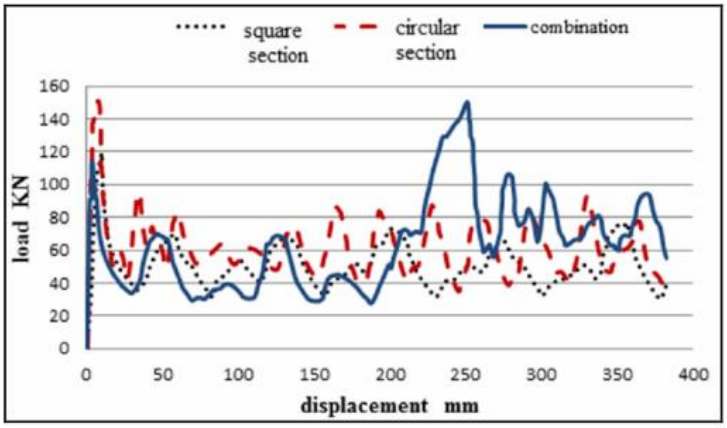

Figure 2.24. Comparison among the force-displacement diagrams of square, circular and combined geometry (Source: Shojaeefard et al. 2014).

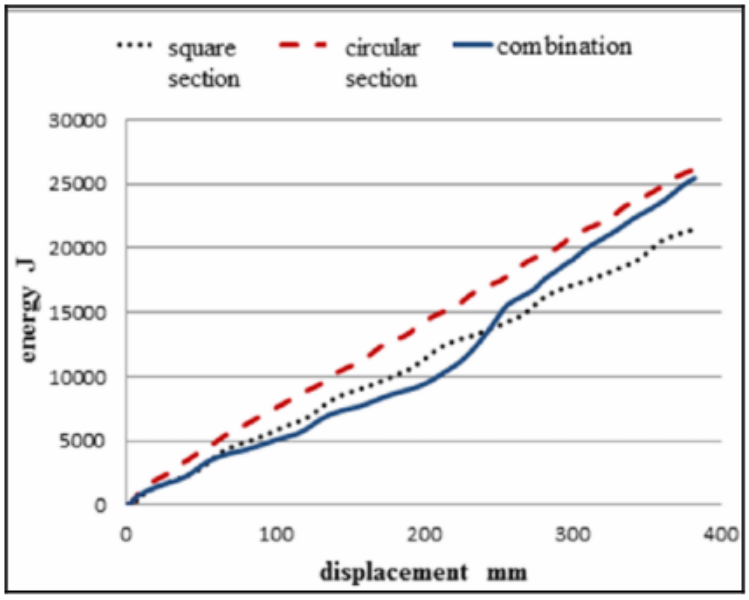

Figure 2.25. Comparison of energy-displacement diagrams of square, circular and combined geometry (Source: Shojaeefard et al. 2014).

2.2. Effect of Forming Process on Crashworthiness of Structures

Metal forming is a common way to fashion the components with a plastically deformation. Metal forming causes some significant variations those effects on the strength of material. Plastic deformation during manufacturing causes the variation of thickness and residual stress/strain. This phenomenon is enormously significant for crushing behavior of structures. The artificial effects of manufacturing method should be considered if the crushing behavior structure is proposed. The variations in the structure due to the manufacturing can be determined to use numerical method. There are lots of studies on the effects of manufacturing method on the crushing behavior of structures.

Sturt et al. worked on the effect of residual stress of stamping on the crushing response of vehicle. In this study the thickness and residual stress/strain were mapped into the crushing simulations. It was reported that stamping information did not affect on the deformation mode of components. However, the peak force of B-pillar decreased from 45.8 g to 42.1 g as can be seen in Figure 2.26 and the force-time histories of side member increased from 50 kN to 59 kN with including stamping information as can be seen in Figure 2.27. Including stamping information into crushing of a vehicle was significant to correlate the experimental and numerical responses (Sturt et al. 2001).

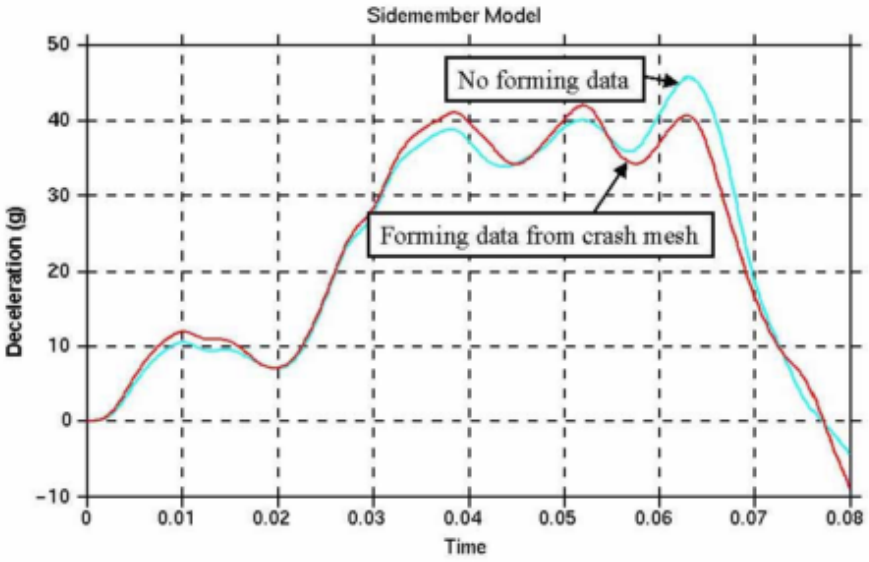

Figure 2.26. B-Pillar deceleration histories
(Source: Sturt et al. 2001).

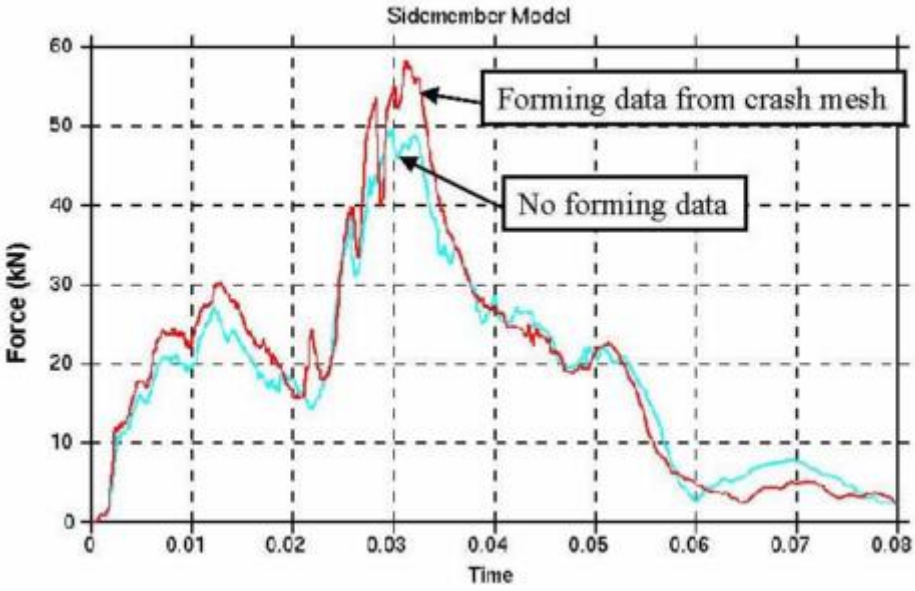

Figure 2.27. Force-time histories of side member of vehicle
(Source: Sturt et al. 2001).

Böttcher and Frik studied the effect of residual stress and strain and thickness variation of structures made by sheet metal on the impact performance of a car. In this study front crushing of vehicle was studied. It was reported that there were significant differences for crushing response of front rail between tests and numerical model. In order to include the manufacturing effect to the crushing behavior of front rail, the stamping model was modeled. With stamping effect, the numerical result correlated well with experimental result (Bottcher and Frik 2003).

Cafolla et al. proposed that influence of metal forming into crushing response of structures. Thanks to improvement in numerical approach in crushing phenomenon, obtained results being good agreement with experiments can be conducted in three ways as following. First step was to determine the parts being relevant to absorb more energy. Second step was to conduct manufacturing process numerically and last step was to account stamping information into crushing simulations. It was reported that forming influenced the material strength and final geometric shape due to the hardening and thickness thinning, respectively (Cafolla et al. 2003).

Krusper investigated the crushing behavior of a square sectional tube with stamping information. Thinning and residual stress/strain were considered separately into the crushing responses of structures. The deformation mode of specimen with residual stress/strain and thickness distribution was observed with global buckling. When the specimen had only residual stress, the specimen deformed with local buckling. (Krusper 2003).

Hoek studied the effects of stamping information on the crushing response of a truck bumper. The crushing of bumper of truck with stamping information, only residual strain, only residual stress, only thinning and without all stamping information. It was reported that the thinning of structure during forming operation resulted in the lower response of the structure. In addition, the structure was stiffer with plastic strain. The effect of residual stress was found to be insignificant. However, plastic strain was most important to converge the crushing response, Figure 2.28 (Hoek 2006).

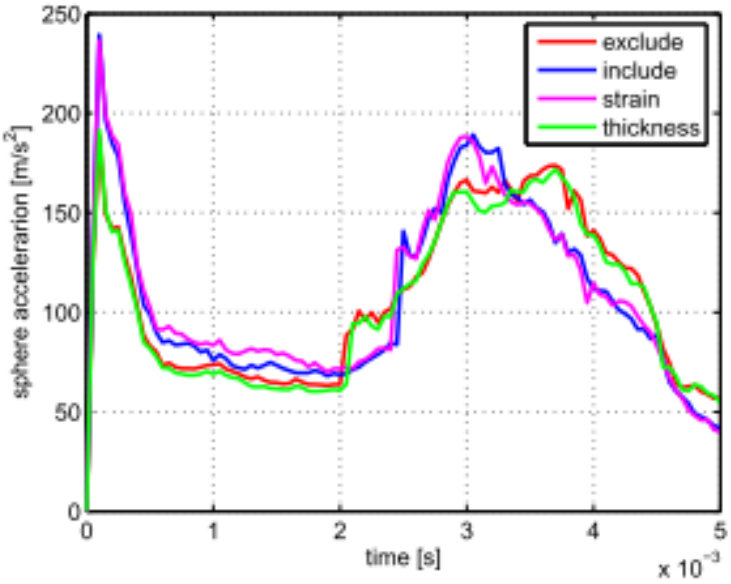

Figure 2.28. Acceleration of Sphere impacted to structure
(Source: Hoek 2006).

Doğan studied the dynamic crushing behavior of a vehicle impacted to rigid wall numerically. The higher energy absorbed parts were found and produced numerically with the variation of thickness and residual stress/strain. To investigate the effects of manufacturing method, all forming information were included into crushing simulations. In Figure 2.29, the numerical result with forming histories converged to the test. It was reported that forming information was significant to obtain realistic crushing simulations (Doğan 2009).

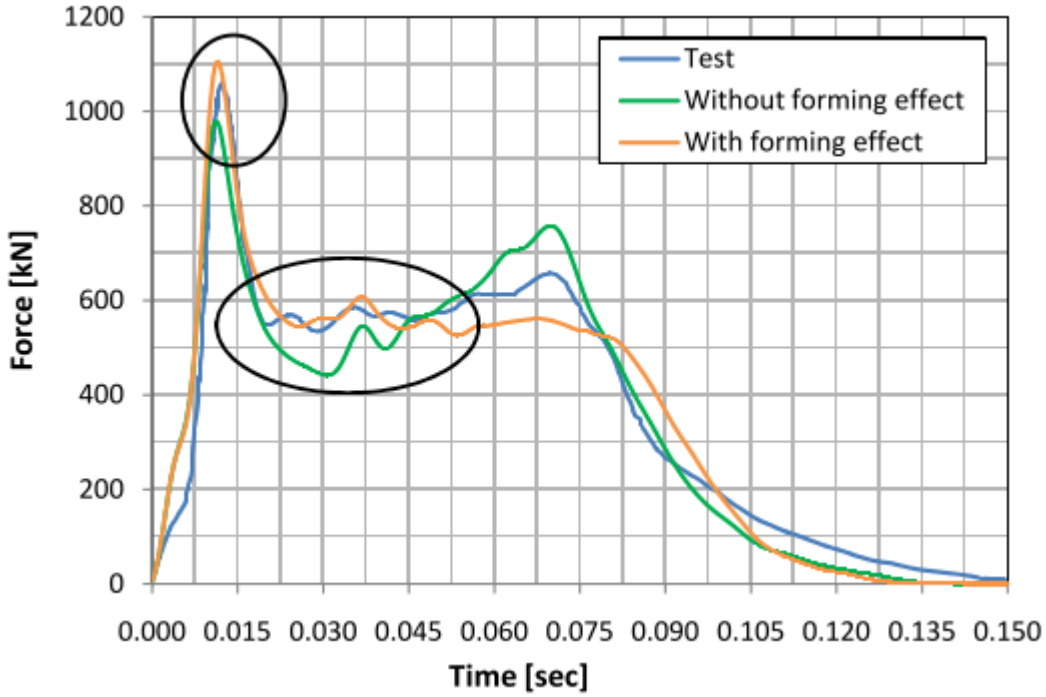

Figure 2.29. Comparison of the total force experimentally and numerically (Source: Doğan 2009).

Alysson L. Vieira and Mesquita presented the influence of metal forming histories on the crushing response of an automobile fender at quasi static strain rate. When strain hardening and thickness distribution were included into the crushing simulation, the numerical results correlated well with the experimental results. (Alysson L. Vieira and Mesquita 2010).

CHAPTER 3

MANUFACTURING AND TESTING METHODS

3.1. Design and Manufacturing of Combined Geometry Shells

The combined geometry shell consists of hemi-spherical and cylindrical segments. AISI 304L stainless steel was selected due to the higher strain rate sensitivity. The chemical composition of AISI 304L stainless steel is shown in Table 3.1.

Table 3.1. Chemical composition of AISI 304L stainless Steel

C (% weight)	Cr (% weight)	Ni (% weight)	Mn (% weight)
0.03	17.5-19.5	8.0-10.0	2.0

The aim of this study is to investigate the crushing behavior by performing tests at static and dynamic strain rates and gaining more insight in to the deformation process by numerical simulations. As mentioned in Chapter 2, progressive buckling is significant in energy absorption of thin walled structures.

3.1.1. Deep Drawing

Deep drawing is one of the most common manufacturing methods for forming a metal sheet to deep-shape cylindrical or box geometries like fuel tanks, saucepans or containers in the industry. The tooling has fundamental parts; blank, die, punch and blank holder as can be seen in Figure 3.1 and it is explained basically that a metal sheet as a blank material is placed over the die and blank holder is pressed on the metal sheet in order to avoid any wrinkling of flange. After that punch begins to travel through the formation direction with a desired force until it reaches proposed depth.

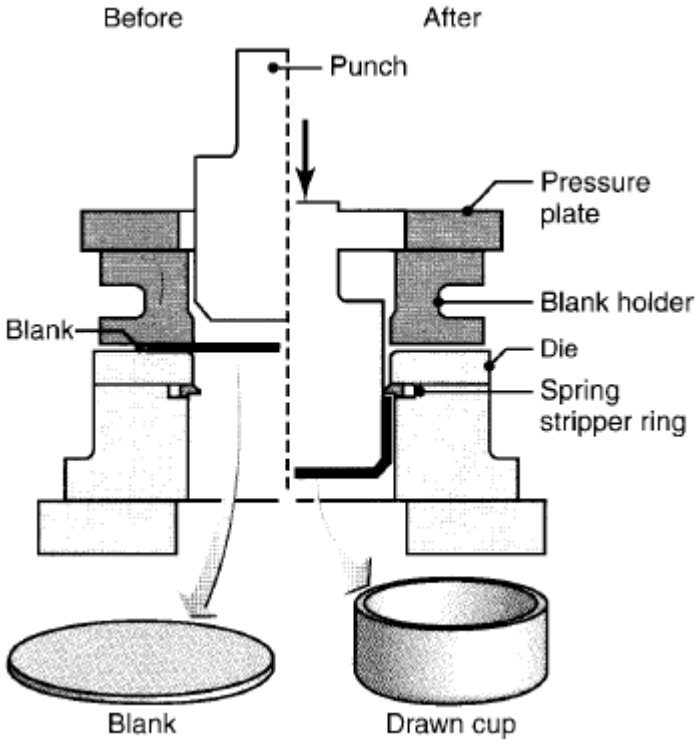

Figure 3.1. The schematic of deep drawing process
(Source: Serope Kalpakjian 2009)

It is possible to produce complex geometries with low cost using the same pattern. At the end of the production, seamless parts can be obtained easily. On the other hand, plastic deformation causes a change in the mechanical properties of the structure. Strain hardening and residual stress result in higher strength levels.

In deep drawing, there are significant parameters such as; the properties of blank material, clearance between punch and die, the diameter of die and punch in particular punch force, friction and lubrication in order to prevent from any defects during deep drawing process.

These defects are developed during deep drawing process or after drawing operation. The well-known failure types in this process were given in following.

- The irregular defects can be seen on the wall of cup in the case of higher punch forces applied, and this issue can be occurred days after process. In order to prevent this situation, the specimens can be annealed after the operation.
- Material properties are also significant for deep drawing. Using the material having the planar anisotropy can be resulted in to wrinkling on the wall of the blank. In order to avoid this phenomenon, the annealing can be done.

- In deep drawing, tearing can occur when higher punch forces are applied. Similarly blank holder force could result in common defects during the process. Tearing is frequently seen on the flange of the blank. If the blank holder force is applied less than required, wrinkling can also be seen, oppositely. Therefore, the blank holder force and punch force must be determined as a function of the punch travel and the maximum force value.
- In the same manner the corner radius of the die is also crucial to prevent common defects like fracture or wrinkling during the process. If the corner radius is too small, fracture can be occurred on the wall cup.

The combined geometry shells were manufactured in two different radii, namely 12.5 mm and 7.5 mm from 0.5 and 1 mm thick AISI 304L stainless steel. The deep drawing model and the combined geometry shells are shown in Figure 3.2. The technical drawings of specimens are shown in Figure 3.3.

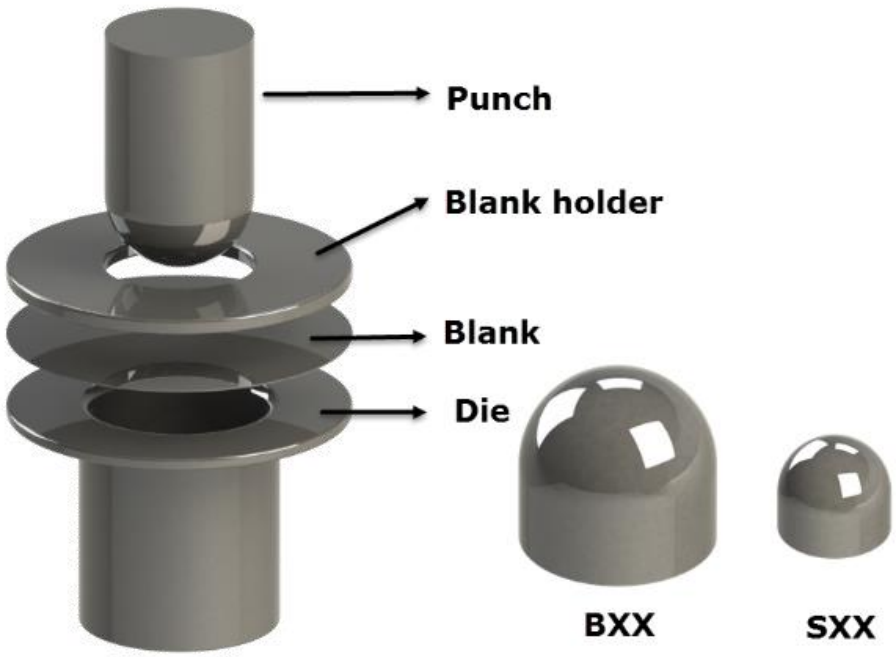

Figure 3.2. Deep drawing model and the combined geometry shells.

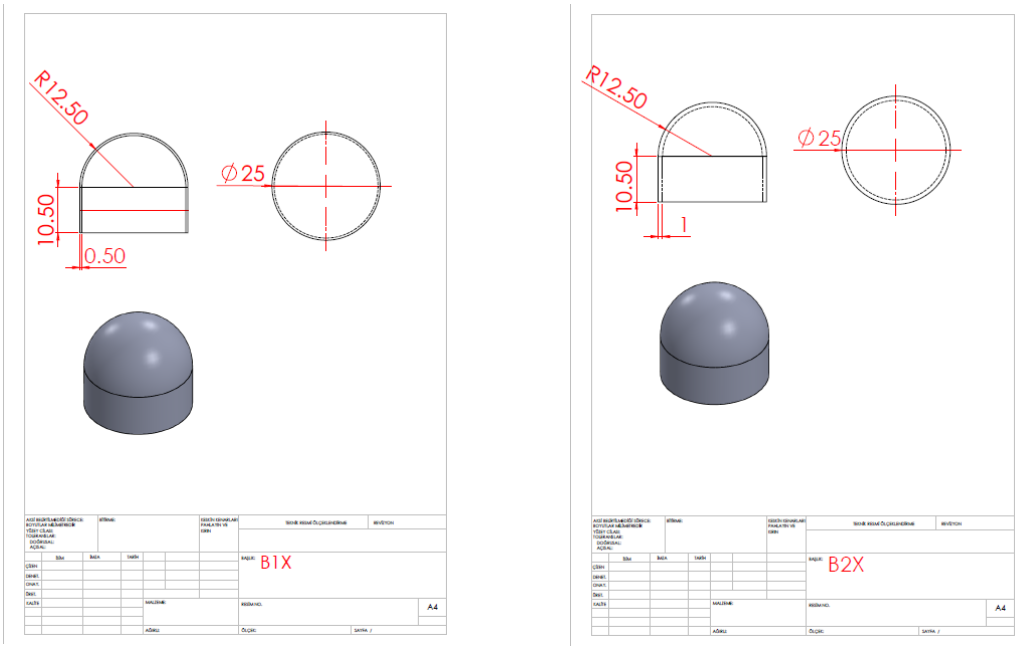

(a) (b)

(c) (d)

Figure 3.3. Technical drawings of (a) B1X, (b) B2X, (c) S1X and (d) S2X.

In the current study, the geometries were created in two stages in deep drawing as seen in Figure 3.4. At the first stage, hemi-spherical portion of the specimens was formed and a cylindrical portion was created with the movement of the punch into another die. After the production of combined geometry shells in deep drawing, the ears of cylindrical segments were trimmed with the cutting tool on a CNC lathe. At the end, four different configurations were obtained. The combined geometries were coded as in terms of radius

and thickness values. The coding of configurations is following: S1X, S2X, B1X and B2X. ‘S’ and ‘B’ refer to specimens’ radius as 7.5 mm (S) and 12.5 mm (B). The second code is related with thickness values of specimens. ‘1’ and ‘2’ represent 0.5 mm and 1.0 mm thickness of specimen, respectively. The last letter as ‘1’ and ‘2’ refers to test at quasi static and dynamic strain rates, respectively. For instance; (‘B11’ refers to the specimen having 12.5 mm radius and 0.5 mm thickness at quasi static compression test.)

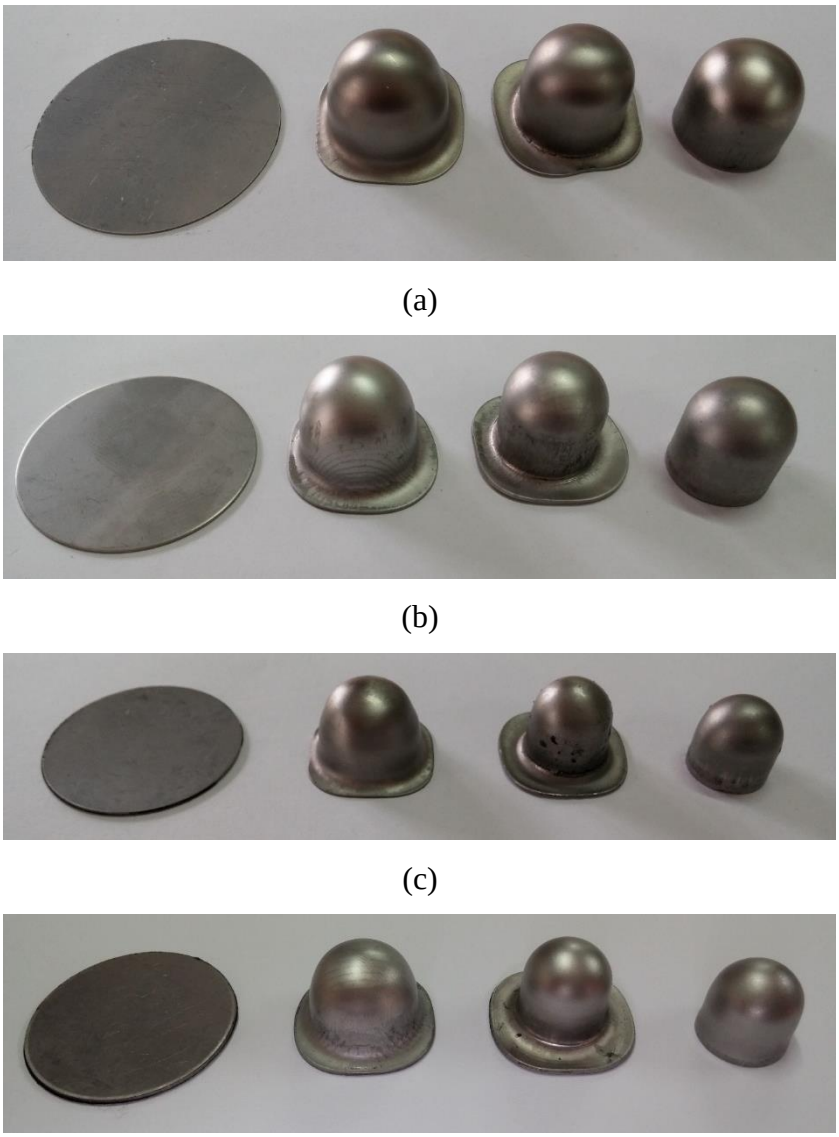

(a) (b) (c) (d)

Figure 3.4. Illustration of the deep drawn (a) B1X, (b) B2X, (c) S1X, (d) S2X specimens after each stage.

During the formation of combined geometries in deep drawing, there were nonlinear thickness variations on the specimens’ wall due to the plastic deformation. As seen in Figure 3.5, red lines refer to the initial thickness of all configurations. For

thickness variation of B1X, the sheet metal thinned about 30% in the hemi-spherical segment. On the other hand, sheet metal thickened about 36% in the cylindrical segment. For thickness variation of B2X, there was a thinning in the hemi-spherical segment about 23% and the thickness value of cylindrical segment was around 1 mm. For the thickness variation of S1X, the sheet metal thinned about 30% in the hemi-spherical segment and thickened about 26% in the cylindrical segment. For thickness variation of S2X, sheet metal thinned about 25% in the hemi-spherical segment and about 7% in the cylindrical segment. For all of the configurations, the thickness of hemi-spherical segment decreased in a nonlinear move between 30% and 25%. 0.5 mm thick sheet metal thickened in the cylindrical segment for specimens B1X and S1X. However, there was not significant thickness variation for the specimens of B2X and S2X in the cylindrical segment.

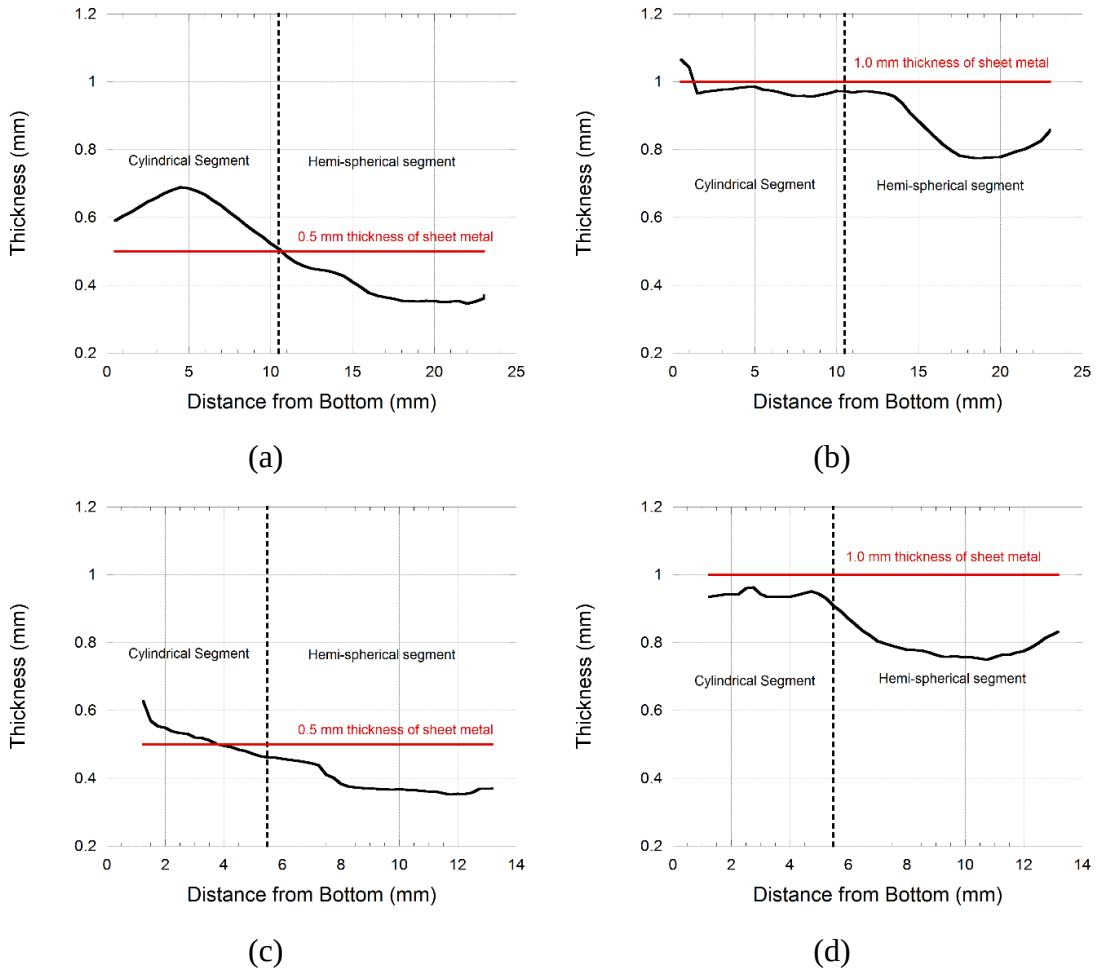

Figure 3.5. Thickness distribution of (a) B1X, (b) B2X, (c) S1X and (d) S2X specimens.

3.2. Testing Methods of the Combined Geometry Shells

In order to investigate the crushing response of combined geometries, crushing tests of all configurations were conducted at both quasi static and dynamic strain rates. The mechanical characterization of AISI 304L stainless steel was also carried out to obtain the material model constants which will be used in numerical simulations. The testing methodology is explained below.

3.2.1. Mechanical Characterization of AISI 304L Stainless Steel

The mechanical characterization of AISI 304L stainless steel was needed to determine the mechanical properties of material. In order to determine the elastic and plastic deformation behavior of the material, quasi static and dynamic tension tests were performed using a Shimadzu universal testing machine in accord with ASTM E8M-04 at quasi static strain rates (10^{-3} s^{-1}, 10^{-2} s^{-1}, 10^{-1} s^{-1}) and using Split Hopkinson Pressure Bar (SHPB) at dynamic strain rates (900 s^{-1} and 1400 s^{-1}). Shimadzu universal testing machine and quasi static test specimen are shown in Figure 3.6. SHPB experiment setup and dynamic test specimens are shown in Figure 3.8.

(a) (b)

Figure 3.6. (a) The universal testing machine Shimadzu and (b) the quasi-static test specimens.

For quasi-static tension test, the displacement of the cross head was recorded using a video extensometer and force was also recorded in. The stress-strain curves at quasi static strain rates are given in Figure 3.7 of three different strain rates (10^{-3} s^{-1}, 10^{-2} s^{-1}, 10^{-1} s^{-1}).

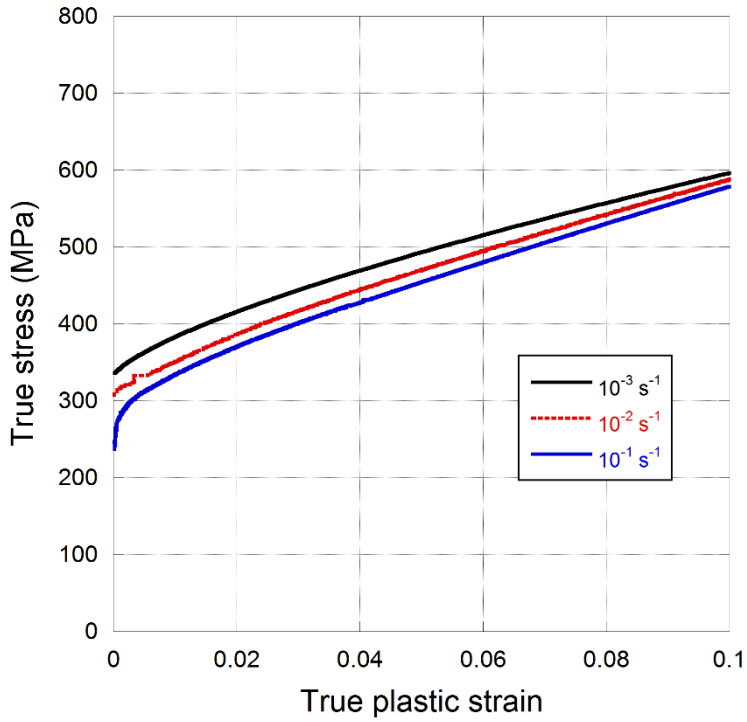

Figure 3.7. True stress-strain curves of AISI 304L stainless steel at quasi static strain rates.

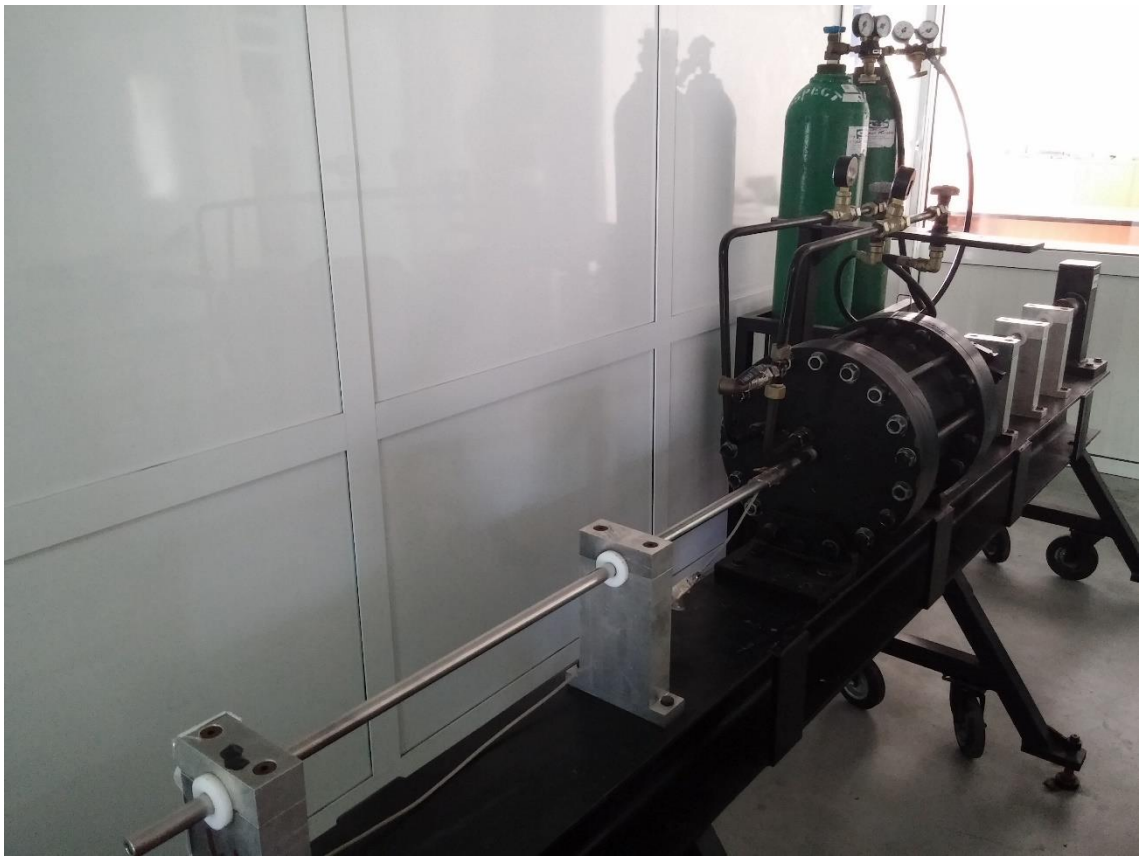

(a)

(b)

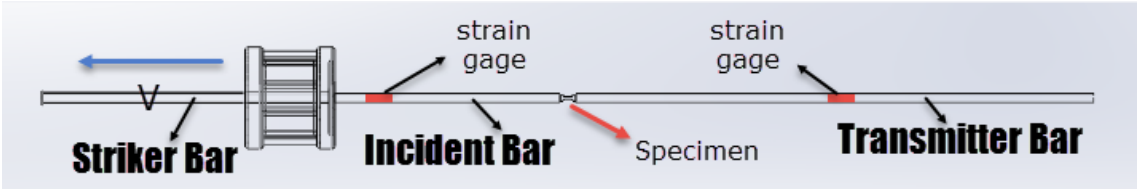

(c)

Figure 3.8. (a) SHPB experiment setup, (b) SHPB tension test specimens, and (c) schematic of the SHPB.

For the dynamic tension test, tension SHPB was used. The main constituents of tension SHPB setup are striker tube, incident and transmitted bars. The specimen is sandwiched between incident and striker bars. The striker tube impacts to the incident bar and a tensile elastic wave propagates in the incident bar. The elastic wave travels through the incident bar and gets into the specimen and transmitted bar. The strain values are measured via strain gauges on the incident and transmitted bars in terms of voltage using oscilloscope during the experiment. The incident and reflected waves are measured from the strain gage located on the incident bar, while transmitted pulse is measured from the strain gage on the transmitted bar. In Figure 3.9, a typical SHPB tension test result is shown. At the same time, the deformation of the specimen is recorded using Photron Fastcam high speed camera. The strain can be calculated using Eqn. 3.1, where V_{exc} is excitation number, GF is gage factor and K_{gain} is the gain. Strain can be found with Eqn. 3.2 where Cb, elastic wave speed of the bar and L_s, length of the specimen in. Furthermore, stress can be found with Eqn. 3. 3 where E_b is the elastic modulus of bar, A_b is the cross section area of bar, A_s is the cross section area of specimen and ε_t is strain measured on the transmitter bar. The true plastic stress-strain curves of AISI 304L stainless steel is shown in Figure 3.10 at dynamic strain rates.

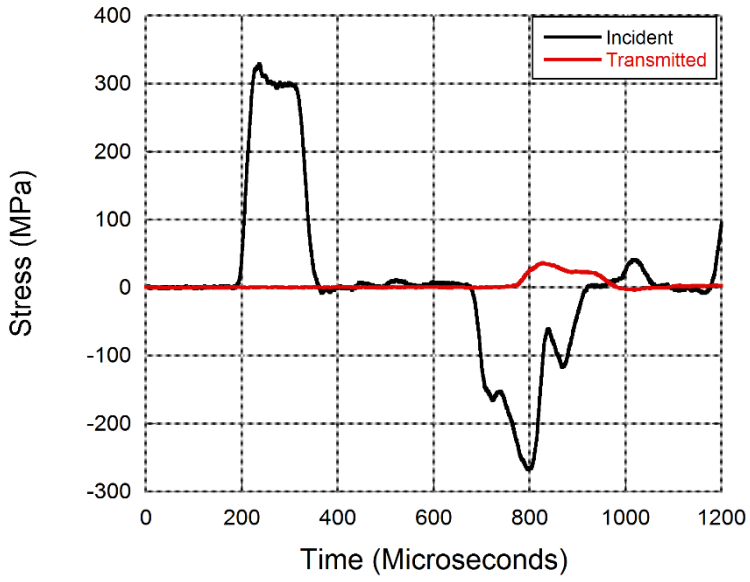

Figure 3.9. A typical SHPB tension test result.

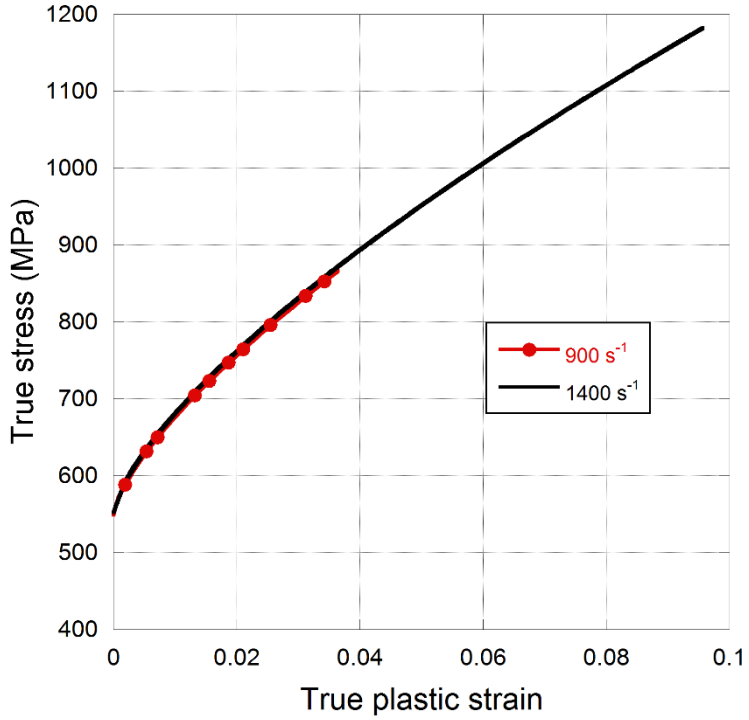

Figure 3.10. True plastic stress-strain curves of AISI 304L stainless steel at dynamic strain rates.

$$\varepsilon(t) = \frac{4 \times Voltaj(t)}{V_{exc} \times GF \times K_{gain}} \quad (3.\ 1)$$

$$\varepsilon_s(t) = -2\frac{C_b}{L_s}\int_0^t \varepsilon_r dt \quad (3.\ 2)$$

$$\sigma_s(t) = E_b \frac{A_b}{A_s}\varepsilon_t \quad (3.\ 3)$$

3.2.2. Material Model of AISI 304L Stainless Steel

Johnson Cook (J-C) material model was chosen to include the plastic deformation behavior, strain rates sensitivity and thermal effects. Equivalent stress is given in Eqn. 3.4, where *A*, *B*, *n* and *C* are material constants, ε_{eq} is the effective plastic strain, $\dot{\epsilon}_{eq}$ is the effective strain, $\dot{\epsilon}_0$ is the reference strain rates, and *T* is the absolute temperature, T_r is the room temperature, T_m is the melting temperature and M is temperature constant. In this study, M values was taken as 1.0 from the literature (Lee et al. 2006). Material model parameters of AISI 304L stainless steel are given in Table 3.2.

$$\sigma = \left(A + B\varepsilon_{eq}^{n}\right)\left(1 + Cln\left(\frac{\dot{\epsilon}_{eq}}{\dot{\epsilon}_0}\right)\right)\left(1 - \left(\frac{T-T_r}{T_m-T_r}\right)^{M}\right) \quad (3.\ 4)$$

Table 3.2. Johnson–Cook model properties of AISI 304L stainless steel used in numerical models (Source: Tasdemirci et al. 2015).

ρ (kg/m^3)	G (Gpa)	E (GPa)	ν	A (MPa)	B (MPa)	n	C	D1	D4
7830	80	193	0.305	264	1567.33	0.703	0.067	0.53467	-0.01913
Tr (K)	Tm (K)								
296	1698								

Failure can also be modeled with Johnson Cook damage model. Failure strain is defined in Eqn. 3.5, where D_1, D_2, D_3, D_4 and D_5 are damage parameters, $\sigma^*=\sigma_m/\sigma_e$ stress was stress triaxiality ratio of mean stress to effective stress. In this study, the stress state did not change significantly during loading. Thus, the parameters related with stress triaxiality were assumed zero. The Eqn. 3.5 was simplified into Eqn. 3.6 and the damage parameters D_1 and D_4 are given in Table 3.2.

$$\varepsilon_f = \left[D_1 + D_2 e^{D_3\sigma^*}\right]\left[1 + D_4\, ln\left(\frac{\dot{\varepsilon}}{\dot{\varepsilon_0}}\right)\right]\left[1 + D_5\, \frac{T-T_r}{T_m-T_r}\right] \quad (3.\ 5)$$

$$\varepsilon_f = D_1\left[1 + D_4\, ln\left(\frac{\dot{\varepsilon}}{\dot{\varepsilon_0}}\right)\right] \quad (3.\ 6)$$

3.2.3. Quasi-static and Dynamic Tests of the Combined Geometry Shells

The compression tests of combined geometry shells were conducted at quasi static and dynamic strain rates to investigate the crushing behavior. The compression tests at quasi static strain rates were performed using a universal testing machine Shimadzu. The specimen was located between two rigid plates and loaded along one axis with a constant crosshead speed. The quasi-static experimental setup is shown in Figure 3.11. The crosshead speed was selected as between $0.023\ mm/s$ and $0.013\ mm/s$ according to the length of the specimen for bigger and smaller specimens to keep strain rate constant (10^{-3} s^{-1}), respectively. On the other hand, the stroke of crosshead was measured via

extensometer to determine the strain of the specimen. Additionally, deformation history of specimens was recorded using camera.

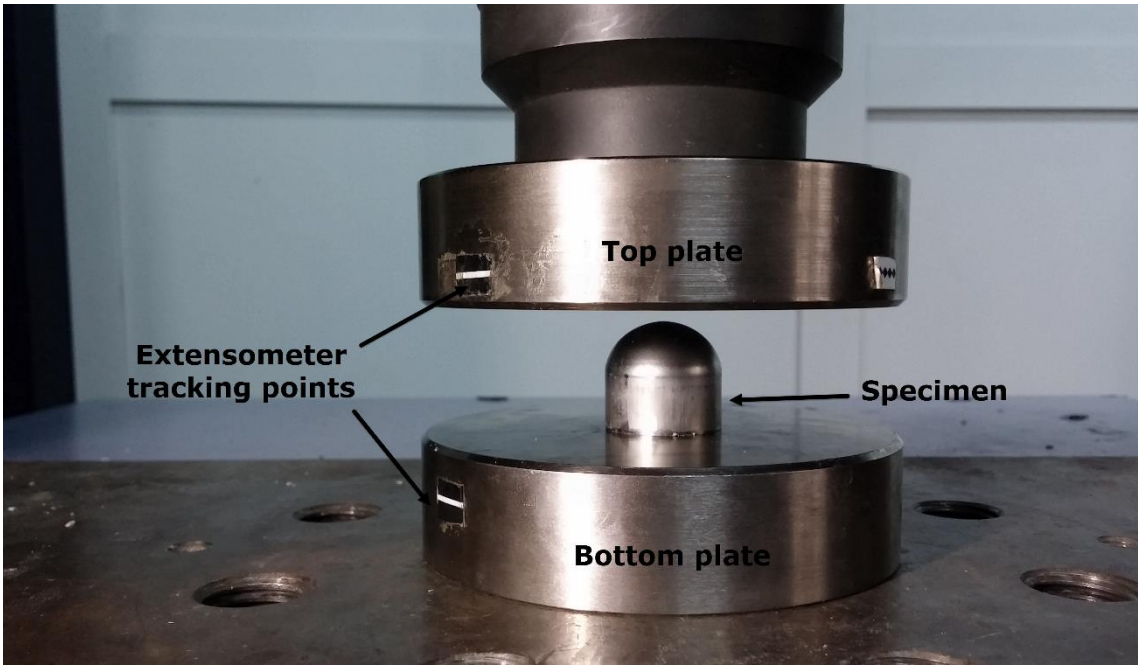

Figure 3.11. Quasi-static experimental setup.

Furthermore, compression tests at dynamic strain rates were performed using Fractovis drop weight tower as seen in Figure 3.12. Fractovis drop weight tower is 90 kN maximum loading capacity, 25 m/s impact velocity and 75 kg additional mass. The system consists of a stationary bottom plate, striker, striker tip, and striker weight and velocity sensor. The flat end striker impacts to the specimen with additional masses at a desired velocity. The force is recorded via DAS data acquisition system. Additionally, Photron Fastcam high speed camera was used to record the deformation history of the specimen.

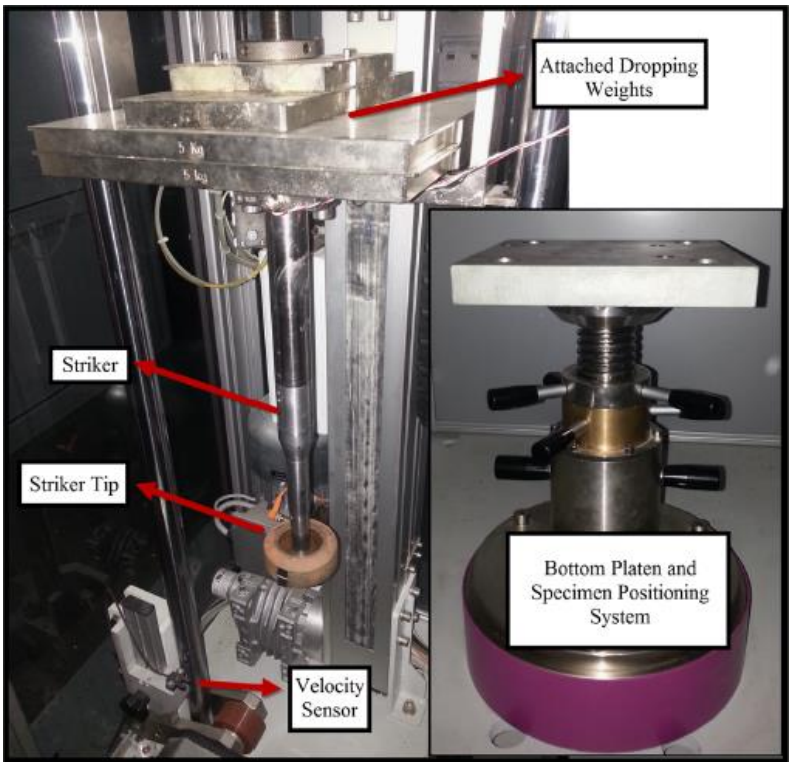

Figure 3.12. Drop weight test setup.

Test parameters are given in Table 3.3. For bigger specimens BXX, the striker velocity was 9.1 m/s and for smaller specimens SXX, the striker velocity was 5.1 m/s in order to obtain similar strain rate levels (400 s^{-1}).

Table 3.3. Impact velocities and drop masses in drop weight tests.

Specimens	Impact velocity (m/s)	Impacted mass (kg)
B1X	9.1	7.4
B2X	9.1	14.4
S1X	5.1	10.4
S2X	5.1	23.4

CHAPTER 4

NUMERICAL STUDIES

4.1. Numerical Studies of the Manufacturing Method

Numerical analysis is an addition tool to gain better insight into a complex problem. In current study in order to investigate the crushing response of the proposed geometry, a detailed finite element analysis was done. Finite element analysis is a method to solve partial differential equations by discretizing the domain into finite elements and considering boundary conditions with numerical approximation for engineering applications. For this purpose commercially available explicit finite element code LS DYNA 971 was used for numerical modeling.

Before the investigation of the crushing behavior of the combined geometry shells, three different specimens were created numerically in order to define the best numerical modeling route. The first specimen was modeled with shell elements having a constant thickness of 0.5 mm. For the second and third specimens, deep drawing was modeled numerically, and the second specimen includes only non-linear thickness distribution. The third specimen includes all both non-linear thickness distribution and residual stress/strain. As seen in Figure 4.1, the force-displacement history of specimen having only thickness distribution was lower than that of constant thickness distribution specimen because when the residual stress/strain and thickness distribution was considered, the crushing response increased when compared with other cases and correlated well with the experimental result. It was shown that the numerical manufacturing route to implemented specimen was significant and significantly affects on the crushing response. The actual thickness distribution was not itself enough. Additionally, residual stress/strain must be implemented with the non-linear thickness distribution.

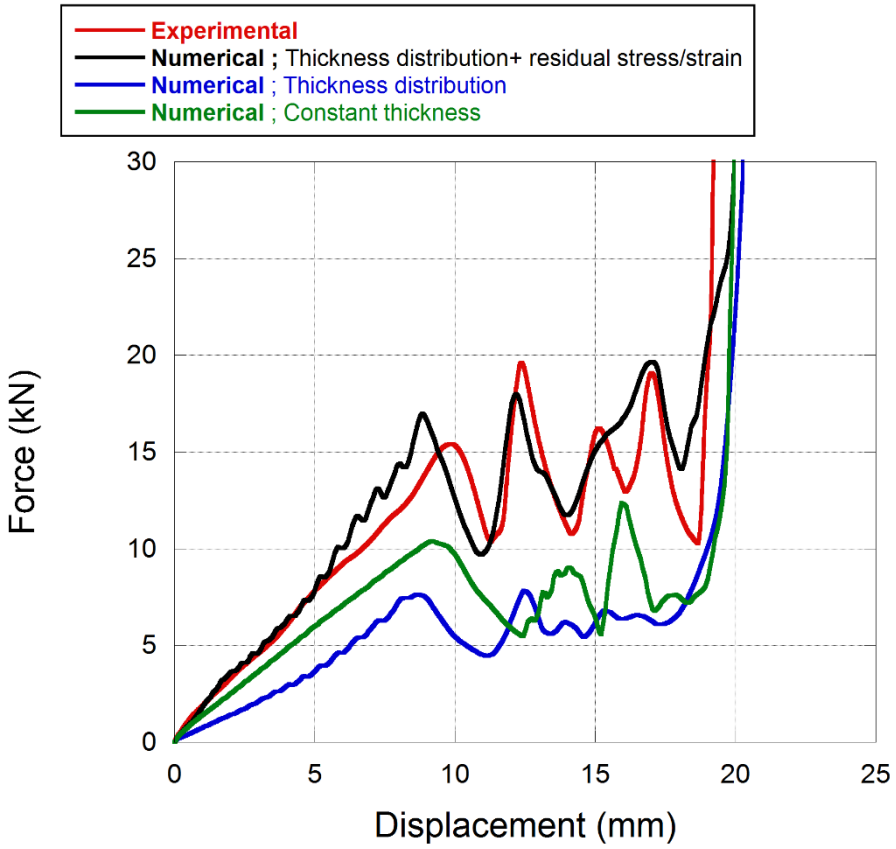

Figure 4.1. Manufacturing effects on crushing behavior of combined geometry shell.

Thus, in the numerical study, the deep drawing was modeled numerically. The deep drawing numerical model consists of blank, blank holder, die and punch as seen in Figure 4.2. All parts were modeled using Belytschko-Tsay element formulation in which the bending stiffness is negligible, with seven integration point through the thickness. Since the crushing mode of the combined geometry shell was not axisymmetric in experiments, the process was modeled in full. The manufacturing of the combined geometry shells was modeled in a single step. In deep drawing, the die was constrained to move in all directions and rotations. Blank holder and punch were also constrained along radial direction and so did rotations. Blank was located between the die and spring holder and the punch traveled through the die with a trapezoidal velocity curve (Maker and Zhu 2000). This velocity history was lower than the limit for an explicit solver, and thus the mass-scaling method was utilized to obtain the optimum time step size to converge result in a reasonable time (Santosa et al. 2000).

$$c = \sqrt{\frac{E}{\rho(1-\nu^2)}} \qquad (4.1)$$

$$\Delta t_{step} = l_c/c \qquad (4.\ 2)$$

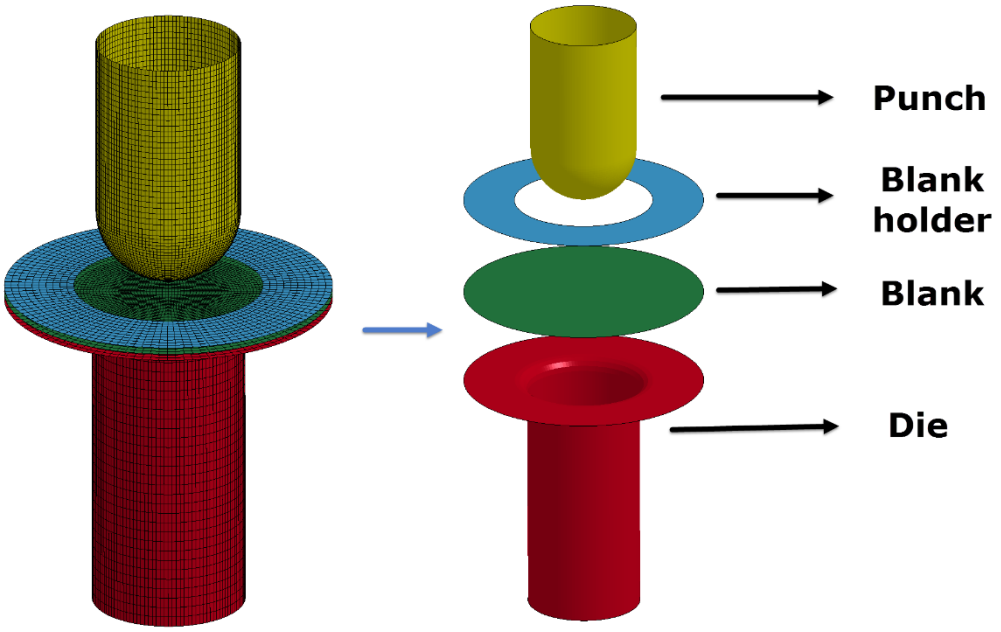

Figure 4.2. Model of deep drawing process.

The elastic wave speed, c, was calculated E, elastic modulus, ν, poison ratio and ρ, density of the material, in Eqn. 4.1. Additionally, time step size was calculated using wave propagation in plane media in terms of l_c, characteristic element length and the elastic wave speed as seen in Equation 4.2. In the mass-scaling method, the density of blank was scaled down 1000 times and the velocity history of punch was set at 10 m/s. Thus, the time step size decreased by a scale of the square root of 1000. The velocity increased by a factor of 100 in order to increase the number of cycles per displacement of the punch in the simulation. The time step size was also controlled using control time step card in the simulation. The ratio of kinetic energy to the total internal energy should be kept lower than 4% to keep the response at static strain rates. In the deep drawing simulation, contact one way surface to surface definition was used. The blank was slave and all other parts were master in the contact definition. The static and dynamic friction coefficients were set to 0.15 and 0.1, respectively. Furthermore, the thickness change and actual thickness usage in contact algorithm were taken into account by activating the option 'THKCHG' and 'SSTHK' in control contact card.

The Johnson Cook material model was used for the blank material. The deformation of the other parts was assumed to be rigid. Thus, all the other parts were modeled with rigid material model. Furthermore, a trapezoidal velocity curve was defined using define curve card and applied to the punch using boundary prescribed motion rigid card. The blank holder force history was important in controlling the tearing or the wrinkling of the blank material. In the current study, a blank holder force of 10 kN was also applied.

Modeling of crushing simulation, the interface spring back lsdyna thickness card was activated to include thickness change, residual stress/strain of the blank material. This card allowed using the deep drawn part for restart simulations by generating a *dynain* file that included all the deep drawing effects. The deep drawing and numerical trimming operation are shown in Figure 4.3.

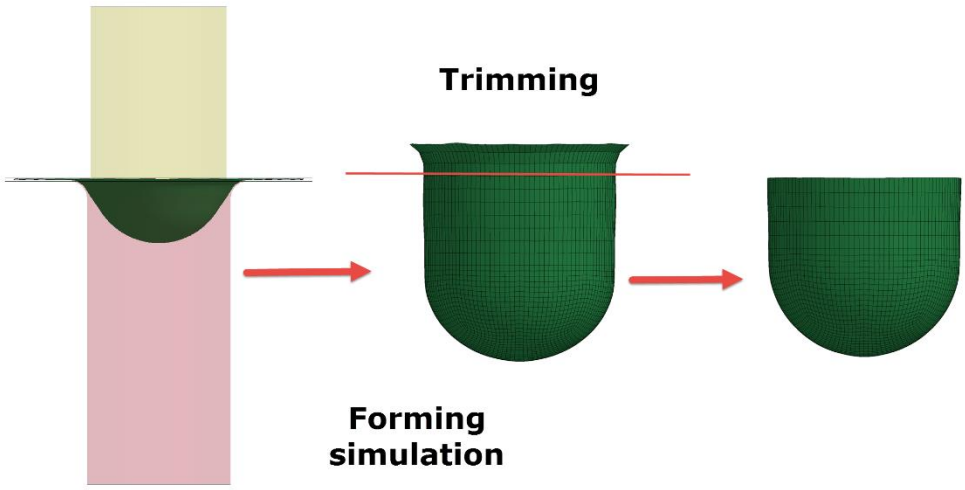

Figure 4.3. Deep drawing and trimming of specimen.

4.2. Numerical Studies of the Crushing Behavior of Combined Geometry Shells

The combined geometry shells were numerical trimmed at desired lengths and imported into the crushing model. The crushing model consisted of a moving top plate, specimen and a stationary bottom plate as seen in Figure 4.4.

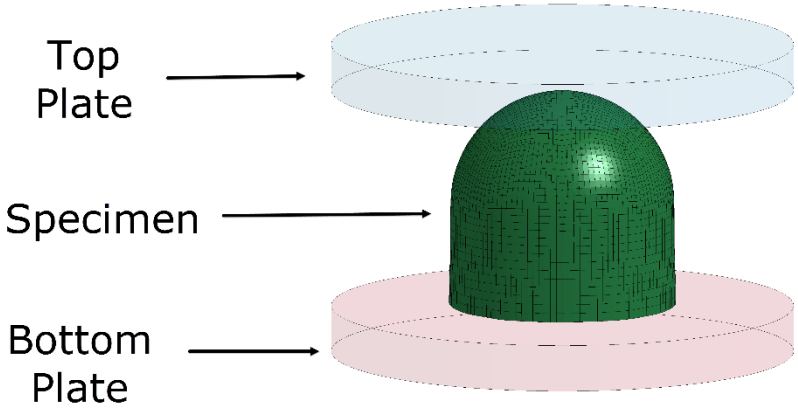

Figure 4.4. Crushing model of the combined geometry shell.

The rigid top and bottom plates were generated using butterfly block mesh generation in ls pre-post. The Johnson Cook material model was used for specimens in lateral crushing simulations. Additionally, the top plate was constrained along radial direction and so did rotations and the bottom plate was constrained to move all directions and rotations. At quasi static strain rates, the mass-scaling method was applied by increasing the crosshead speed of the top plate and reducing the density of the specimens. In addition, the contact eroding surface to surface card was used to account of contact between plates and specimen. The contact eroding single surface card was used for the specimen to consider contacts during the folds formation with including failure. The static and dynamic friction coefficients were selected as 0.3 and 0.2, respectively. In the drop weight simulation, the initial velocity was given to the top plate and the desired masses were added to nodes of the top plate. The initial velocity of top plate was decreasing during collapse until the kinetic energy converted into strain energy by combined geometry shell.

4.2.1. Energy Partitions Between the Hemi-Spherical and Cylindrical Segments

The combined geometry shells consisted of the hemi-spherical and the cylindrical segments. Energy partitions between these segments at quasi static and dynamic strain rates are also significant to understand the crushing behavior in a better way. For this

purpose, in the numerical model the hemi-spherical segment and the cylindrical segment were created separately and a different part id was assigned to each of them.

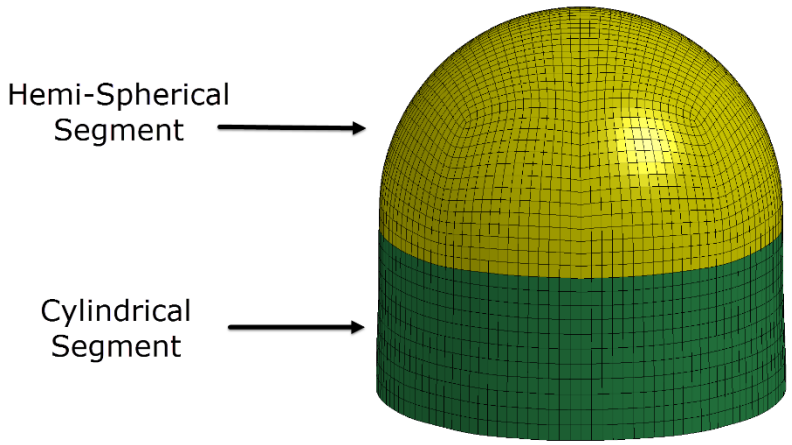

Figure 4.5. The hemi-spherical and the cylindrical segments.

4.2.2. Effect of Temperature

For the sandwich structures subjected to blast loading, the effect of the temperature on the crushing behavior of structure is supposed to become important. The equivalent stress is functions of both temperature and strain rate as given in Eqn. 3.4. In addition, the conversion of plastic work is converted into heat during deformation, Eqn. 4.1 where β, the fraction of plastic work, η, the transient heat transfer constant, C_p, the specific heat , ρ, the material density and ε^p, the plastic strain. The fraction of plastic work is generally taken to be constant 0.9 (Hodowany et al. 2000) and μ value is taken to be 1 for adiabatic process.

$$\Delta T = \mu \, \beta \, \frac{1}{\rho \, C_p} \int_0^{\varepsilon^p} \sigma d\varepsilon \qquad (4.1)$$

In order to understand the effect of temperature, a coupled structural thermal analysis was done. In order to activate a coupled structural analysis, SOLN parameter was set to a value of 2 in the control solution card. The control thermal nonlinear card and the control thermal solver card were also activated while solving this nonlinear transient thermal problem.

CHAPTER 5

RESULTS AND DISCUSSIONS

5.1. Numerical Approach of Manufacturing of the Combined Geometry Shells

The deep drawing was modeled to numerically obtain the combined geometry shells. In deep drawing, the thickness of the combined geometry shells varied. These thickness distributions are given for B1X and B2X of specimens at 0-5-15-25 and 32 mm of punch displacements in Figure 5.1 and Figure 5.2. Additionally, the thickness distributions of S1X and S2X of specimens are given at 0-5-10-15 and 20 mm of punch displacements in Figure 5.3 and Figure 5.4.

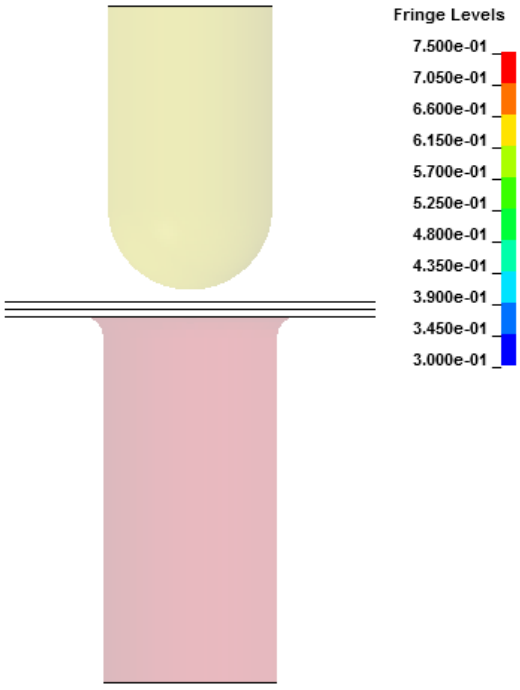

(a)

Figure 5.1. Thickness distributions of B1X specimen at (a) 0 mm, (b) 5 mm, (c) 15 mm, (d) 25 mm and (e) 32 mm of punch displacements.

(cont. on next page)

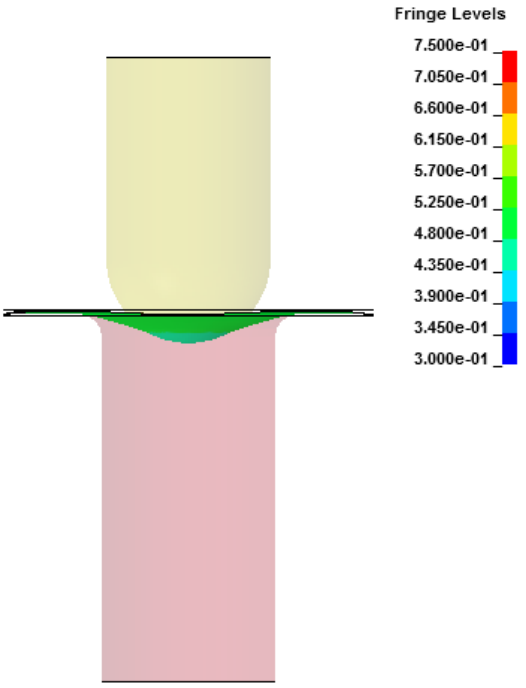

(b)

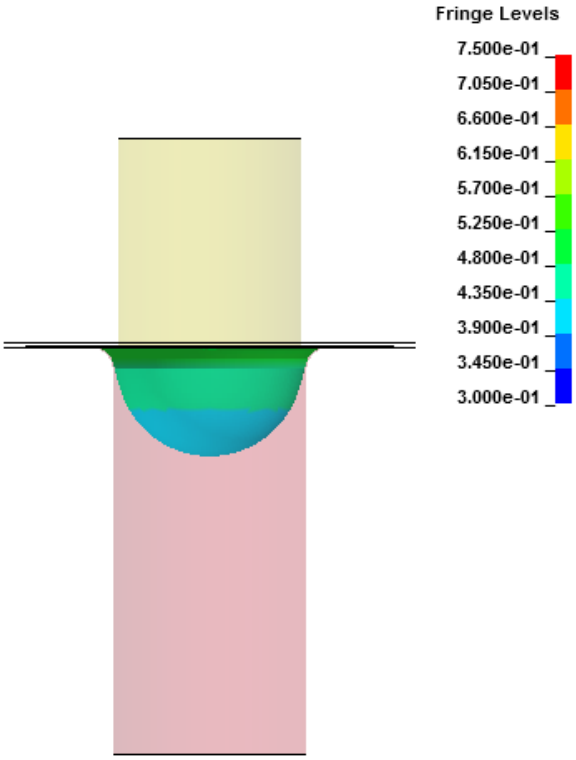

(c)

Figure 5.1. (cont.)

(cont. on next page)

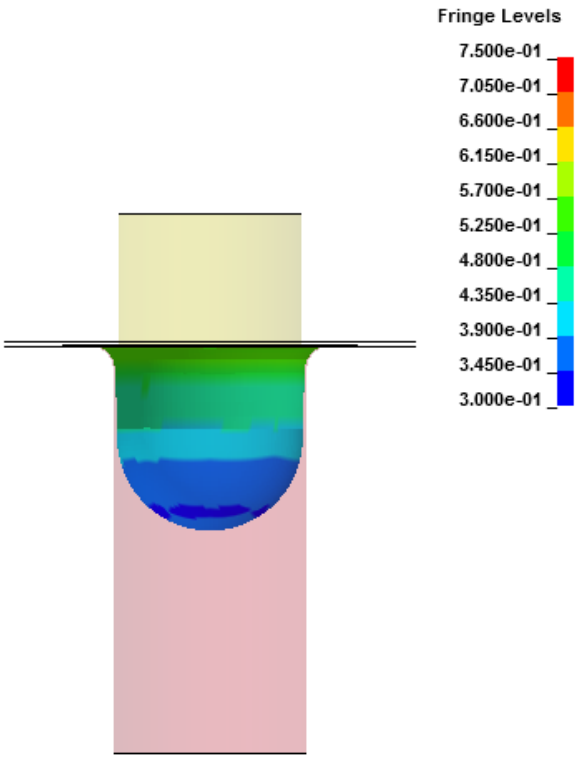

(d)

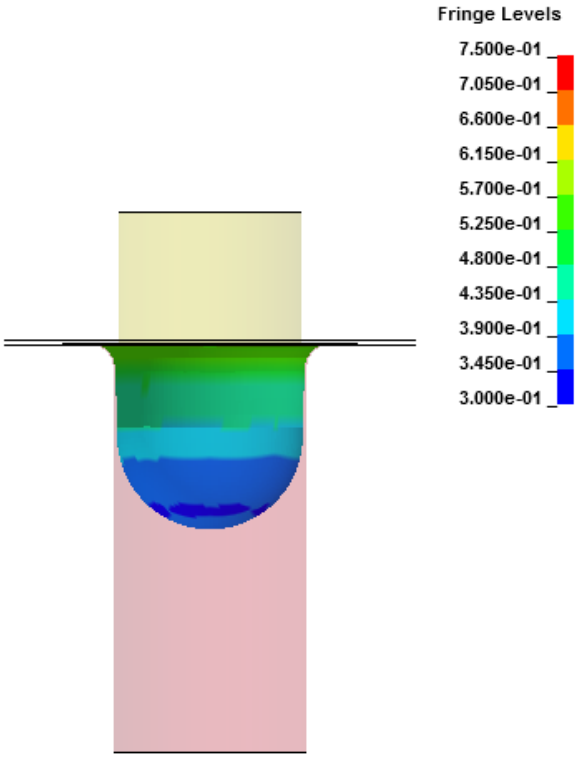

(e)

Figure 5.1. (cont.)

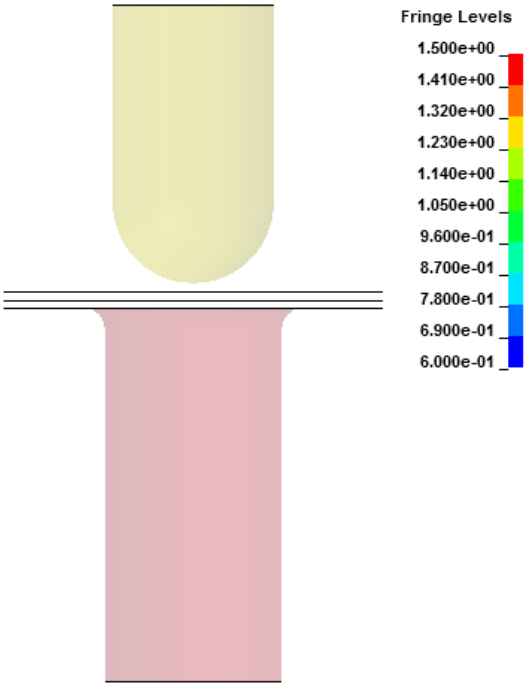

(a)

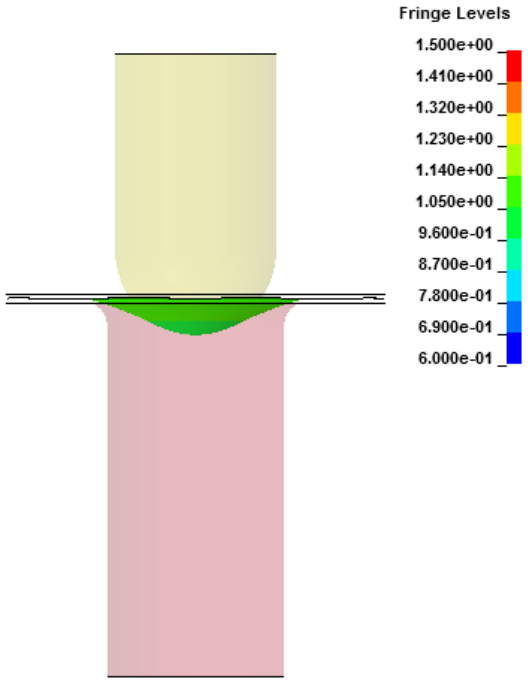

(b)

Figure 5.2. Thickness distributions of B2X specimen at (a) 0 mm, (b) 5 mm, (c) 15 mm, (d) 25 mm and (e) 32 mm of punch displacements.

(cont. on next page)

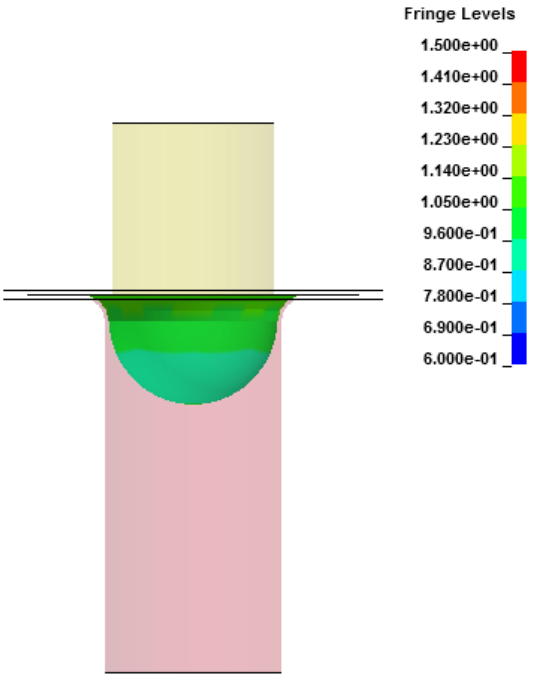

(c)

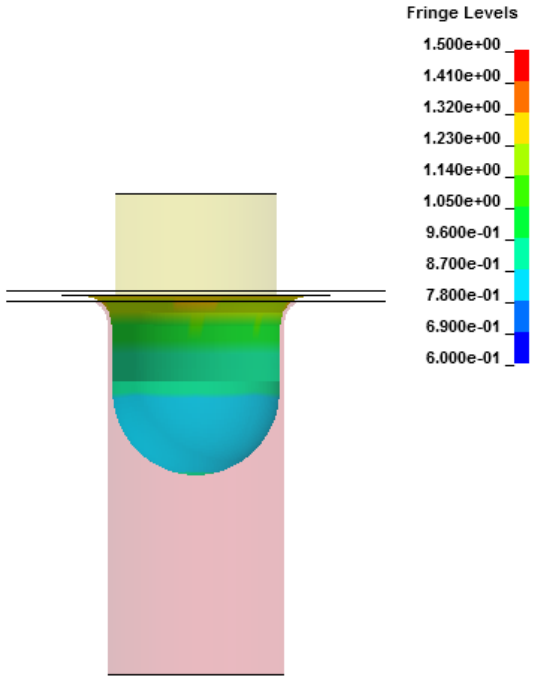

(d)

Figure 5.2. (cont.)

(cont. on next page)

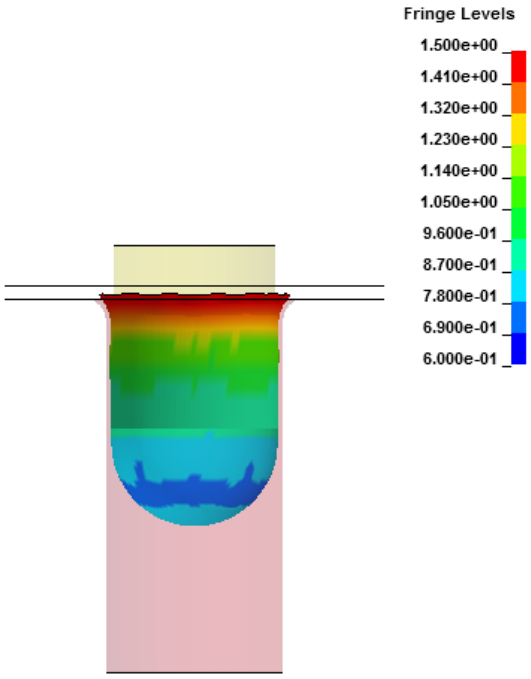

(e)

Figure 5.2. (cont.)

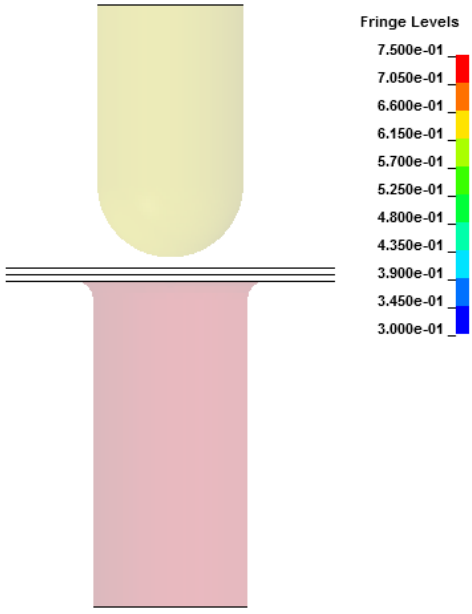

(a)

Figure 5.3. Thickness distributions of S1X specimen at (a) 0 mm, (b) 5 mm, (c) 10 mm, (d) 15 mm and (e) 20 mm of punch displacements.

(cont. on next page)

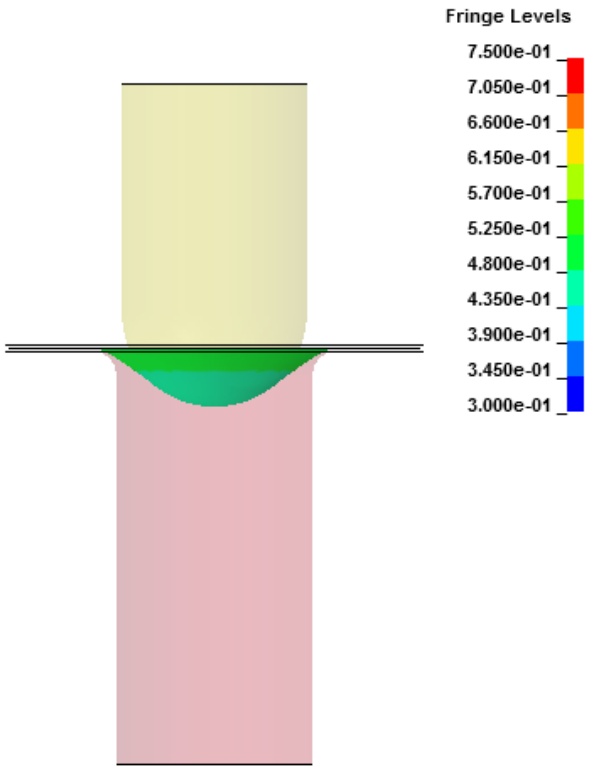

(b)

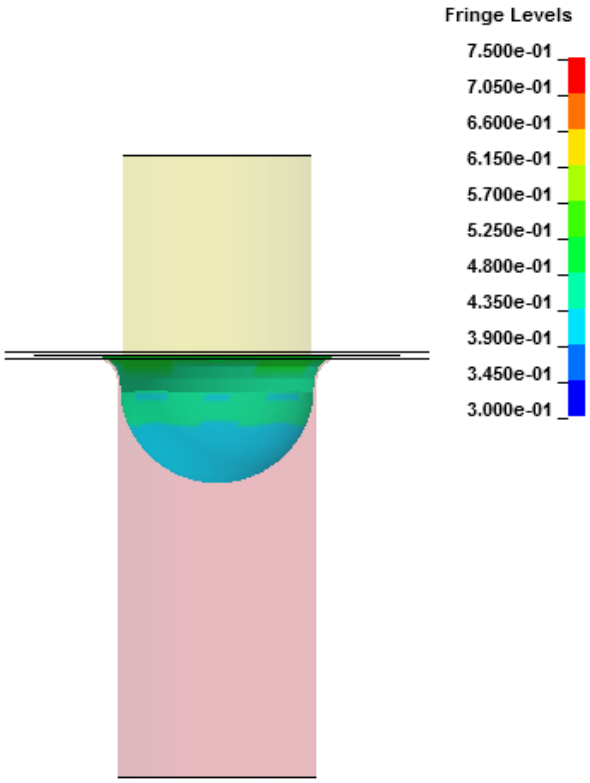

(c)

Figure 5.3 (cont.)

(cont. on next page)

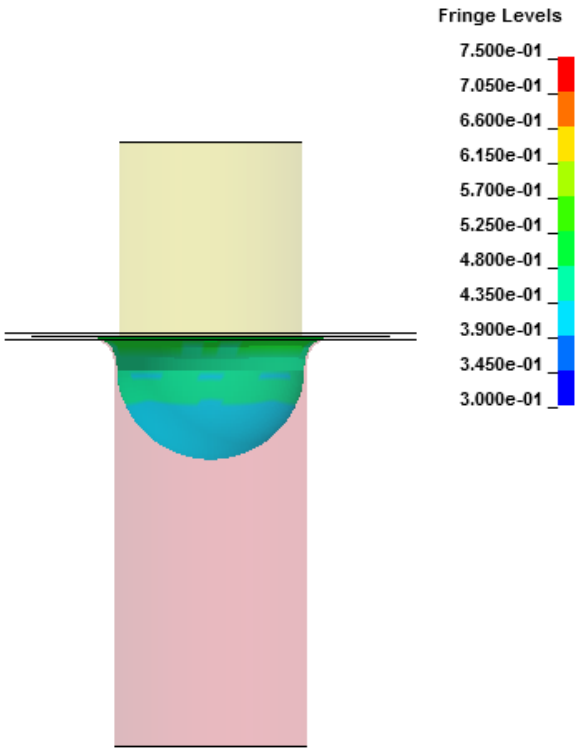

(d)

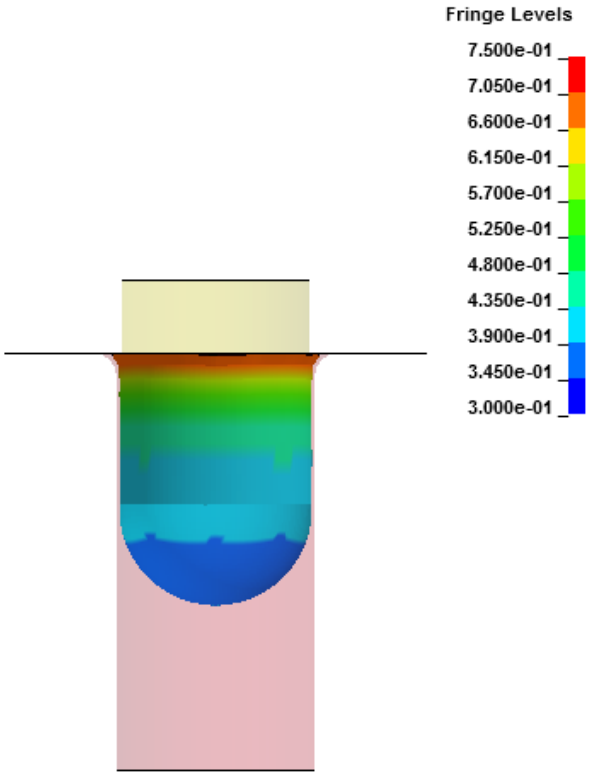

(e)

Figure 5.3. (cont.)

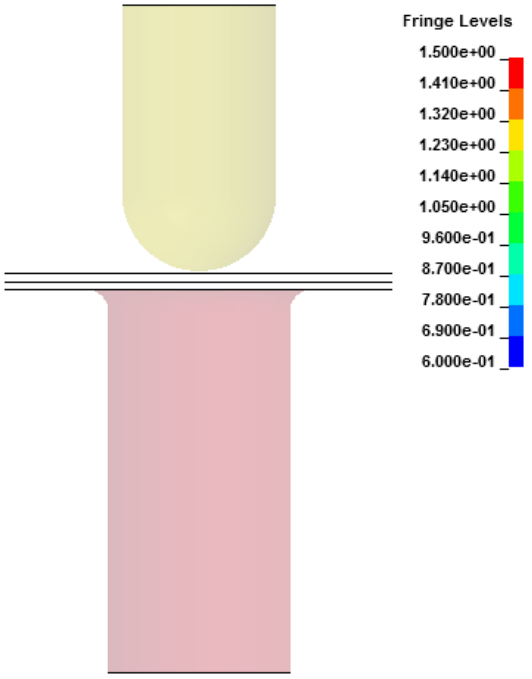

(a)

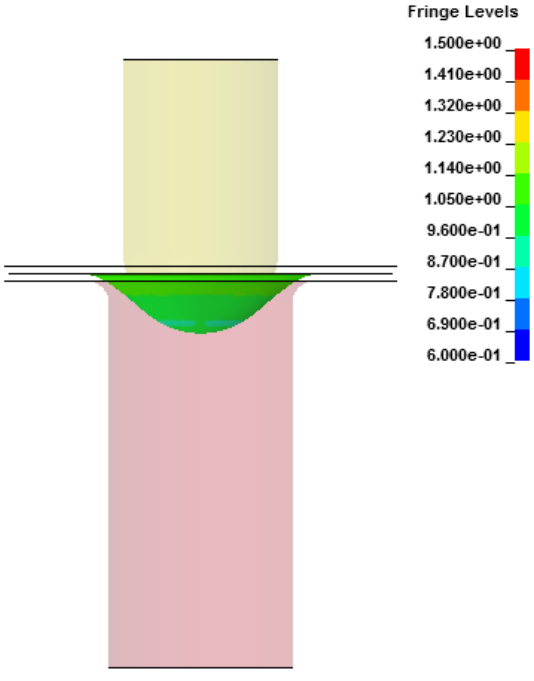

(b)

Figure 5. 4. Thickness distributions of S2X specimen at (a) 0 mm, (b) 5 mm, (c) 10 mm, (d) 15 mm and (e) 20 mm of punch displacements.

(cont. on next page)

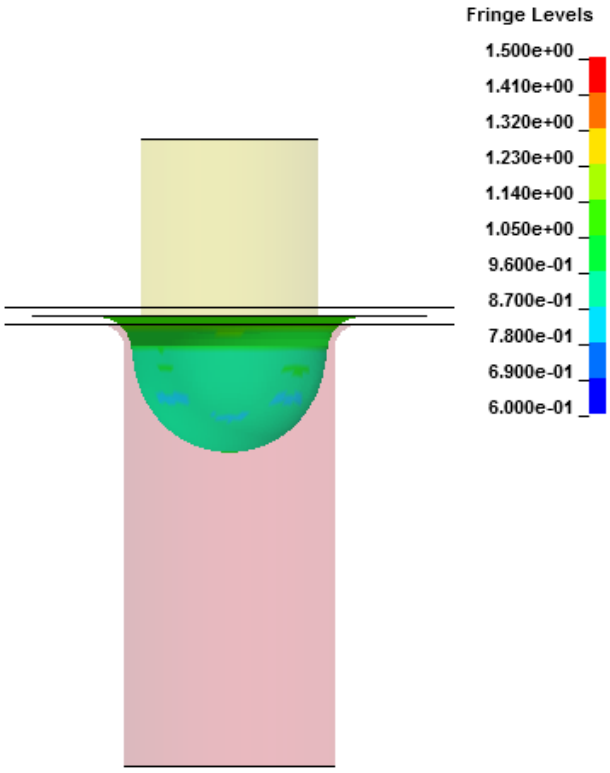

(c)

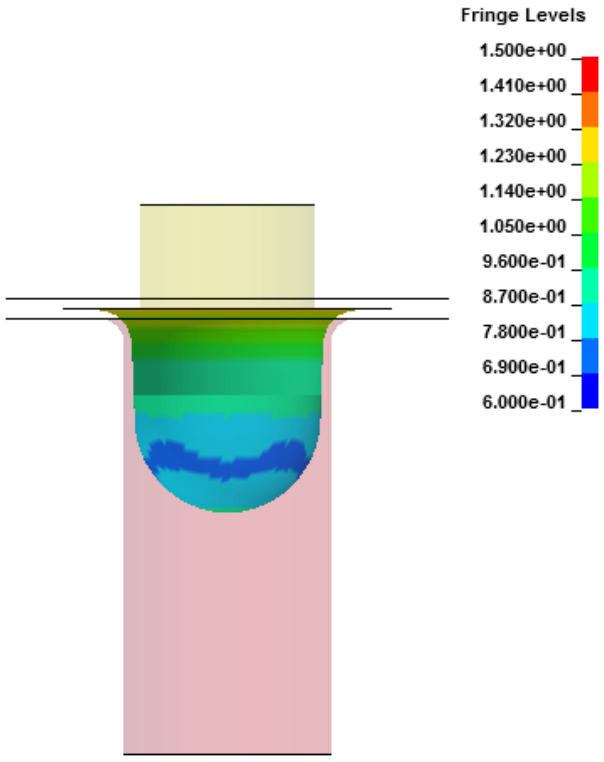

(d)

Figure 5.4 (cont.)

(cont. on next page)

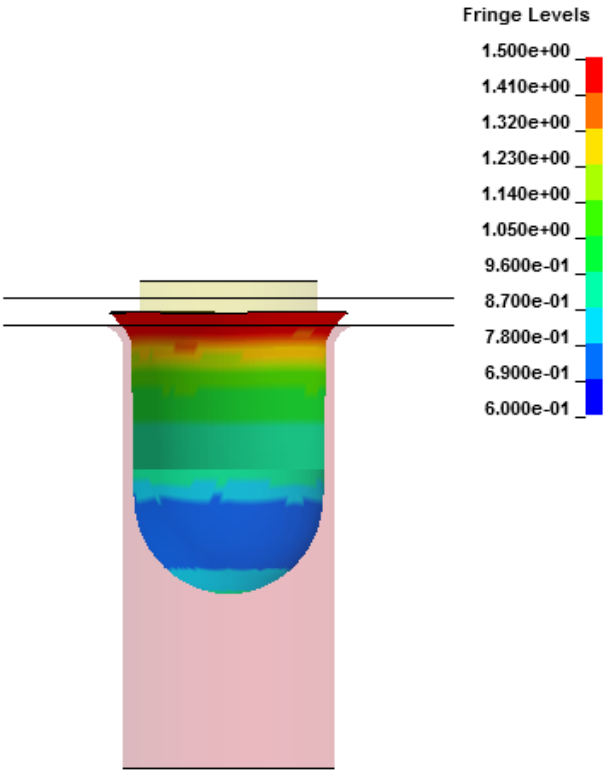

(e)

Figure 5.4. (cont.)

The thickness distribution of combined geometry shells were compared experimentally and numerically. Once there is a good agreement is noted then this numerically generated specimen can further be used in the subsequent crushing simulations. The numerical thickness distribution of the combined geometry shells was compared with the experimental results can be seen in Figure 5.5. There is a close agreement between the experimental and numerical results.

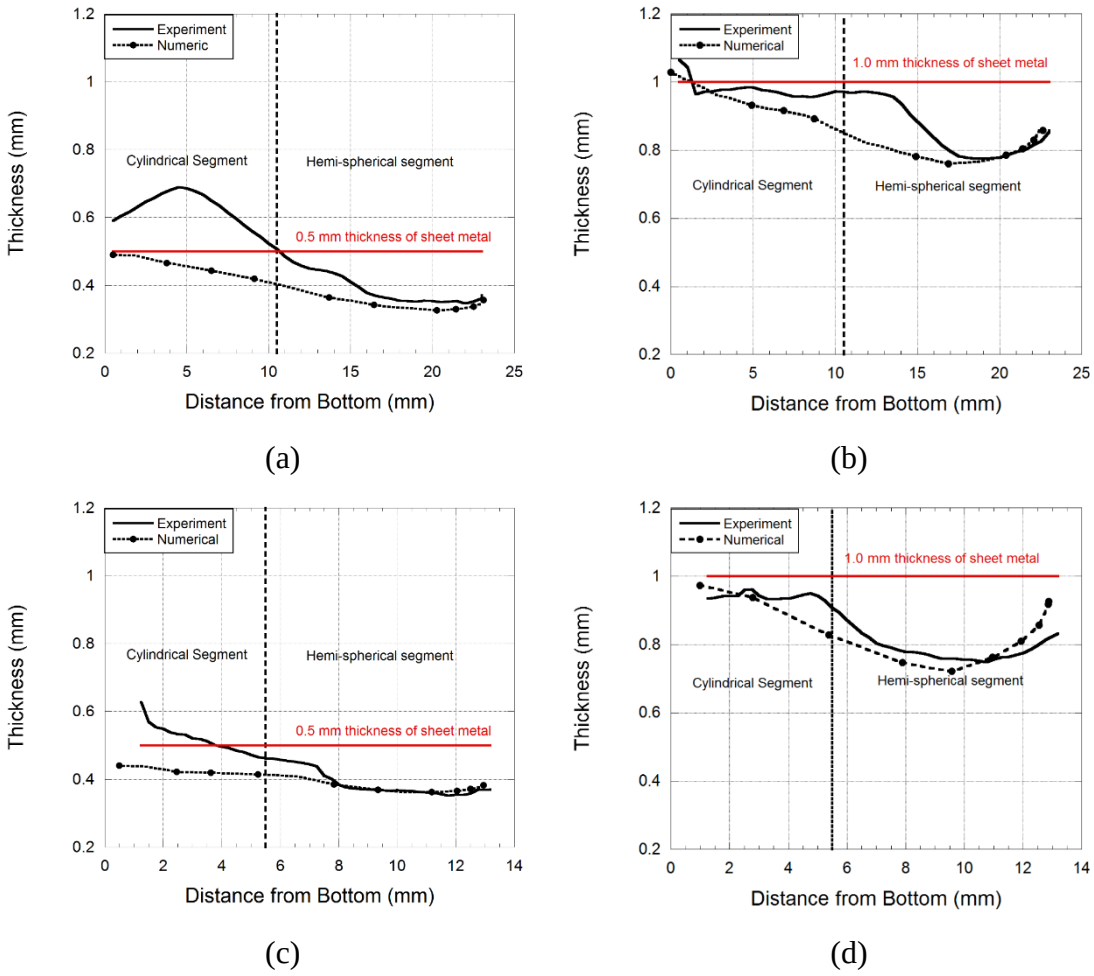

Figure 5.5. Thickness distributions of (a) B1X, (b) B2X, (c) S1X and (d) S2X specimens.

5.2. Investigation of the Crushing Behavior of the Combined Geometry Shells

In this study, the crushing responses of combined geometry shells were investigated experimentally and numerically. At first, compression tests were conducted at quasi-static strain rates using universal testing machine Shimadzu. The low velocity impact tests were conducted using the Fractovis drop weight tower at varying impact velocities with additional masses. Furthermore, the proposed geometries were produced numerically in order to include manufacturing effects. Once the numerical thickness distributions of the combined geometries correlated well with those of experimental, the compression of combined geometry shells were modeled at quasi-static and dynamic strain rates. In this section, the quasi-static compression and dynamic impact tests results were given experimentally and numerically.

5.2.1. Crushing Behavior of the Combined Geometry Shells at Quasi-static and Dynamic Strain Rates

The crushing behavior of the combined geometry shells was investigated in this section in terms of the initial peak force (P_i), the maximum peak force (P_{max}), the mean crushing force (P_{mean}) and the specific absorbed energy (*SAE*). In order to obtain better energy absorption characteristics, the maximum peak force should be kept close to the mean crushing force. For this purpose, the crushing for efficiency (*CFE*) is calculated generally and it is the ratio of mean crushing force to the maximum peak force, Eqn. 5.1.

$$CFE = P_{mean}/P_{max} \tag{5.1}$$

The comparison of the load-displacement curves and the deformation modes at various displacements were given at quasi-static strain rates for B1X specimen, Figure 5.6 and Figure 5.7. The load increased linearly with the deformation of the hemi-spherical segment until the first peak value at which the buckling of the hemi-spherical occurred. During the deformation of the hemi-spherical segment, firstly local flattening, then axisymmetric inward dimpling was observed, Figure 5.7.(b). After that, the first fold formation was occurred and this resulted in a decrease in the crushing force until the compression of the cylindrical segment. Further, compression of cylindrical segment caused on an increase in the crushing force until the second fold formation at which the first buckling of the cylindrical segment occurred at a displacement value of 12 mm. The crushing force decreased after the formation of second fold. The crushing force increased with the further deformation of the cylindrical segment and the similar deformation behavior was observed for the rest. After 19 mm deformation, the densification was reached, Figure 5.6.

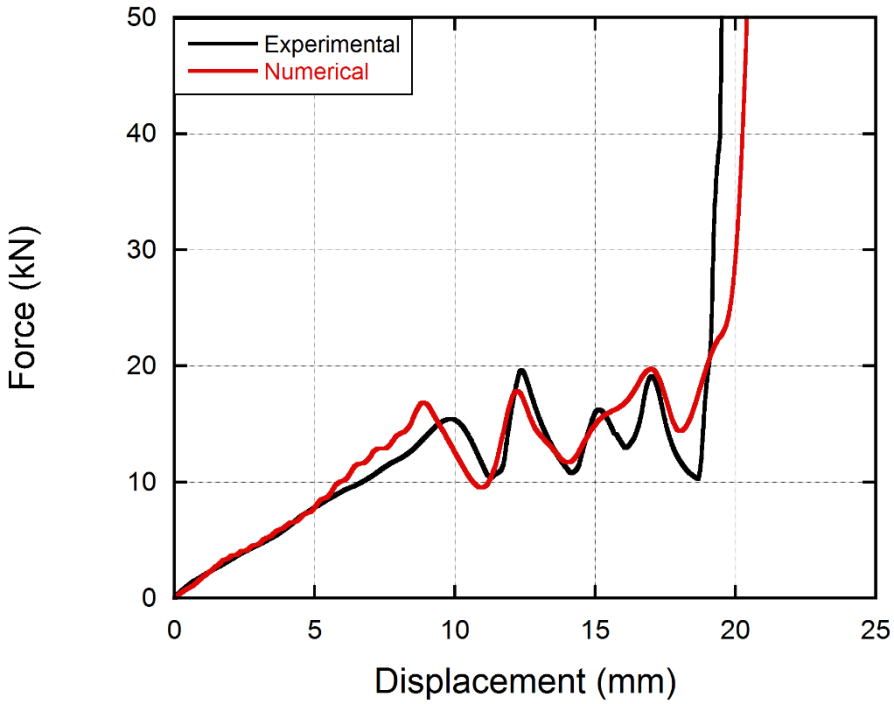

Figure 5.6. Experimental and numerical force-displacement curves of B11.

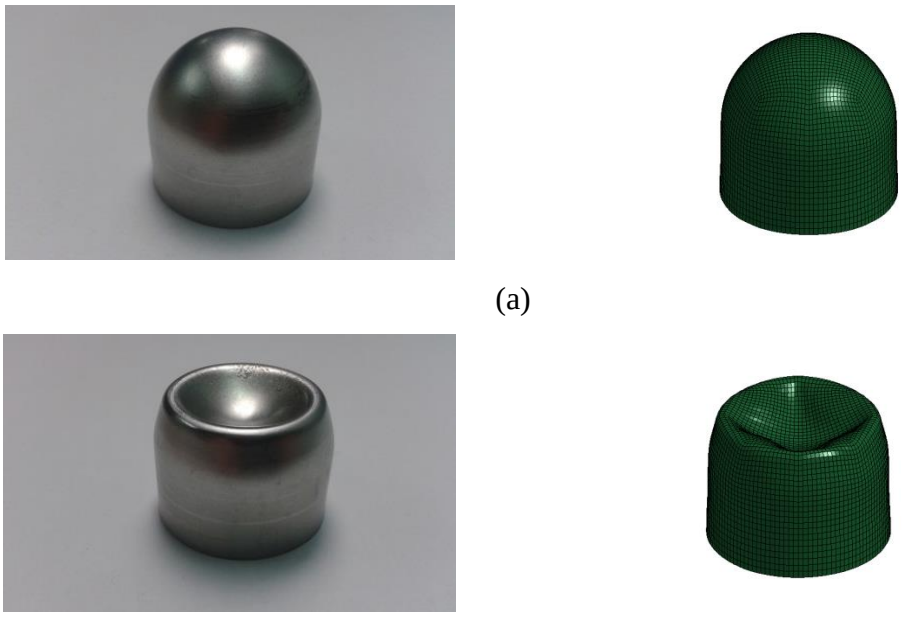

(a)

(b)

Figure 5.7. Experimentally and numerically deformed pictures of B11 at (a) 0 mm, (b) 5 mm, (c) 10 mm, (d) 15 mm and (e) 19 mm of compressions.

(cont. on next page)


(c)


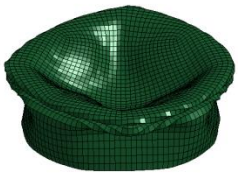

(d)


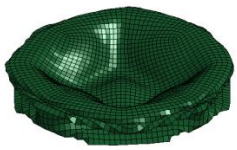

(e)

Figure 5.7 (cont.)

The comparison of load-displacement curves at quasi-static strain rates are given in Figure 5.8, along with the deformation modes at various displacements in Figure 5.9 for the B2X specimen. Axisymmetric inward dimpling of hemi-spherical segment was observed with a bilinear increase in the crushing force until the buckling of hemi-spherical cap completed at 10 mm of compression. After that, the crushing force decreased until to a fold formation in the cylindrical segment. Subsequently, after 17 mm of compression, the densification point was reached.

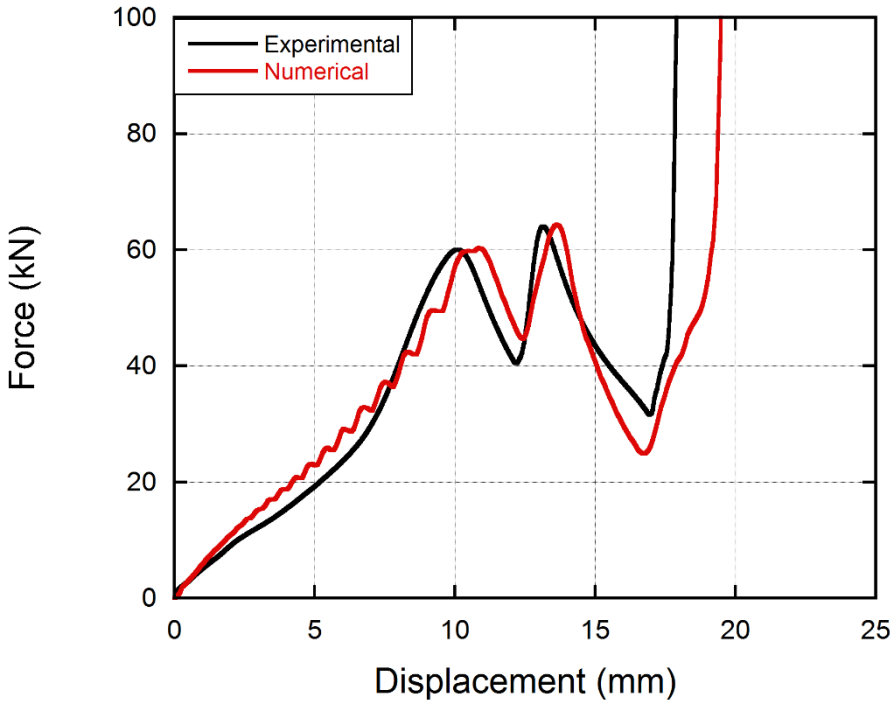

Figure 5. 8. Experimental and numerical force-displacement curves of B21.

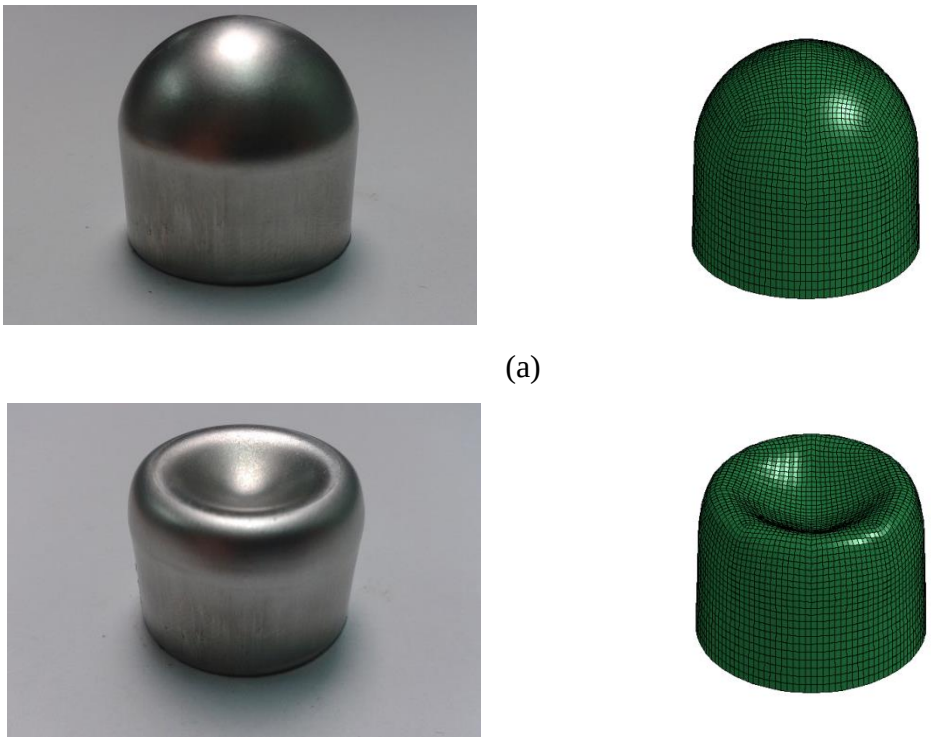

(a)

(b)

Figure 5.9. Experimentally and numerically deformed pictures of B21 at (a) 0 mm, (b) 5 mm, (c) 10 mm, (d) 15 mm and (e) 17.75 mm of compressions.

(cont. on next page)

(c)

(d)

(e)

Figure 5.9 (cont.)

The comparison of load-displacement curves of S2X specimen at quasi-static strain rates is given in Figure 5.10 experimentally and numerically. The deformation modes are also shown in Figure 5.11 at various displacements. The crushing force increased nonlinear with the axisymmetric inward dimpling mode until 6 mm displacement where the buckling of hemi-spherical cap occurred. Then, the crushing force decreased with the formation of first fold in hemi-spherical cap. With further compression of the cylindrical segment, the crushing force increased again until the buckling of the cylindrical segment occurred at 8 mm displacement. The buckling mode of cylindrical segment occurred at 8 mm displacement. The buckling mode cylindrical segment for S11 was different from those of B11 and B21. The cylindrical segment of

S11 deformed asymmetrically during formation of fold and this resulted in lower buckling force, Figure 5.13.

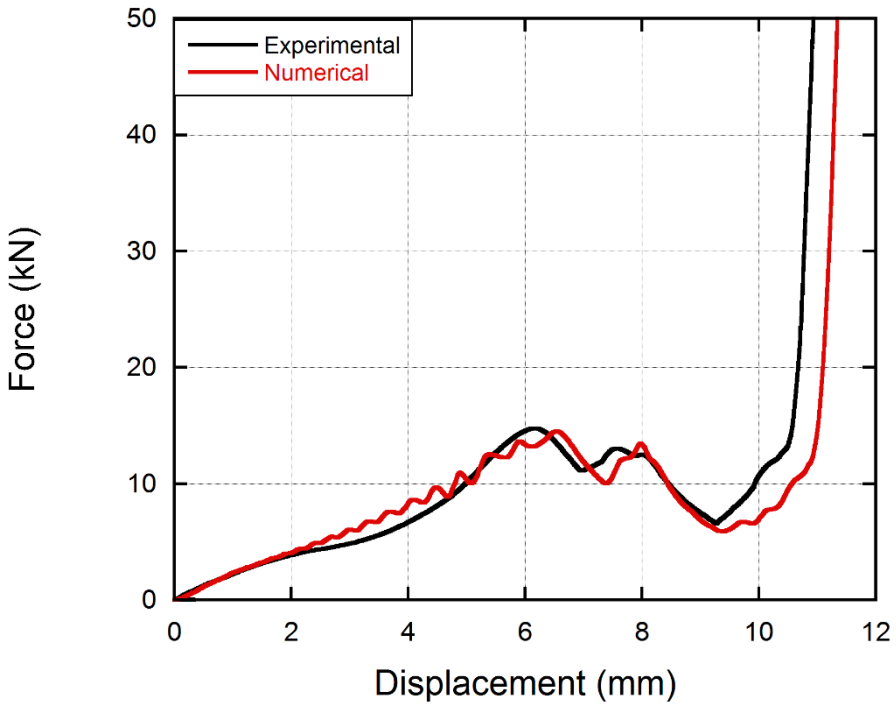

Figure 5.10. Experimental and numerical force-displacement curves of S11.

(a)

(b)

Figure 5.11. Experimentally and numerically deformed pictures of S11 at (a) 0 mm, (b) 4 mm, (c) 6 mm, (d) 9 mm and (e) 10 mm of compressions.

(cont. on next page)

(c)

(d)

(e)

Figure 5.11 (cont.)

The comparison of load-displacement curves for S2X specimen at quasi-static strain rates are given experimentally and numerically in Figure 5.12. The deformation modes of S21 specimen are given in Figure 5.13 at various displacements. The crushing force of S21 increased bilinear with the inward dimpling of hemi-spherical segment. After 7 mm of displacement, the formation of fold of the cylindrical segment was observed. That resulted in an increase in the crushing force until 8 mm of displacement. The crushing force decreased until the formation of fold and increased suddenly at the densification point at approximately 9 mm of displacement.

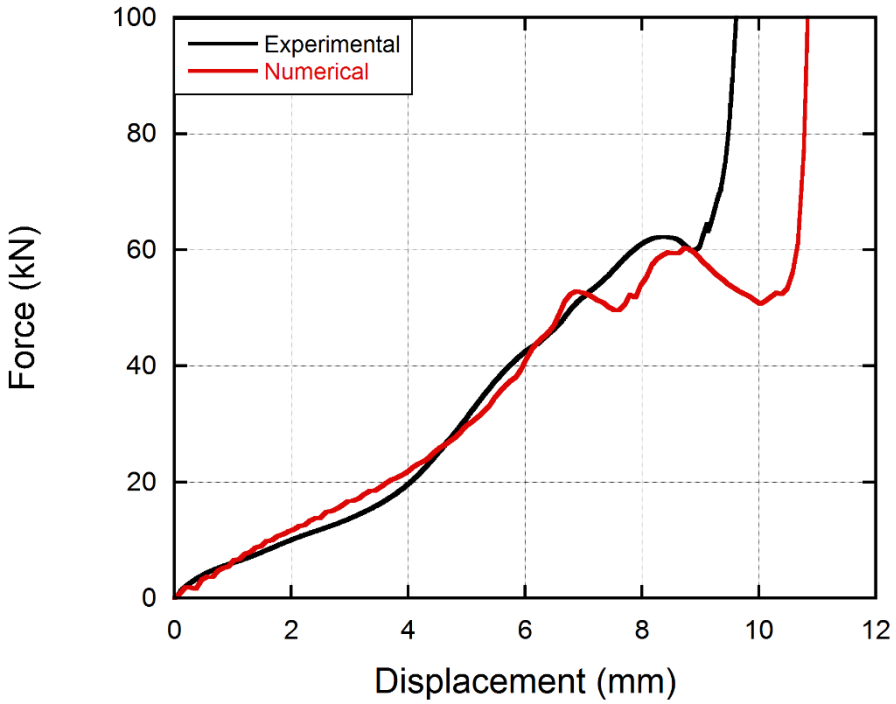

Figure 5.12. Experimental and numerical force-displacement curves of S21.

(a)

(b)

Figure 5.13. Experimentally and numerically deformed pictures of S21 at (a) 0 mm, (b) 4 mm, (c) 7 mm, (d) 9 mm and (e) 10 mm of compressions.

(cont. on next page)

(c)

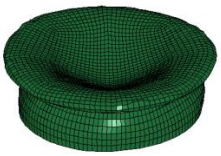

(d)

(e)

Figure 5.13 (cont.)

The crushing behavior of combined geometry shells was also investigated at dynamic strain rates in this thesis. The low velocity impact tests were performed using the Fractovis drop weight tower with required velocities and additional masses. The comparison of load-displacement curves of B12 is given in Figure 5.14. The crushing load increased with a mode of axisymmetric inward dimpling in the hemi-spherical segment as seen in Figure 5.16.(b). After the formation of the fold, the crushing load decreased until the compression of cylindrical segment started and the crushing load increased again with asymmetric deformation until the buckling of the cylindrical segment occurred. Then the crushing load decreased sharply and increased again with the formation of the number of lobes in the cylindrical segment. The crushing load started to increase at the densification point at 20 mm of deformation.

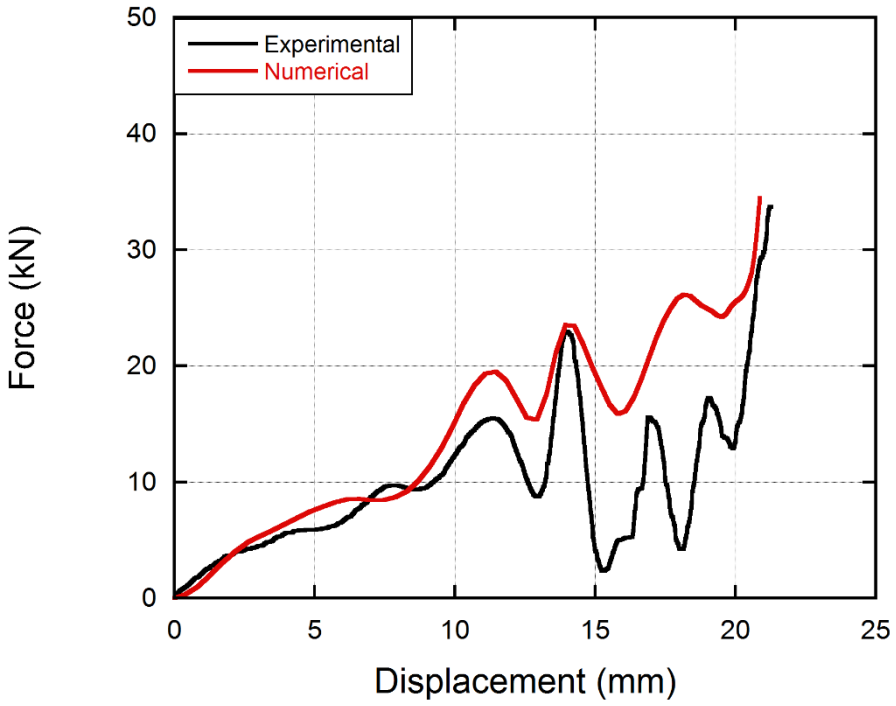

Figure 5.14. Experimental and numerical force-displacement curves of B12.

Figure 5.15. Deformed views of B12.

The deformation mode of B12 was similar with that of quasi statically tested until 9 mm of deformation. However, the deformation of the cylindrical segment differed from the deformation at quasi static strain rate. Although the axisymmetric formation of folds were observed at quasi-static strain rate, the number of lobes in the deformation of the cylindrical segment at dynamic strain rate can be seen in seen Figure 5.16.(e) . That resulted a decrease in the crushing force. The last deformation stages of B1X specimen were seen in Figure 5.15.

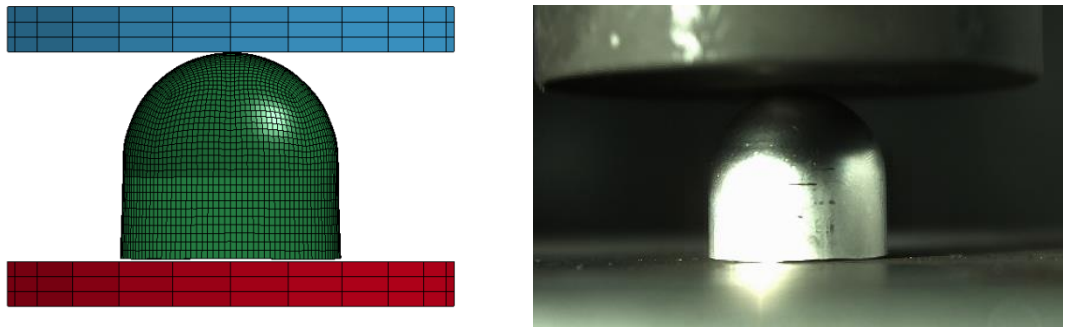

(a)

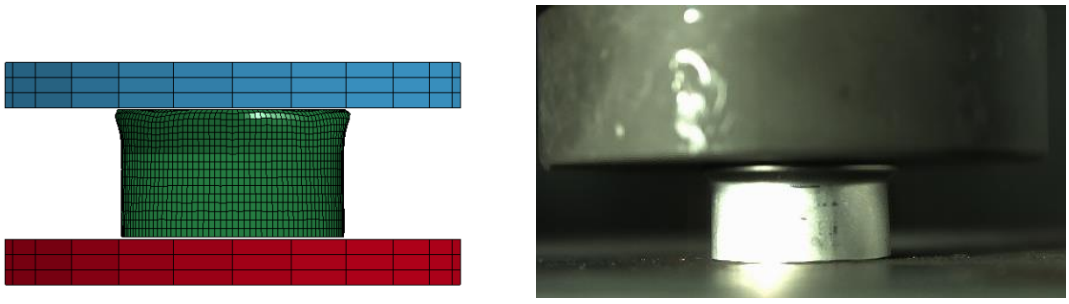

(b)

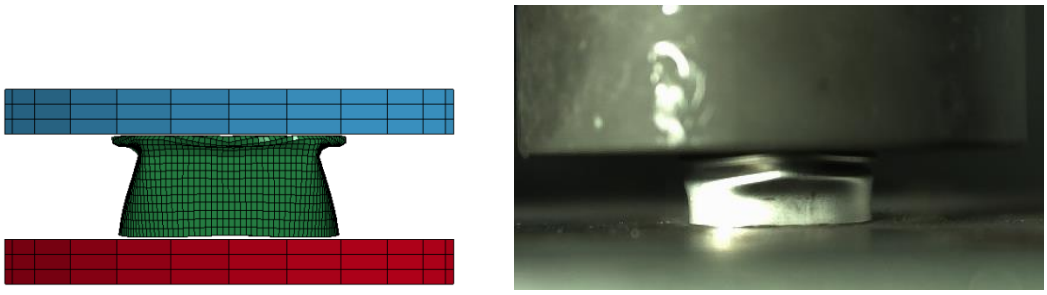

(c)

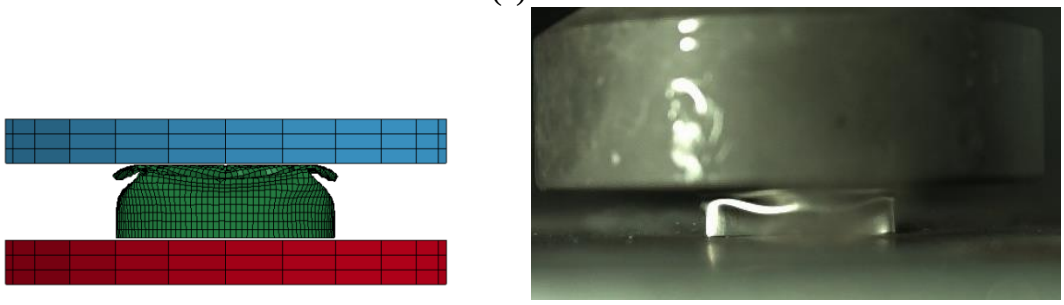

(d)

Figure 5.16. Experimentally and numerically deformed pictures of B12 at (a) 0 mm, (b) 9.8 mm (c) 13.1 mm, (d) 16.3 mm and (e) 19.6 mm of compressions.

(cont. on next page)

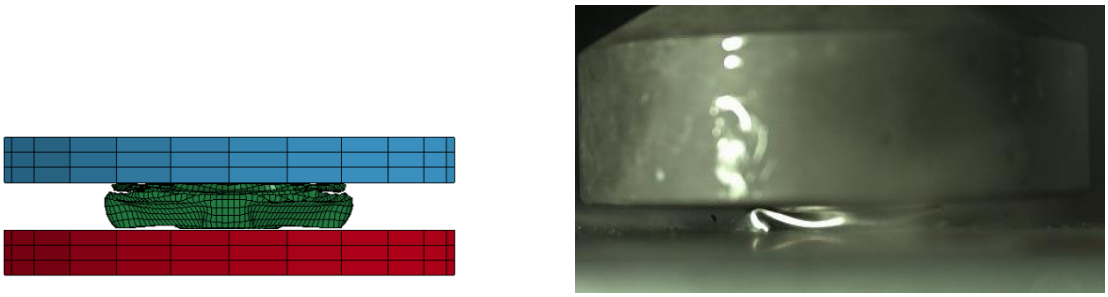

(e)

Figure 5.16. (cont.)

The comparison of load-displacement curves of B22 is given in Figure 5.17. The deformation modes are shown in Figure 5.19 at various displacements. In addition, the last deformation stage of B22 is shown in Figure 5.18. The crushing load increased while the hemi-spherical segment deformed with a mode of axisymmetric inward dimpling. Then, the crushing load reached an initial peak force value at which the buckling of hemi-spherical segment occurred and the formation of fold was observed, Figure 5.19.(c). When the fold was completed, the failure was seen at the junction of the hemi-spherical and the cylindrical segments due to reduced plastic failure strain as seen in Figure 5.19. (d). That caused a reduction in the crushing load. After that, the crushing load increased again with further compression of the cylindrical segment.

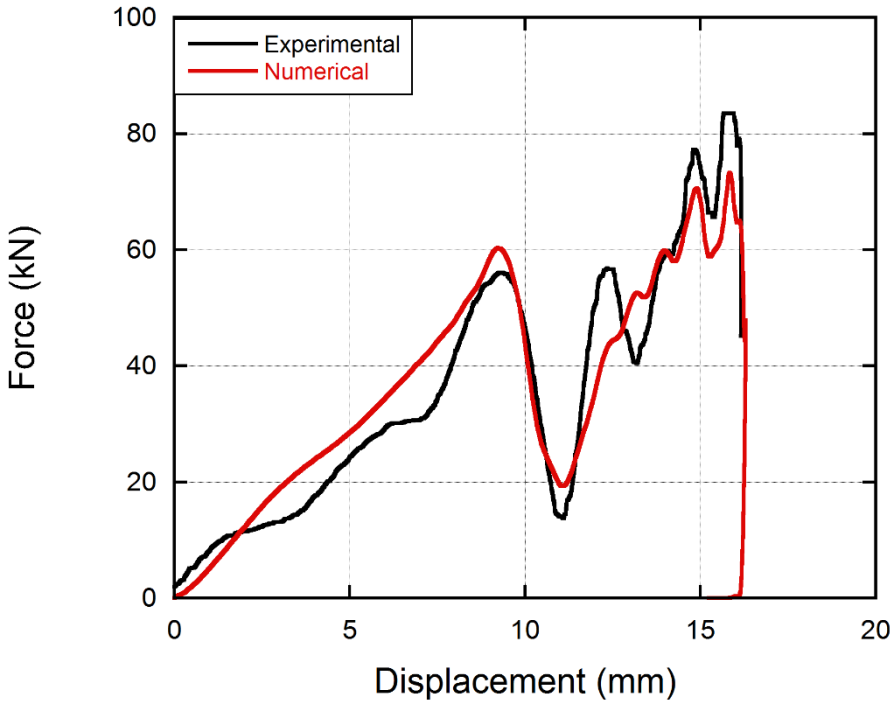

Figure 5.17. Experimental and numerical force-displacement curves of B22.

Figure 5.18. Deformed views of B22.

The crushing behavior of B2X specimen subjected to dynamic loading differed from quasi-static strain rate. Although the crushing load increased linearly with the axisymmetric deformation in the hemi-spherical segment, the crushing load increased bilinear in the hemi-spherical segment at higher strain rates. In addition, there was no failure in the compression at quasi-static strain rate (B21), but at dynamic rates there was.

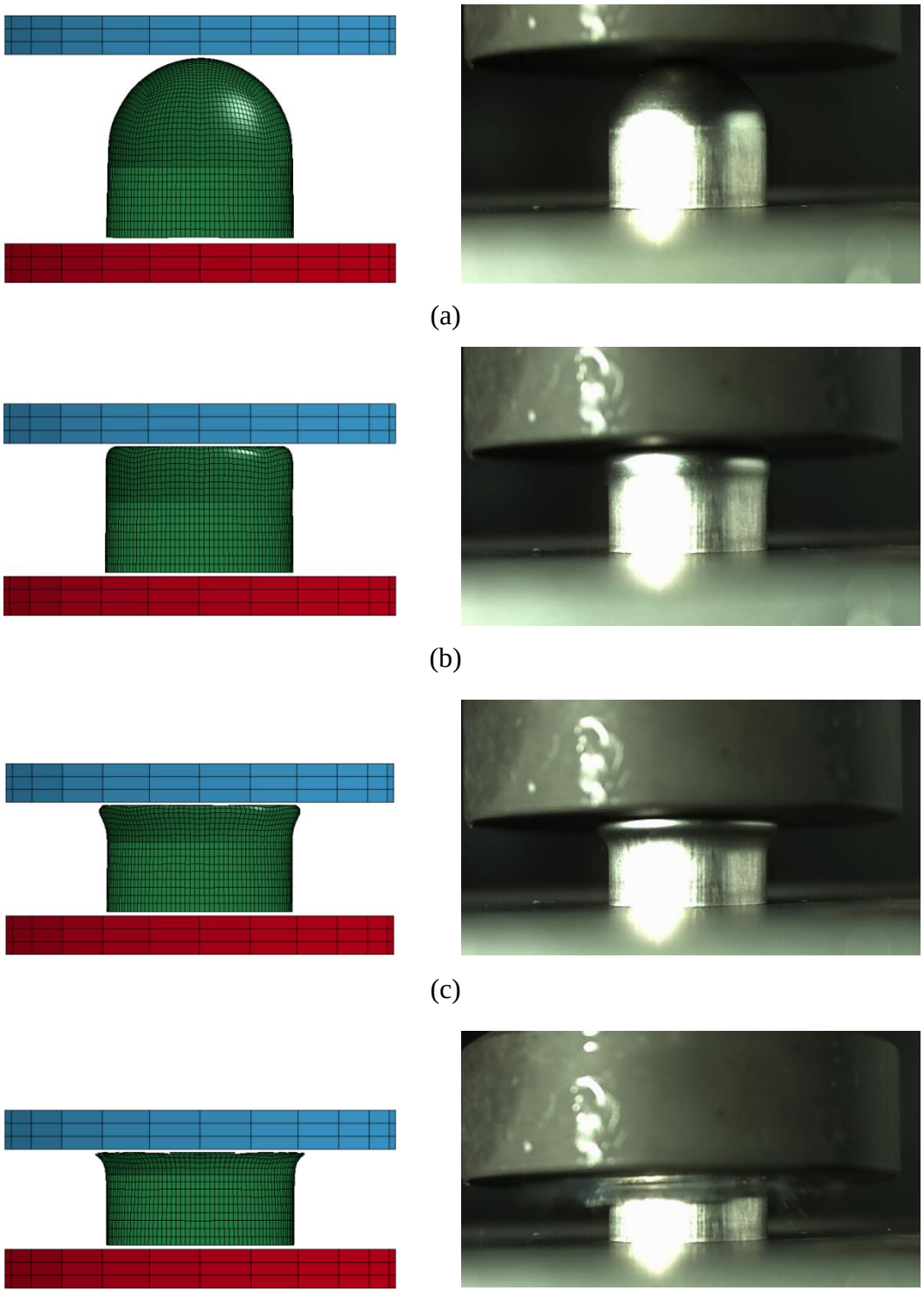

Figure 5.19. Experimentally and numerically deformed pictures of B22 at (a) 0 mm, (b) 7.4 mm, (c) 9.6 mm, (d) 12.6 mm and e) 13.4 mm of compressions.

(cont. on next page)

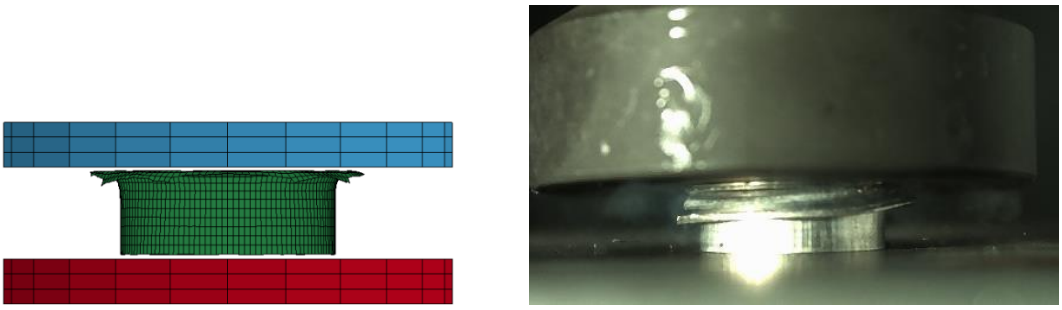

(e)

Figure 5.19. (cont.)

The comparison of the load-displacement curves of S12 is given in Figure 5.20 and the deformation modes are shown in Figure 5.22 at various displacements. The last deformation stages of S12 are illustrated in Figure 5.21. The deformation mode of S12 closely resembles that of B12.

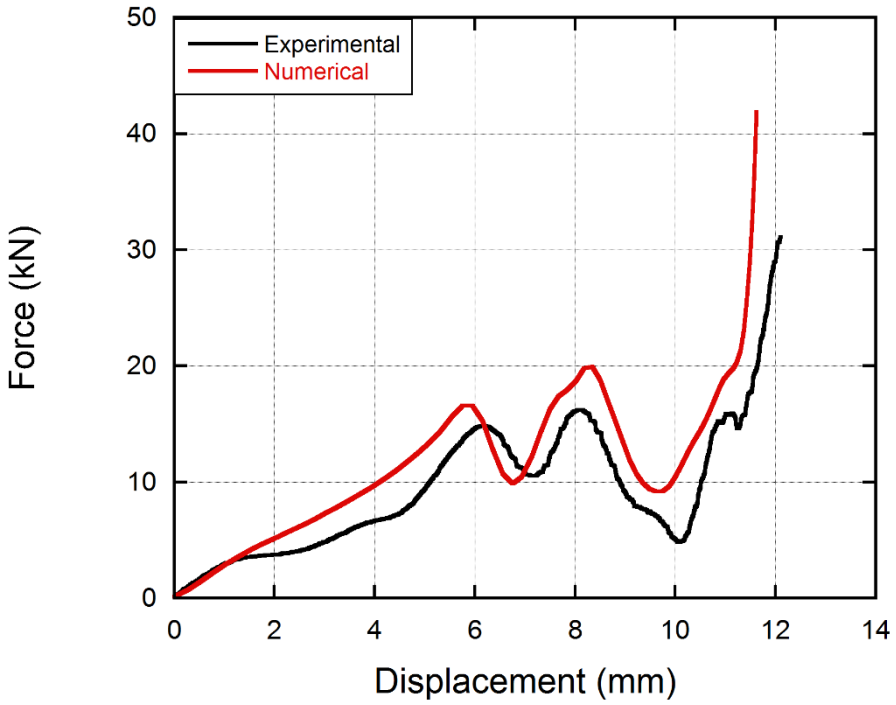

Figure 5.20. Experimental and numerical force-displacement curves of S12.

Figure 5.21. Deformed views of S12.

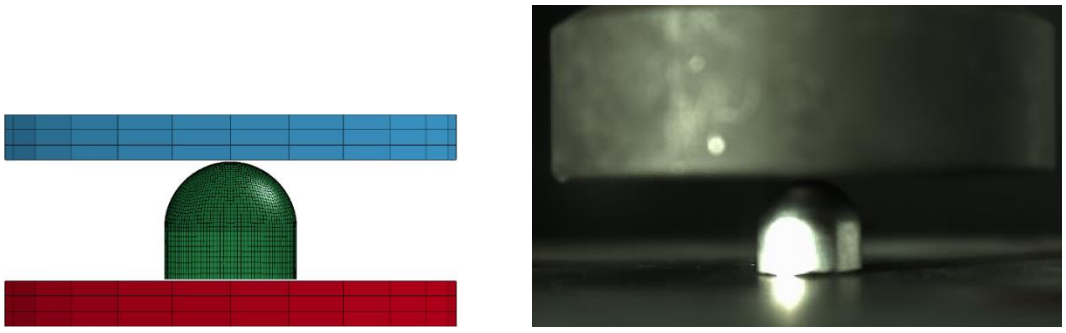

(a)

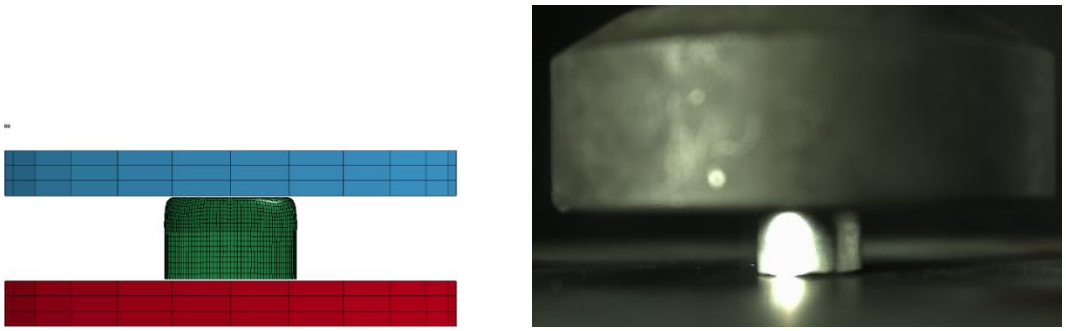

(b)

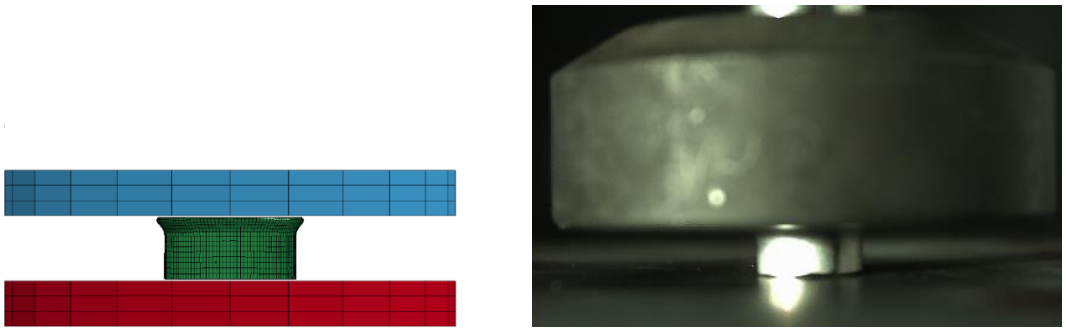

(c)

Figure 5.22. Experimentally and numerically deformed pictures of S12 at (a) 0 mm, (b) 4 mm, (c) 6.1 mm, (d) 8.4 mm and (e) 9.1 mm of compressions.

(cont. on next page)

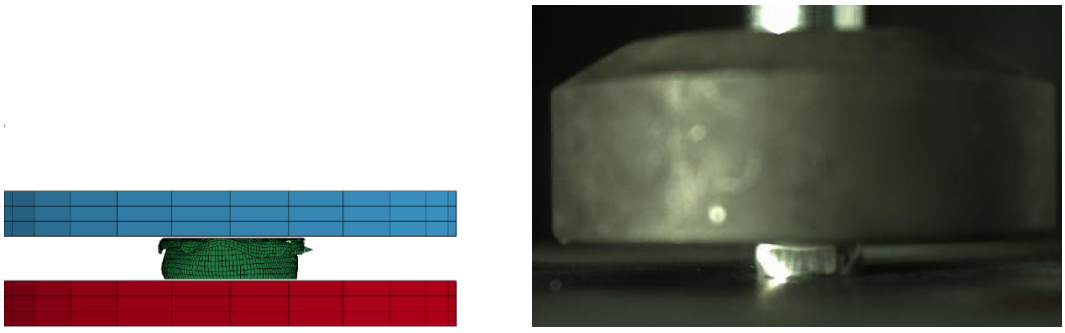

(d)

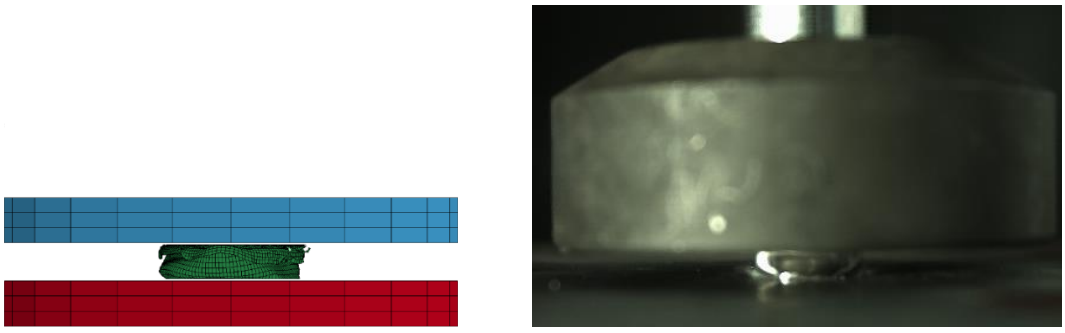

(e)

Figure 5.22. (cont.)

The comparison of load-displacement curves of S22 is given experimentally and numerically in Figure 5.23 and the deformation modes are shown at various displacements in Figure 5.25. The last deformation stages are shown in Figure 5.24. The deformation mode closely resembles that of B22.

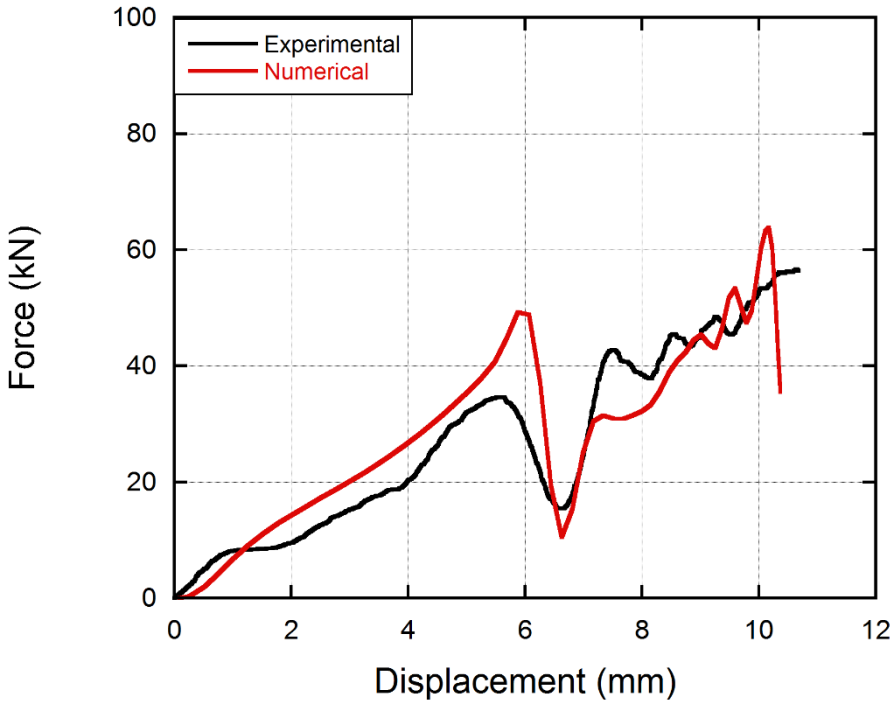

Figure 5.23. Experimental and numerical force-displacement curves of S22.

Figure 5.24. Deformed views of S22.

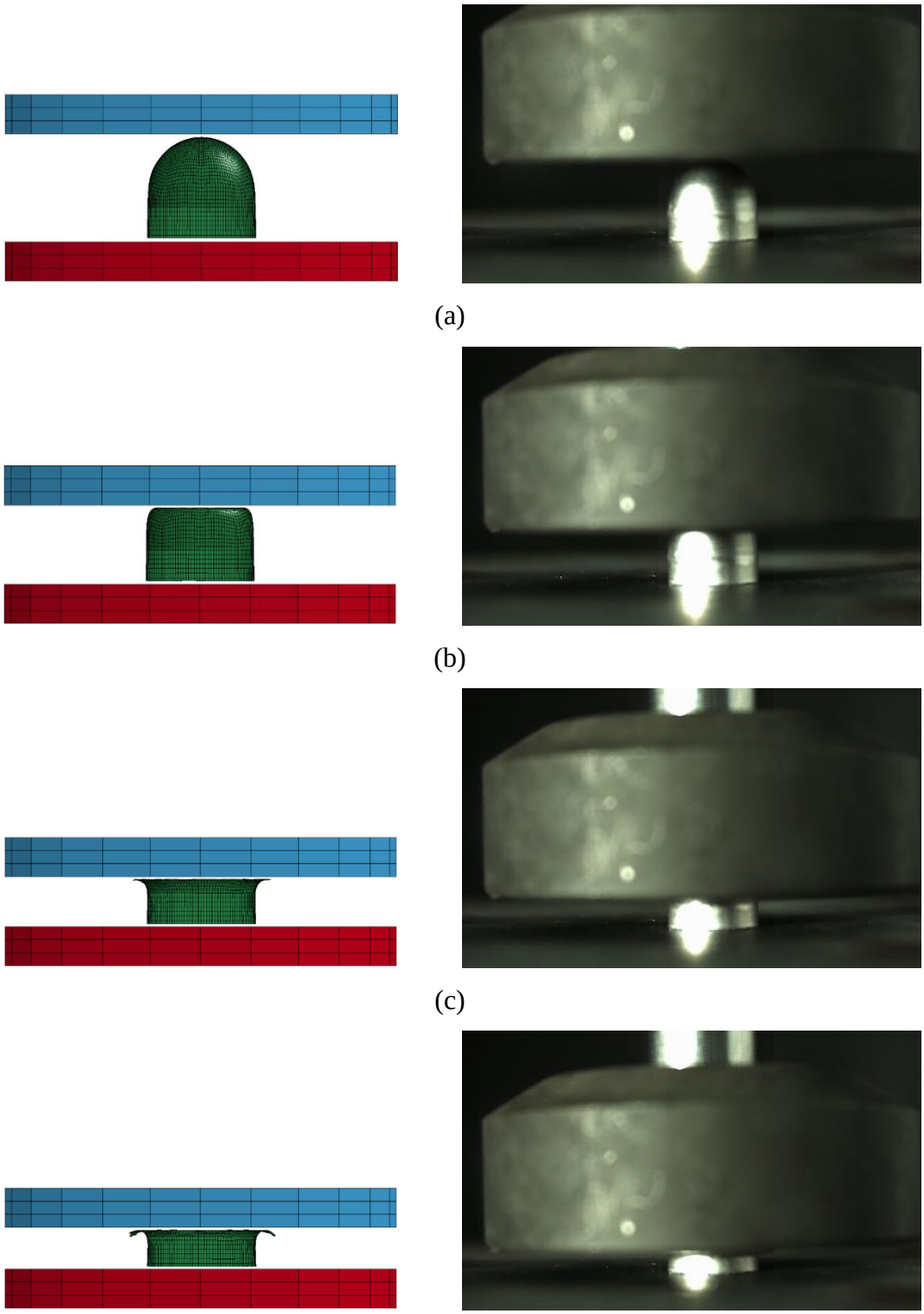

(a)

(b)

(c)

(d)

Figure 5.25. Experimentally and numerically deformed pictures of S22 at (a) 0 mm, (b) 4 mm, (c) 7.8 mm, (d) 8.7 mm, (e) 9.8 mm.

(cont. on next page)

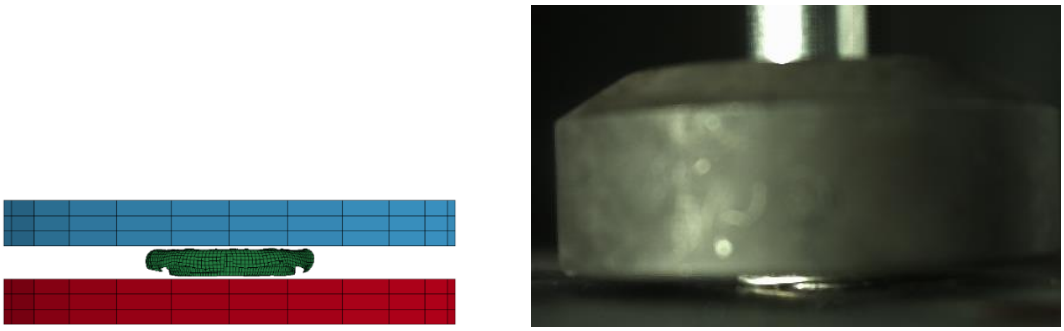

(e)

Figure 5. 25. (cont.)

The dimensional characteristics like the radius to thickness (R/t) ratio and length (L) and the crushing related parameters: P_i, P_{max}, P_{mean}, *SAE*, *CFE* and displacement values are given experimentally and numerically at quasi-static and dynamic strain rates in Table 5.1. When the crushing parameters were compared in terms of R/t and L values, the highest P_i value was attained in S21 as 62.7 kN, whereas the lowest was in S11 as 14.8 kN. In addition, the P_{max} value was found in B22 (77.1 kN), while the lowest was in S11 again as 14.8 kN. Furthermore, the highest P_{mean} value was observed in B21 as 33.9 kN, whereas the lowest was in S11 as 7.9 kN.

It was obviously seen that the crushing behavior of a combined geometry shells was a function of R/t and L. For the same diameter and length of the specimen, P_i, P_{max} and P_{mean} increased as R/t ratios decreased. For smaller specimen (length of 13 mm) the P_i, P_{max} and P_{mean} values increased as R/t values decreased.

Table 5.1. Experimental and numerical results of combined geometry shells.

Specimen	R/t (mm/mm)	L (mm)	Result	Pi (kN)	Pmax (kN)	Pmean (kN)	Energy (J)	SAE (kJ/kg)	CFE (kN/kN)	Compression (mm)
B11	25	23.06	Experiment	15.5	19.6	10.7	203.8	34.0	0.54	19.0
			Numerical	17.0	19.8	11.5	220.2	36.7	0.58	19.1
B12	25	22.80	Experiment	15.4	29.0	9.3	189.7	31.6	0.32	20.5
			Numerical	19.6	26.1	13.9	282.2	47.0	0.53	20.4
B21	12.5	22.62	Experiment	59.8	64.0	33.9	600.0	50.0	0.52	17.7
			Numerical	59.7	64.2	35.0	666.3	55.5	0.54	19.0
B22	12.5	22.95	Experiment	56.1	77.1	33.5	525.1	43.8	0.43	15.7
			Numerical	60.1	73.0	35.6	563.5	47.0	0.48	15.8
S11	15	13.01	Experiment	14.8	14.8	7.9	79.3	39.6	0.53	10.0
			Numerical	14.3	14.3	8.1	90.0	45.0	0.56	11.1
S12	15	13.05	Experiment	14.9	16.2	8.5	96.5	48.2	0.52	11.3
			Numerical	16.5	19.9	10.9	124.3	62.2	0.54	11.4
S21	7.5	13.06	Experiment	62.7	62.7	33.3	323.6	107.9	0.53	9.7
			Numerical	52.7	60.1	32.9	348.1	116.0	0.54	10.6
S22	7.5	13.02	Experiment	34.8	48.8	27.1	289.3	96.4	0.55	10.7
			Numerical	51.1	63.3	27.2	272.5	90.8	0.42	10.0

The comparison of *CFE* and *SAE* values is given in Figure 5.26. When the experimental results were compared, the *CFE* values were almost similar in quasi-static strain rate range, however the *CFE* values decreased at dynamic strain rates except S2X specimen. The highest *CFE* value was calculated in S22 (0.55), whereas the lowest value was calculated for B12 (0.32). The highest *SAE* value was calculated for S21 (107.9 kJ/kg), whereas the lowest value was observed for B12 (31.6 kJ/kg).

For a more detailed analysis and comparison of experimental and numerical results one must refer to related project (Taşdemirci et al. 2014) supported by TÜBİTAK as already mentioned.

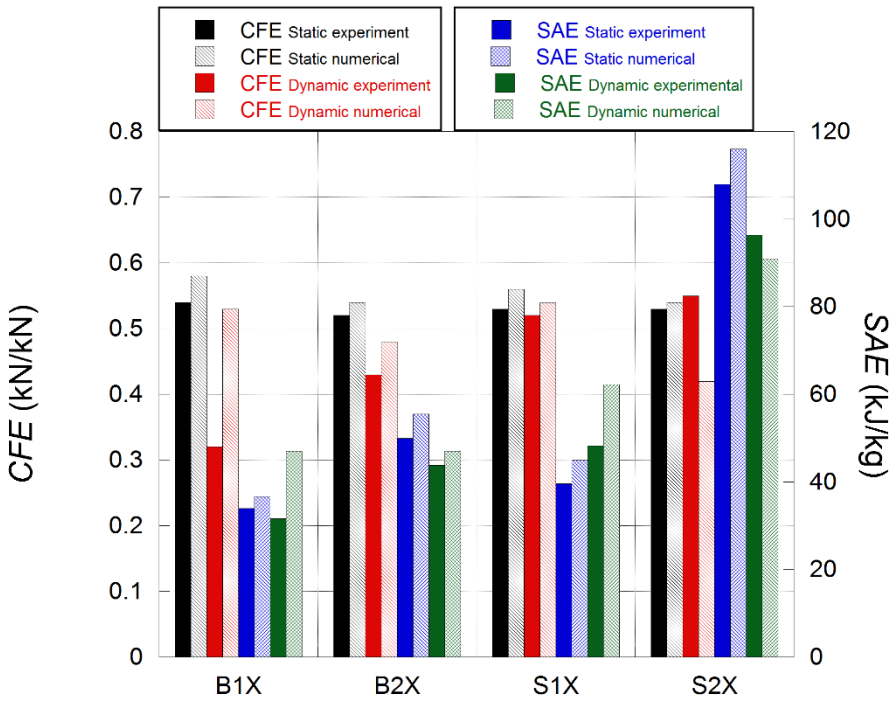

Figure 5.26. *CFE* and *SAE* values of combined geometry shells.

5.2.2. Energy Partitions Between the Hemi-Spherical and Cylindrical Segments.

The energy partitions between the hemi-spherical and cylindrical segments were investigated numerically in terms of the absorbed energies of the both hemi-spherical and cylindrical segments. In current study, the combined geometry shell was divided numerically into two parts i.e.; the hemi-spherical and the cylindrical segments to determine the percentages of energy absorption of each segment. The percentages of energy-deformation curves are given in Figure 5.27.

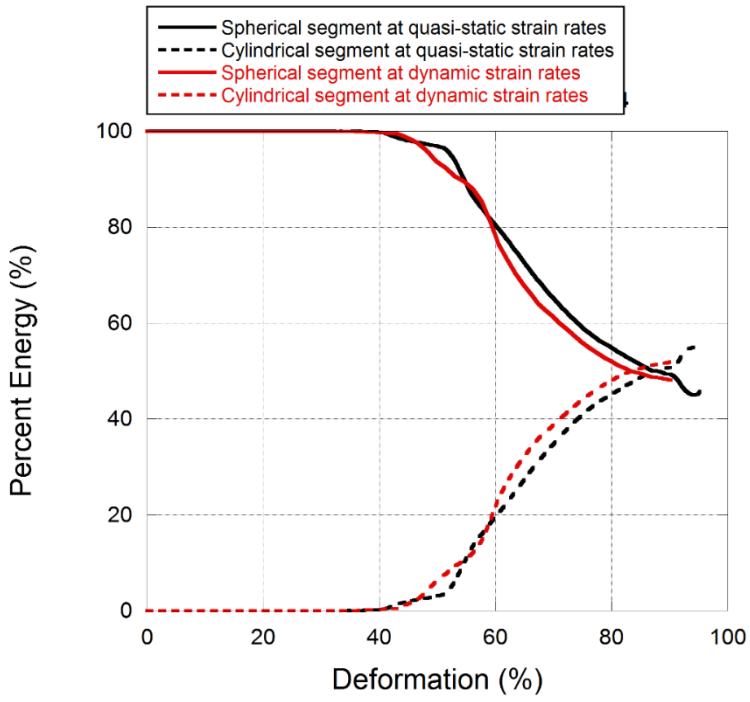

(a)

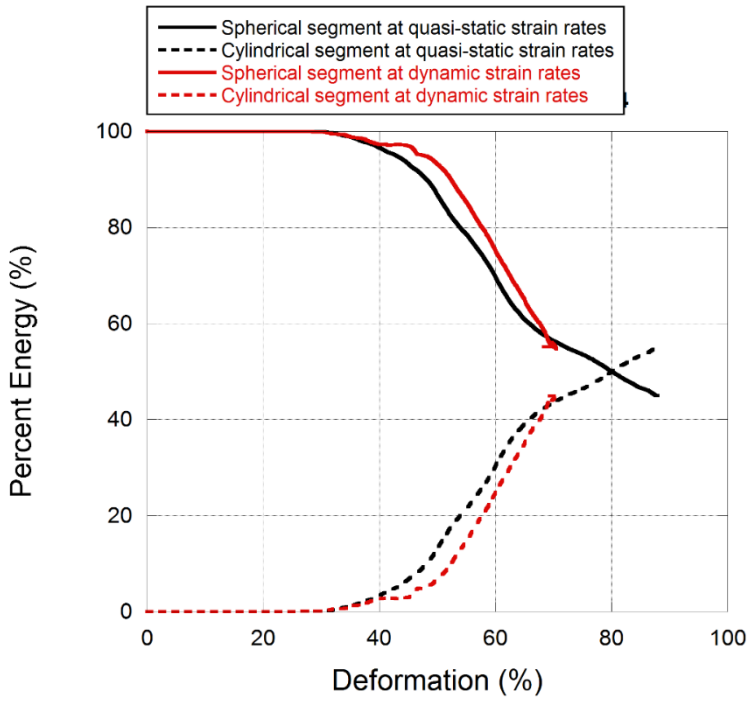

(b)

Figure 5.27. Energy partitions between the hemi-spherical and the cylindrical segments of (a) B1X, (b) B2X, (c) S1X and (d) S2X specimens.

(cont. on next page)

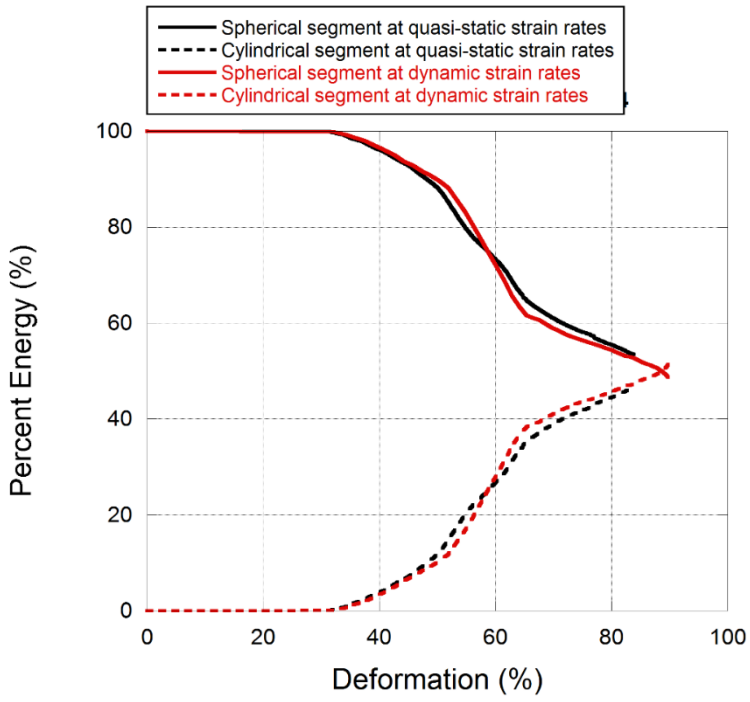

(c)

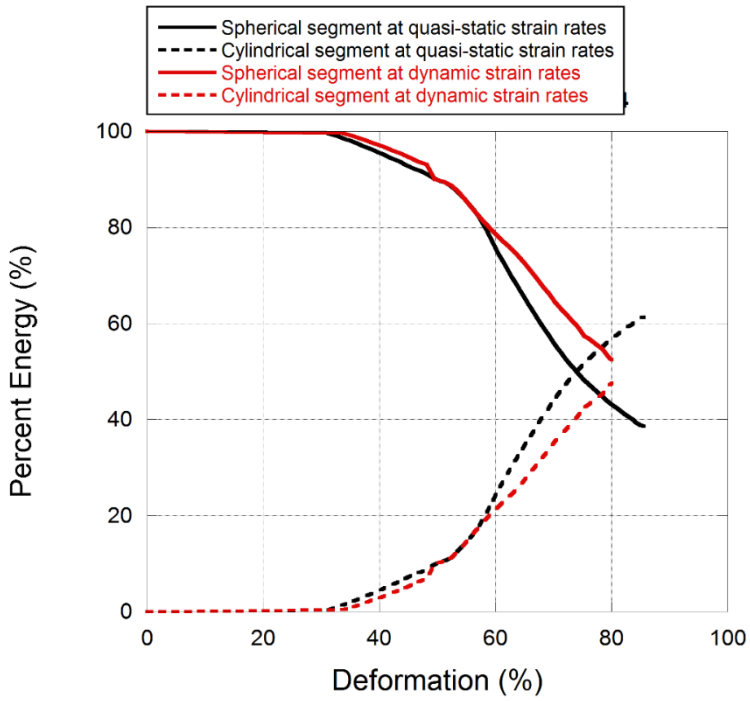

(d)

Figure 5.27. (cont.)

The Figure 5.27.(a) shows that only the hemi-spherical segment absorbed energy up to 40% of a deformation with mode deformation of axisymmetric inward dimpling for both strain rates. When the cylindrical segment started to deform, the absorbed energy was shared by both the hemi-spherical and cylindrical segments. The energy absorption percentage of the cylindrical segment at dynamic strain rate was higher than that of quasi-static strain rate due to the change in deformation mode. The hemi-spherical segment of B2X absorbed energy up to 30%, Figure 5.27.(b). After the failure occurred at 40% of deformation, the energy absorption percentage of the cylindrical segment was remained constant at 45% of deformation. That resulted in lower energy absorption the cylindrical segment at dynamic strain rates at the same deformation levels than that of quasi-static strain rate. The absorbed energies of the hemi-spherical and the cylindrical segment were almost the same at 80% of deformation of B2X at quasi-static strain rate. In Figure 5.27.(c), the increase rate was lower in the range between 30% and 50% of deformation than the range between 50% and 65% of deformation. That was due to the asymmetric deformation of S1X in the cylindrical segments. In addition, the absorbed energy by the hemi-spherical and the cylindrical segment were similar at both quasi-static and dynamic strain rates. The slight differences were due to the failure and different number of lobes formed at the dynamic strain rate. The comparison of energy-deformation curves of S2X is given in Figure 5.27.(d). The energy absorptions at quasi-static and dynamic strain rates were similar in the range between 30% and 55% of deformation. After 55% of deformation, failure was observed at dynamic strain rate. That resulted in lowered energy absorption in the cylindrical segment for the same deformation than that of quasi static strain rate.

5.2.3. Effect of Inertia and Strain Rate on the Crashworthiness of Combined Geometry Shells

The energy absorbing structures can be classified in terms of crushing responses. That the crushing load is a function of displacement like ‘flat-topped’ is classified as Type I and that the crushing load decreases suddenly after peak value is named Type II (Calladine and English 1984). The laterally compression of beam or tubes can be given examples of Type I structures and axially compression of beam or tubes can be example of Type II. The comparison of load-displacement and energy-displacement curves of

Type I and Type II structures are given in Figure 5.28 and 5.29 with the demonstration of the loading direction.

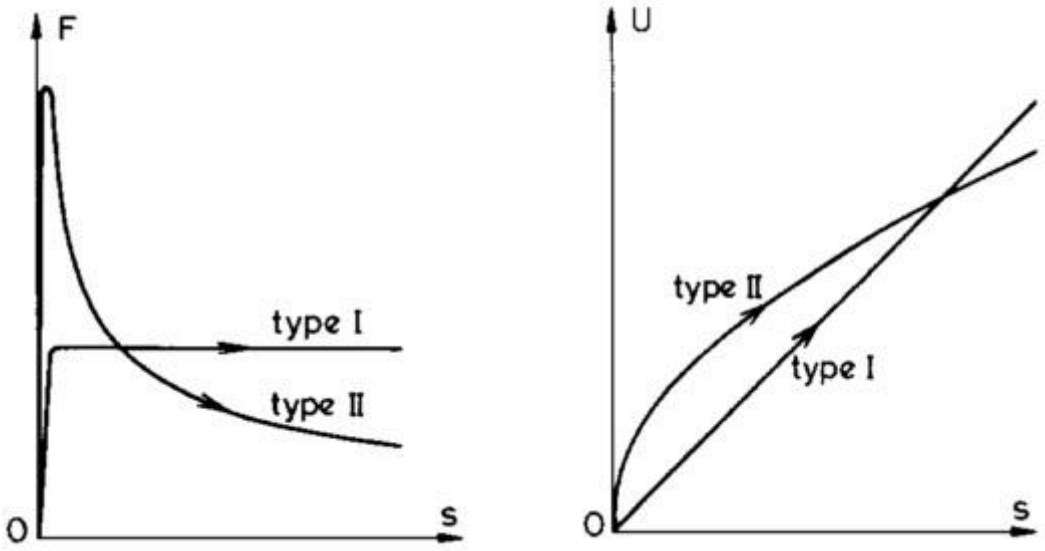

(a) (b)

Figure 5.28. (a) Crushing force and (b) energy absorbing behavior of Type I and Type II structures (Source: Calladine and English 1984).

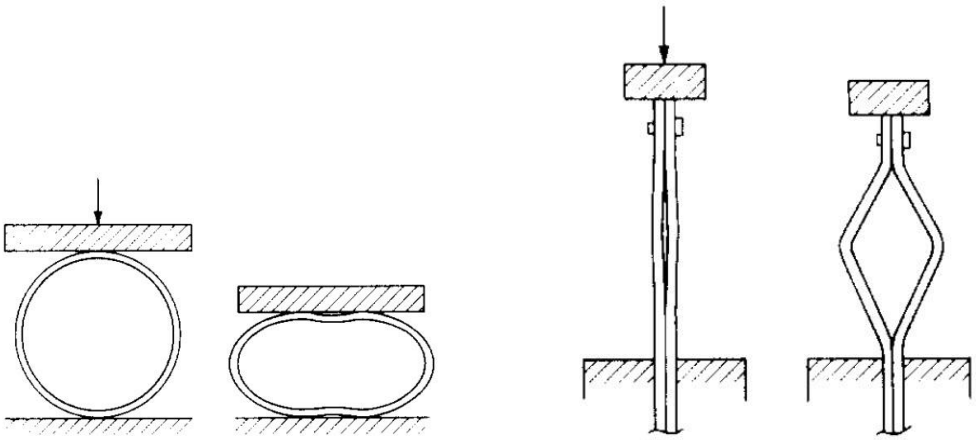

(a) (b)

Figure 5.29. The demonstration of (a) Type I and (b) Type II structures (Source: Calladine and English 1984).

When the crushing responses of a structure at dynamic and quasi-static strain rate is determined, there are two significant effects that need to be considered: strain rate sensitivity and inertia. The rate sensitivity and inertia effects are more pronounced in Type II structures than Type I (Calladine and English 1984) and additionally, the tendency of energy absorption of Type II structures can be increased by the material strain

rate sensitivity (Tam and Calladine 1991). In the current study, the combined geometry shell consists of hemi-spherical segment an example of Type I structure and the cylindrical segment, an example of Type II structure. In order to clarify the increase in the crushing response due to inertia and rate sensitivity, the crushing of structure can be modeled with and without including rate sensitivity parameter in the material model definition at static and dynamic strain rates. The difference between the crushing responses of with and without including rate sensitivity presents an increase in the crushing load due to the rate sensitivity and the difference of the crushing responses of without including rate sensitivity and quasi-static models presents the increase in the crushing load due to the inertial effect. (Taşdemirci, Ergönenç, and Güden 2010).

To investigate the rate sensitivity and the inertia effects, the crushing responses of the combined geometry shell B1X was modeled numerically at varying dynamic loading rate of 50-100 and 160 m/s. The simulations were run without considering any damage options. The load-displacement curves and the increase in the crushing responses due to inertia and strain rate were given in detail as follows.

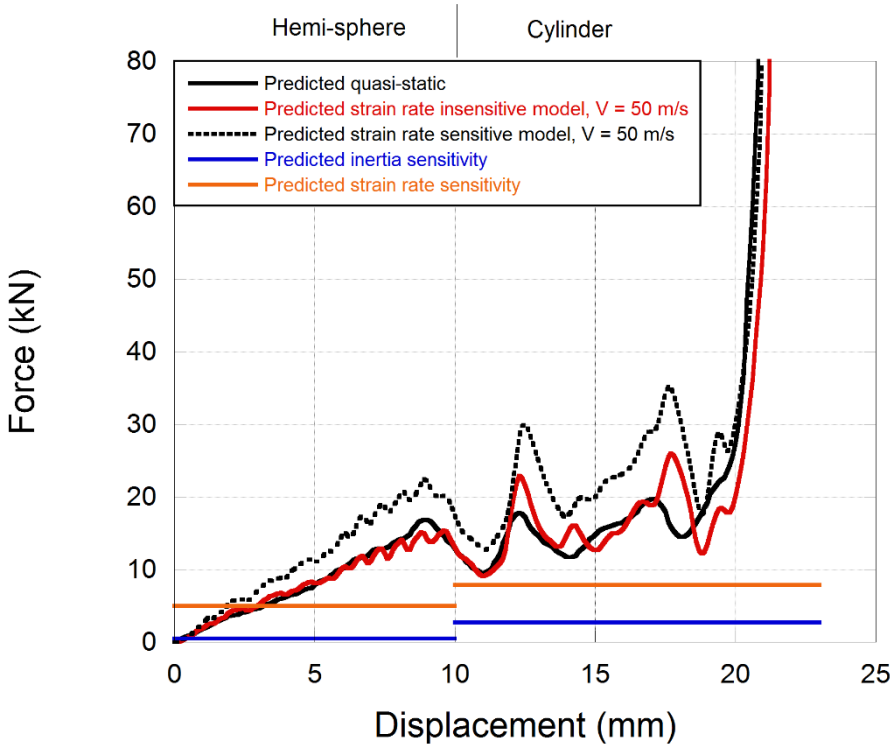

(a)

Figure 5.30. Inertia and strain rate effects for (a) 50 m/s, (b) 100 m/s, (c) 160 m/s velocities.

(cont. on next page)

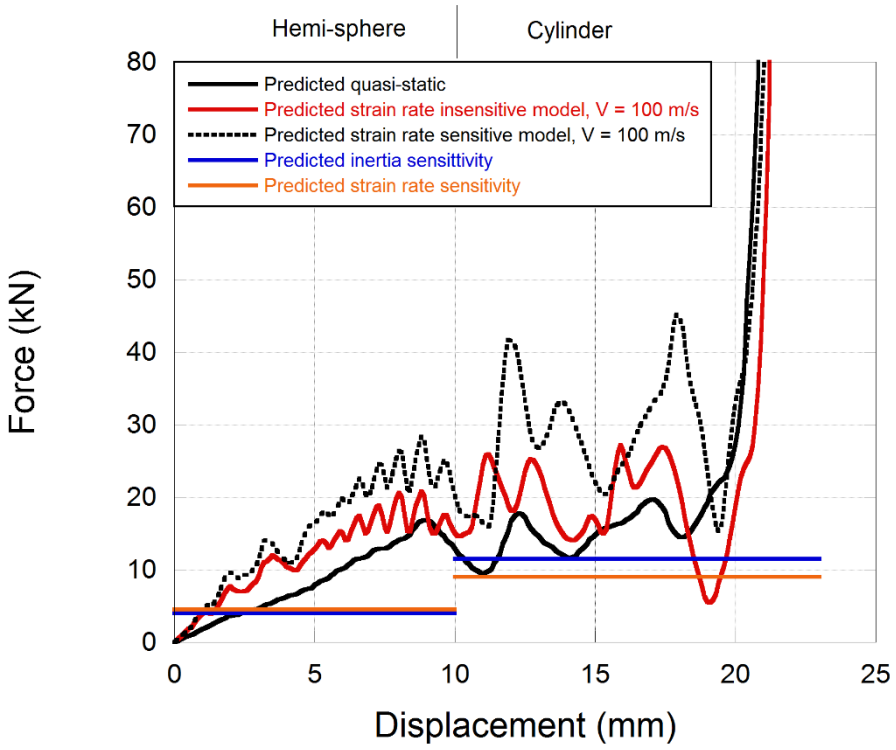

(b)

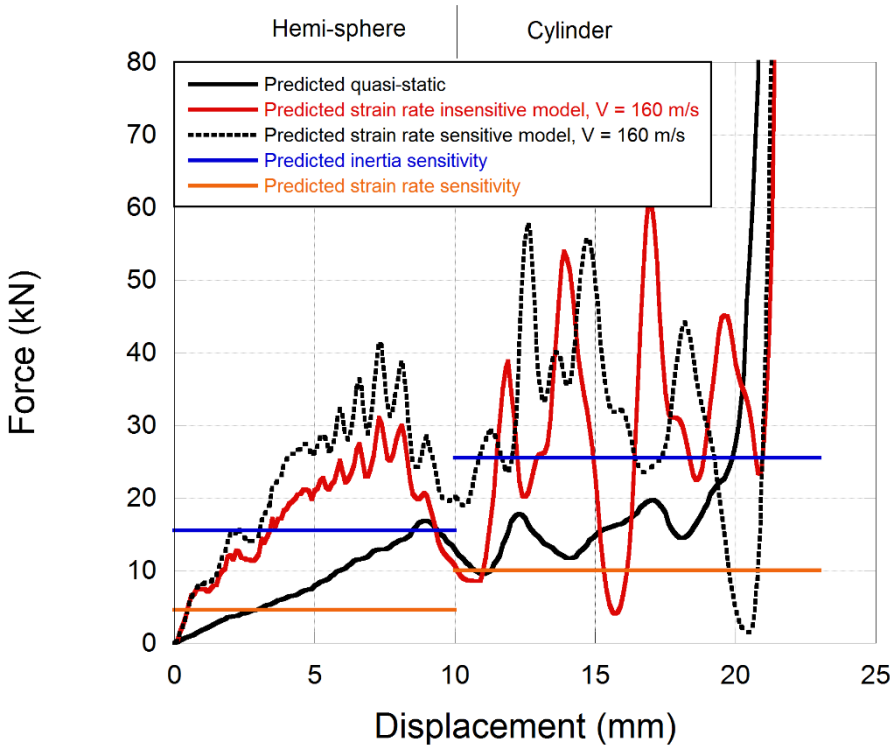

(c)

Figure 5.30. (cont.)

The crushing responses of B1X are given with and without strain rate sensitivity at 50 m/s and quasi-static strain rates in Figure 5.30.(a). The crushing force including strain rate sensitivity was higher than that of without and quasi-static. The average increase in the crushing load was around 5 kN due to the rate sensitivity. In addition, the increase in crushing load due to the inertia effect was not found to be that significant in the hemi-spherical segment at this dynamic loading rate. When the strain rate and inertia effects were both considered, the crushing load with strain rate sensitivity was higher than that of the without and quasi-static strain rate. It was also shown that the crushing load increased predominantly due to the inertia effect in the cylindrical segment than in the hemi-spherical segment. The increase in the crushing load due to the strain rate and inertia were 7.9 kN and 2.7 kN in cylindrical segment.

The crushing responses of B1X with and without strain rate sensitivity at 100 m/s dynamic loading and the quasi-static compression are given in Figure 5.30.(b) with the strain rate sensitivity and inertia. The crushing load with strain rate sensitivity was higher than without and the quasi-static compression in both hemi-spherical and cylindrical segment. The increase in crushing force due to the strain rate sensitivity in cylindrical segment was around twice as much of the hemi-spherical segment.

The crushing responses of B1X with and without including strain rate sensitivity at 160 m/s dynamic loading and the quasi-static compression are given with the contribution of strain rate sensitivity and inertia in Figure 5.30.(c). The increase in the crushing force due to the strain rate sensitivity for cylindrical segment (10.0 kN) was higher than that of the hemi-spherical segment (4.6 kN). The increase in the crushing force due to the inertia was 15.5 kN for the hemi-spherical segment and 25.5 kN for the cylindrical segment.

In Figure 5.31 the increase in crushing load vs. impact velocity is given. The increase in crushing load due to strain rate sensitivity and inertia in the cylindrical segment was always higher than in hemi-spherical segment for all rates. It was due to the tendency of increase in the crushing load of Type II structures was higher than Type I structures. It was also concluded that the rate of increase in the crushing load due to the strain rate sensitivity in the cylindrical segment (Type II) was higher than that of the hemi-spherical segment (Type I). Moreover, the contribution of inertia increased significantly as dynamic loading rate increased. Additionally, the rate of increase in the crushing load was similar in the range between 50 and 140 m/s for both the hemi-spherical and the cylindrical segments. After 140 m/s, the increase rate in the crushing load of cylindrical

segment was higher. According to results, there were critical loading velocities for both constituents at which the contribution of inertia effect becomes higher than the strain rate sensitivity; 80 m/s in the cylindrical segment and 120 m/s for the hemi-spherical segment.

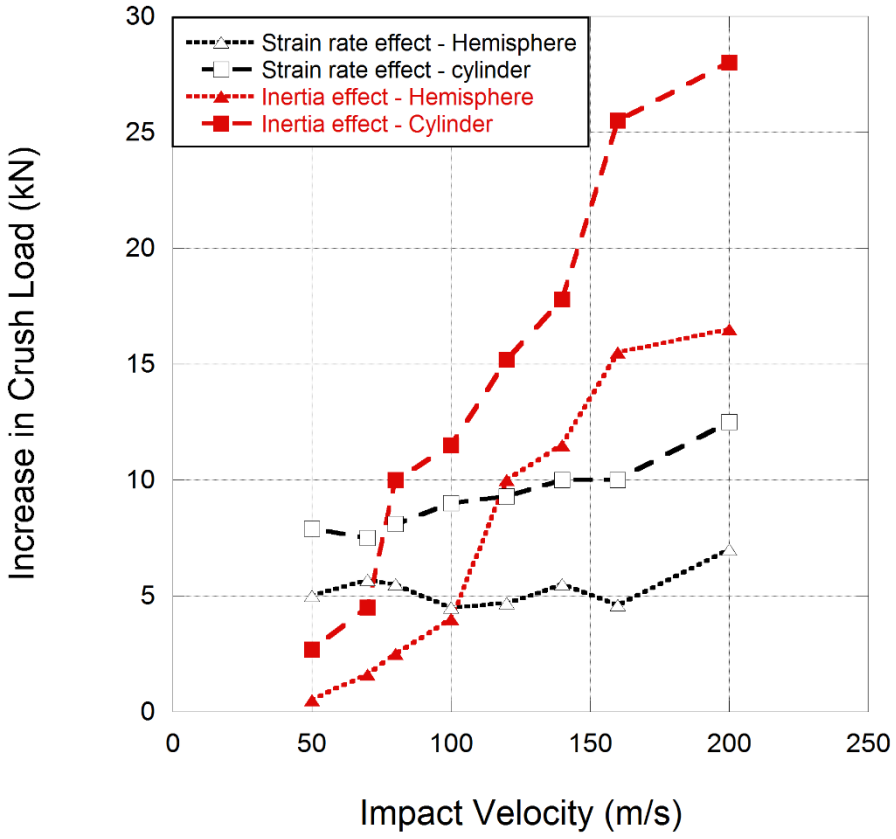

Figure 5.31. Increase in crushing force due to the rate sensitivity and inertia.

The simulations with and without strain rate sensitivity of B1X at a constant energy of 250 J were performed at different impact velocities of 50,100 and 150 m/s. The contributions of the rate sensitivity and inertia were determined in terms of final displacements. The comparison of crushing responses with and without strain rate sensitivity at 50 m/s and the quasi-static strain rate are shown in Figure 5.32. As the final displacement of quasi-static compression was 20 mm, the final displacement of strain rate insensitive model decreased to 19.6 mm due to the inertia effect. It was seen that the final displacement of the rate sensitive model decreased to 16.04 mm due to the strain rate sensitivity. It was concluded that the final displacements of model were reduced as 0.4 mm and 2.7 mm due to the inertia and strain rate sensitivity.

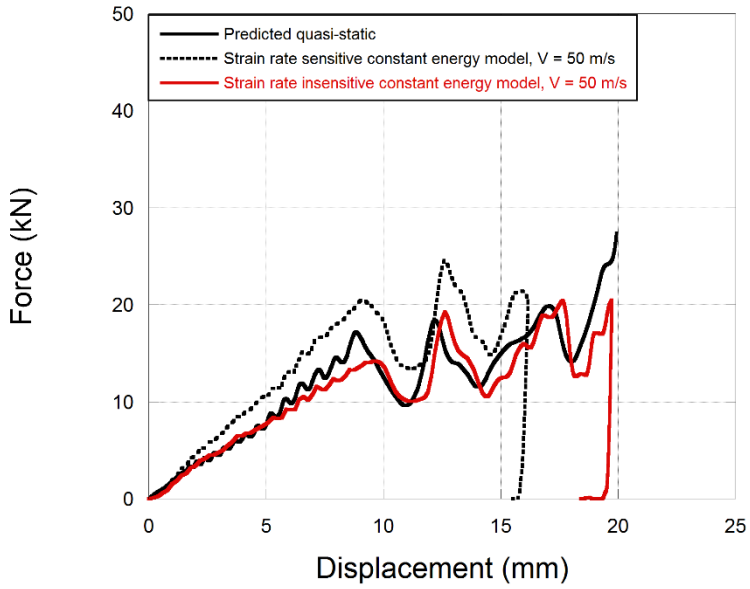

Figure 5.32. Simulations force-displacement curves of quasi-static and the strain rate sensitive and insensitive models at 50 m/s.

The comparison of crushing responses with and without strain rate sensitivity at 100 m/s and the quasi-static compression are given in Figure 5.33. The final displacement of model without the strain rate sensitivity decreased 17.98 mm due to the inertia effect and the final displacement of model with the strain rates sensitivity decreased 14.9 mm due to the strain rate sensitivity. It was resulted that the decrease in final displacements of models were 2.02 mm and 3.08 mm due to the inertia and strain rate sensitivity.

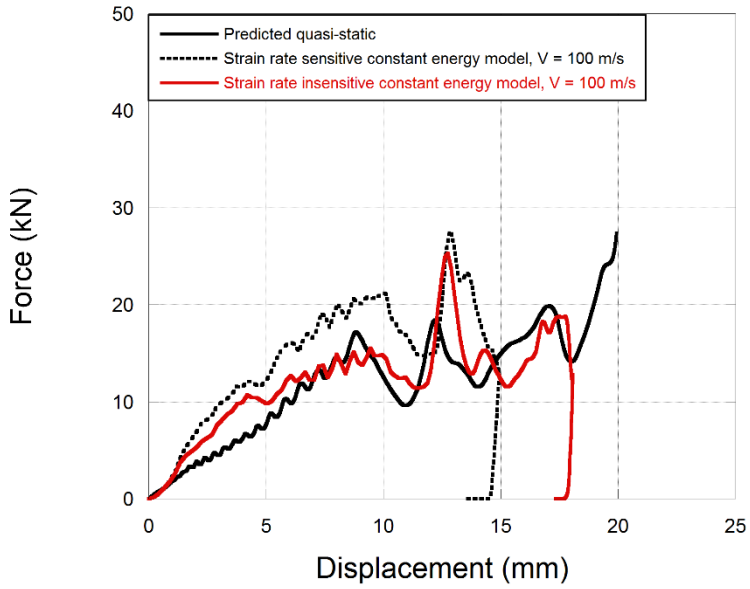

Figure 5.33. Simulations force-displacement curves of quasi-static and the strain rate sensitive and insensitive models at 100 m/s.

The comparison of crushing responses with and without the strain rate sensitivity at 150 m/s and the quasi-static compression are given in Figure 5.34. The final displacement of model without the strain rate sensitivity decreased to 16.5 mm due to the inertia and with the strain rate sensitivity decreased to 13.68 mm. The final displacements of model were reduced as 3.5 mm and 2.82 mm due to the inertia and strain rate sensitivity. It was concluded that, the model with the strain rate sensitivity absorb more energy at the same displacement than the model without and the quasi-static compression as seen in Figure 5. 35. Furthermore, the model without strain rate sensitivity absorbed more energy than the quasi-static compression. The decreases in final displacement values due to the strain rate sensitivity were similar at 50, 100 and 150 m/s dynamic loading. However, the final displacement values decreased depending on the loading velocity.

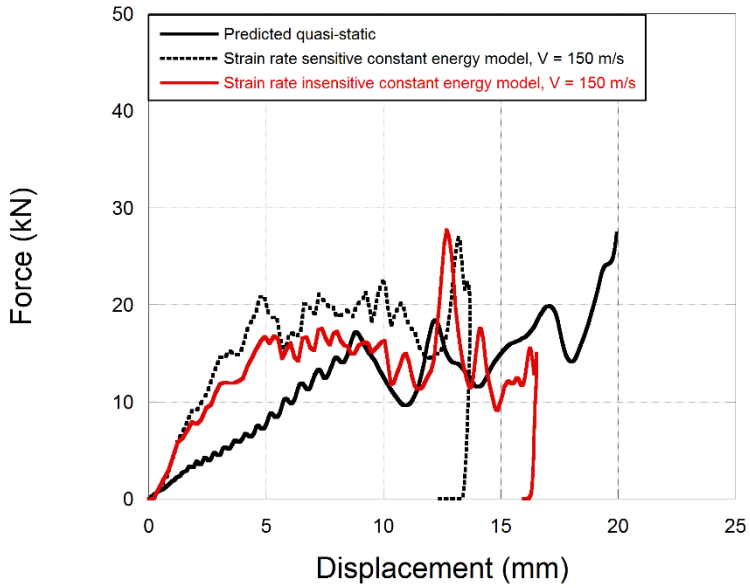

Figure 5.34. Simulations force-displacement curves of quasi-static and the strain rate sensitive and insensitive models at 150 m/s.

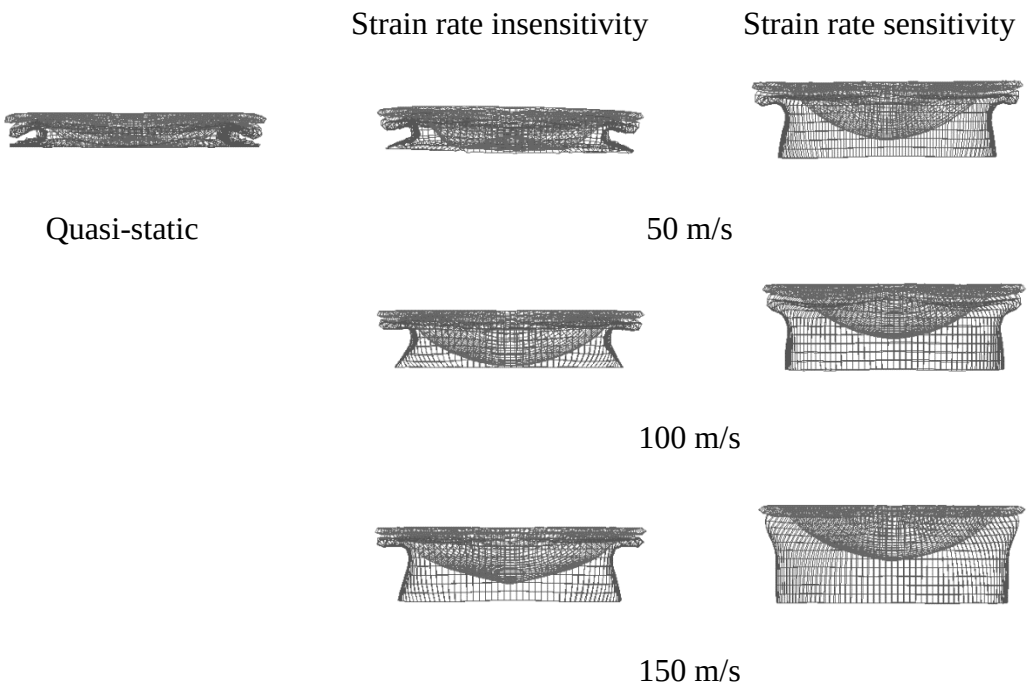

Figure 5.35. Final deformation pictures of constant energy deformation models.

5.2.4. Effect of Temperature on Crushing Behavior of the Combined Geometry Shells

The effect of temperature on the crushing behavior of combined geometry shells was investigated by selection one of the geometric configuration, B1X. The dynamic compression model of B1X was run at 50, 100 and 150 m/s with different temperatures of 298, 673, 1073 and 1473 K. The mean crushing forces are given in Figure 5.36.

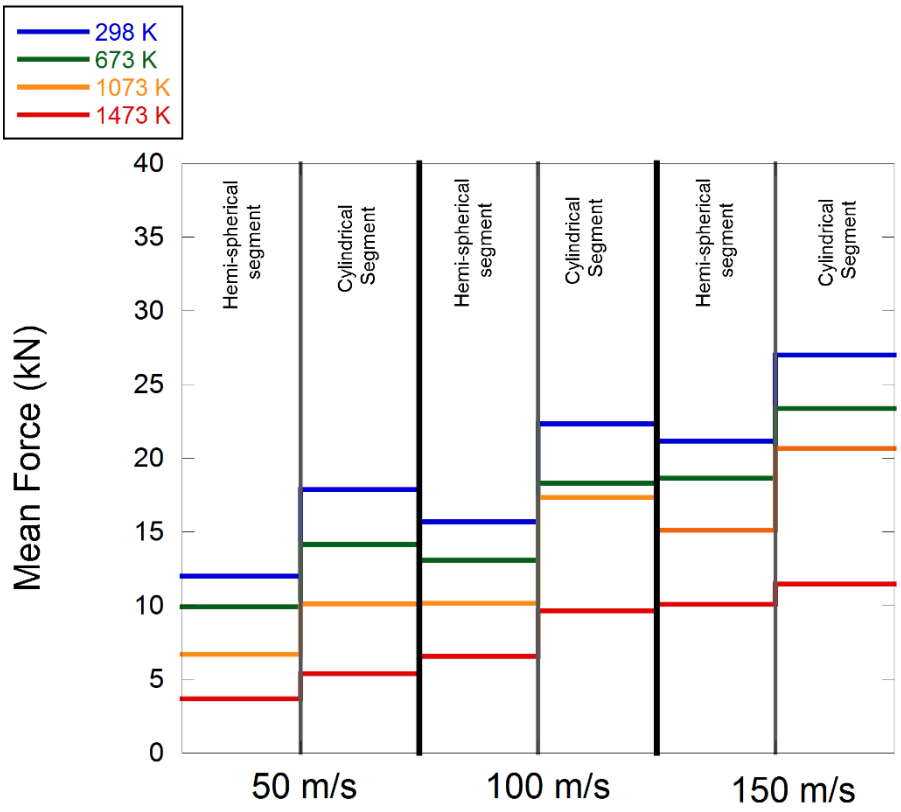

Figure 5.36. The mean crushing forces in the hemi-spherical and the cylindrical segments at various temperatures and loading velocities.

The mean crushing forces of the cylindrical segments were higher those of hemi-spherical at all loading velocities and temperatures. It was seen that the mean crushing force increased as the loading velocity increased. However, the mean crushing force decreased due to the thermal softening as the temperature increased.

The average increase in the mean force of the hemi-spherical segment for different velocities and temperatures are given in Table 5.2. The mean crushing forces at 50 m/s and at 298, 673, 1073 and 1473 K were assumed to be reference values.

Table 5.2. Increase rates in mean crushing forces for various loading velocities in the hemi-spherical segment.

	Loading Velocity (m/s)		
Absolute Temperature (K)	**50**	**100**	**150**
298 K	11.9 kN	32%	77%
673 K	9.9 kN	32%	87%
1073 K	6.7 kN	53%	124%
1473 K	3.7 kN	78%	168%

The mean crushing force increased as the loading velocity increased for all values of temperature. The amount of increase in mean crushing load due to the loading velocity at 298 K and 673 K were similar. However, the amount of increase in mean crushing force due to the loading velocity increased at higher temperatures. That was partly due to the change in deformation mode of specimen. The deformation modes of B1X subjected to 100 m/s at 673-1073-1473 K are given in Figure 5.37. The rolling plastic hinge radius of the hemi-spherical segment decreased at higher temperature for the same loading velocity of 100 m/s.

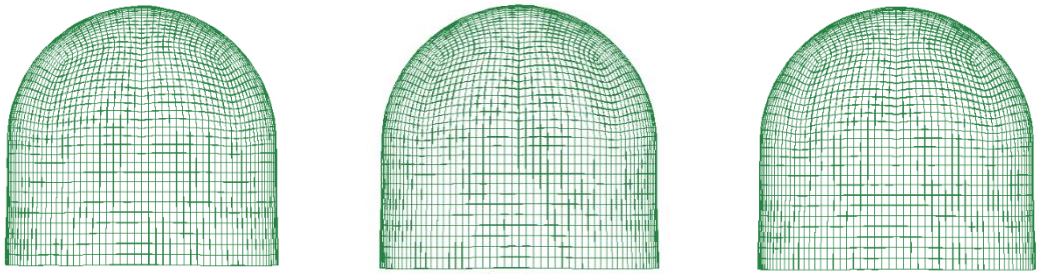

(a)

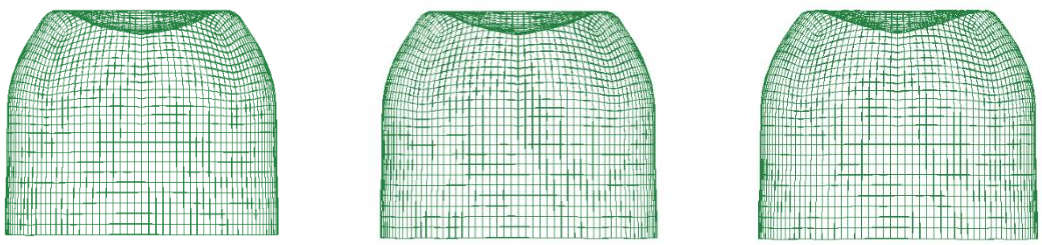

(b)

Figure 5.37. The deformation of B1X at 673, 1073 and 1473 K at (a) 0 mm, (b) 2.85 mm, (c) 4.6 mm, (d) 6.5 mm (e) 11.3 mm, (f) 13.8 mm and (g) 17.8 mm of compressions.

(cont. on next page)

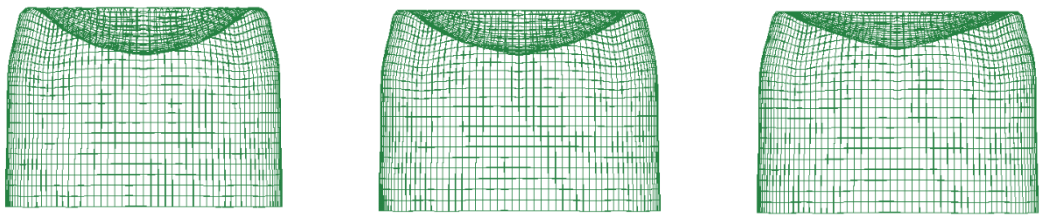

(c)

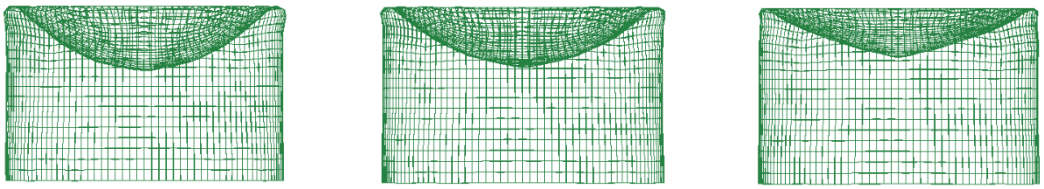

(d)

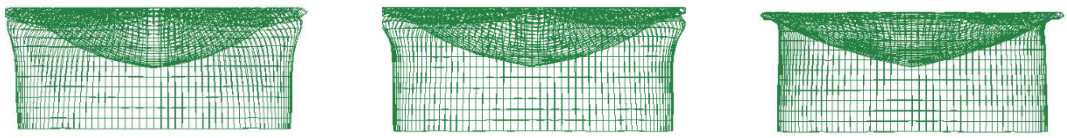

(e)

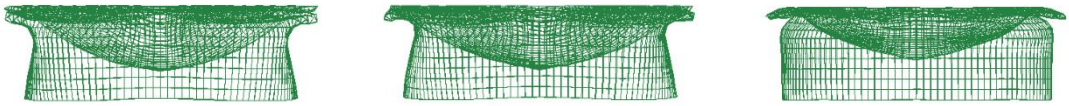

(f)

Figure 5.37 (cont.)

(cont. on next page)

(g)

673 K 1073 K 1473 K

Figure 5.37. (cont.)

5.2.5. Effect of Wall Thickness Variation on the Crushing Behavior of Combined Geometry Shells

In this section, the crushing behavior of combined geometry shells were investigated with various R/t ratios between 25 and 12.5. For this purpose, the combined geometry shells were created numerically in 12.5 mm of radius from 0.6, 0.7, 0.8 and 0.9 mm thick of stainless steel using the deep drawing model.

The thickness distributions of specimens were compared with those of B1X and B2X as seen in Figure 5.38. The specimens were coded as in terms of thickness and coding configurations were named as N06, N07, N08 and N09 where the numbers referred to the thickness of specimens before deep drawing.

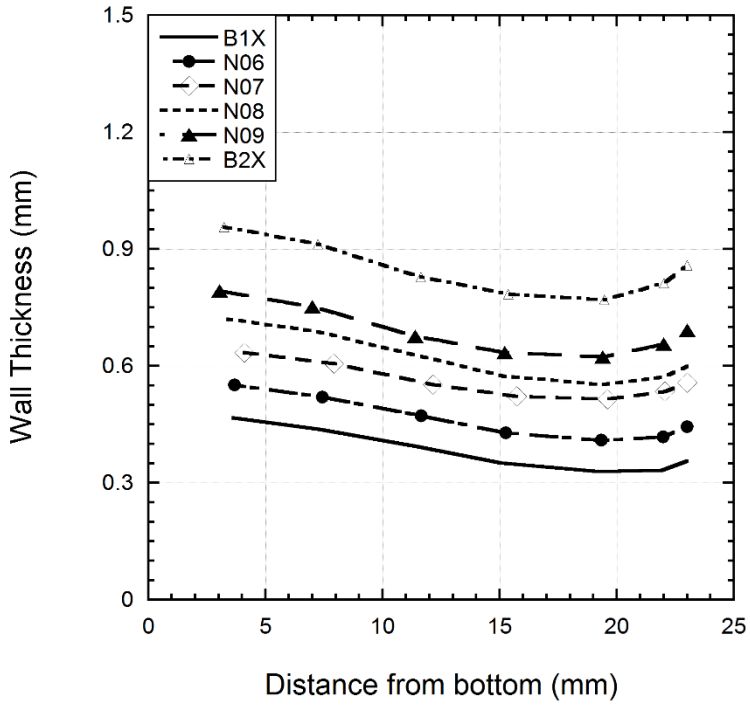

Figure 5.38. Thickness distributions of specimens.

The combined geometry shells were modeled at 50 m/s loading velocity. The load-displacement curves of combined geometry shells are given in Figure 5.39 and the initial peak force, the mean crushing force, the maximum peak force, the *CFE* and *SAE* values were tabulated in Table 5.3. The deformation histories of combined geometry shells at 0, 10, 12, 15, 18 mm are given in Figure 5.40.

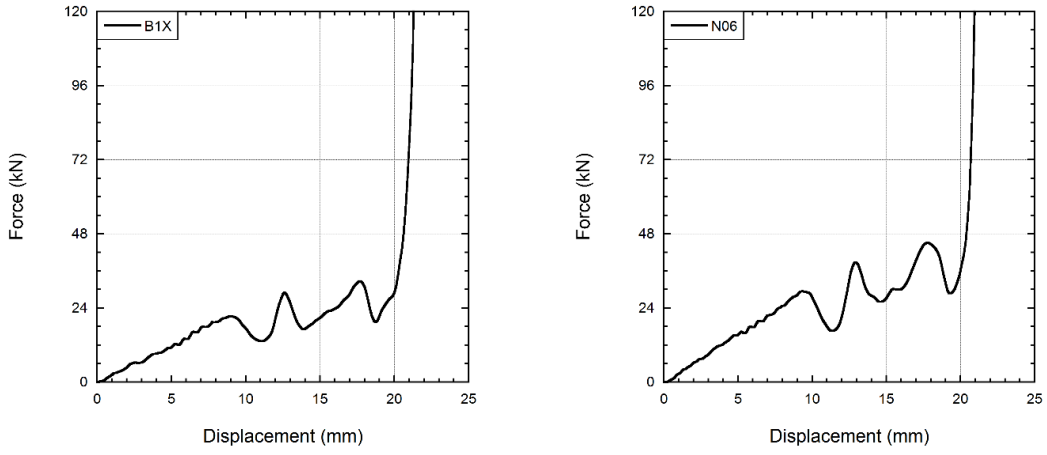

(a) (b)

Figure 5.39. The load-displacement curves of (a) B1X, (b) N06, (c) N07, (d) N08, (e) N09 and (f) B2X specimens.

(cont. on next page)

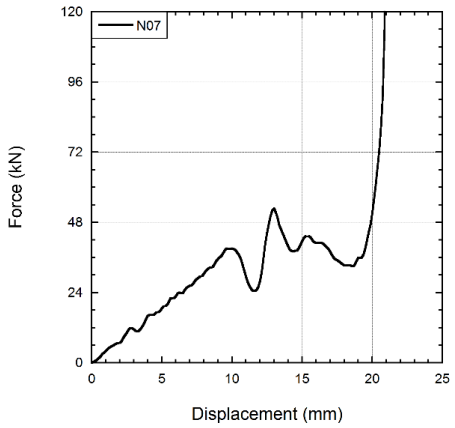

(c)

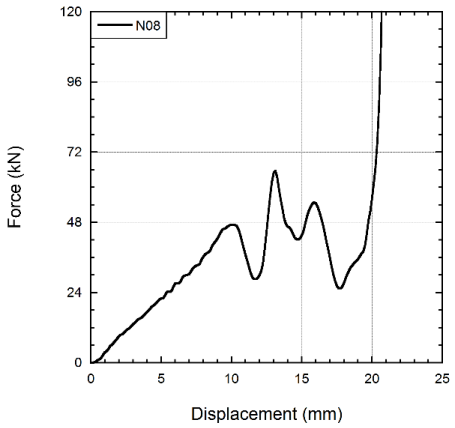

(d)

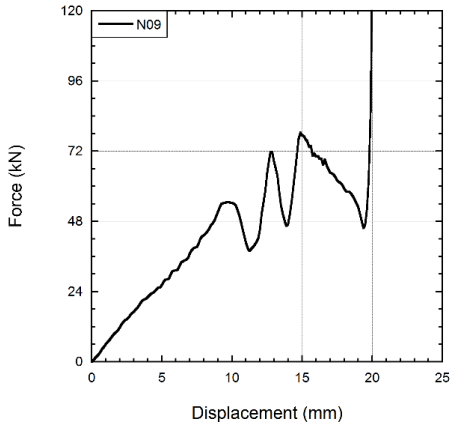

(e)

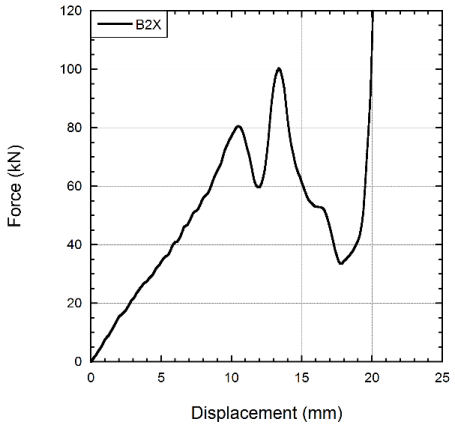

(f)

Figure 5.39. (cont.)

The mean crushing forces increased as the thickness distribution of the specimen increased. The highest and lowest P_{mean} were 50 kN in B2X and 17.7 kN in B1X.

Table 5.3. Dimensional characteristics of specimens at 50 m/s loading velocity.

Specimen	**R/t**	**P_i (kN)**	**P_{max} (kN)**	**P_m (kN)**	**Energy (J)**	***SAE* (kJ/kg)**	***CFE* (kN/kN)**
B1X	25	21.3	33	17.7	360	60	0.537
N06	20.8	29.7	45	23.2	470	71	0.516
N07	17.8	39.1	52.5	29	579	75	0.552
N08	15.6	47.5	65.5	32.3	626	78	0.493
N09	13.8	54.7	78.3	43	854	91	0.549
B2X	12.5	80.6	100	50	940	78	0.5

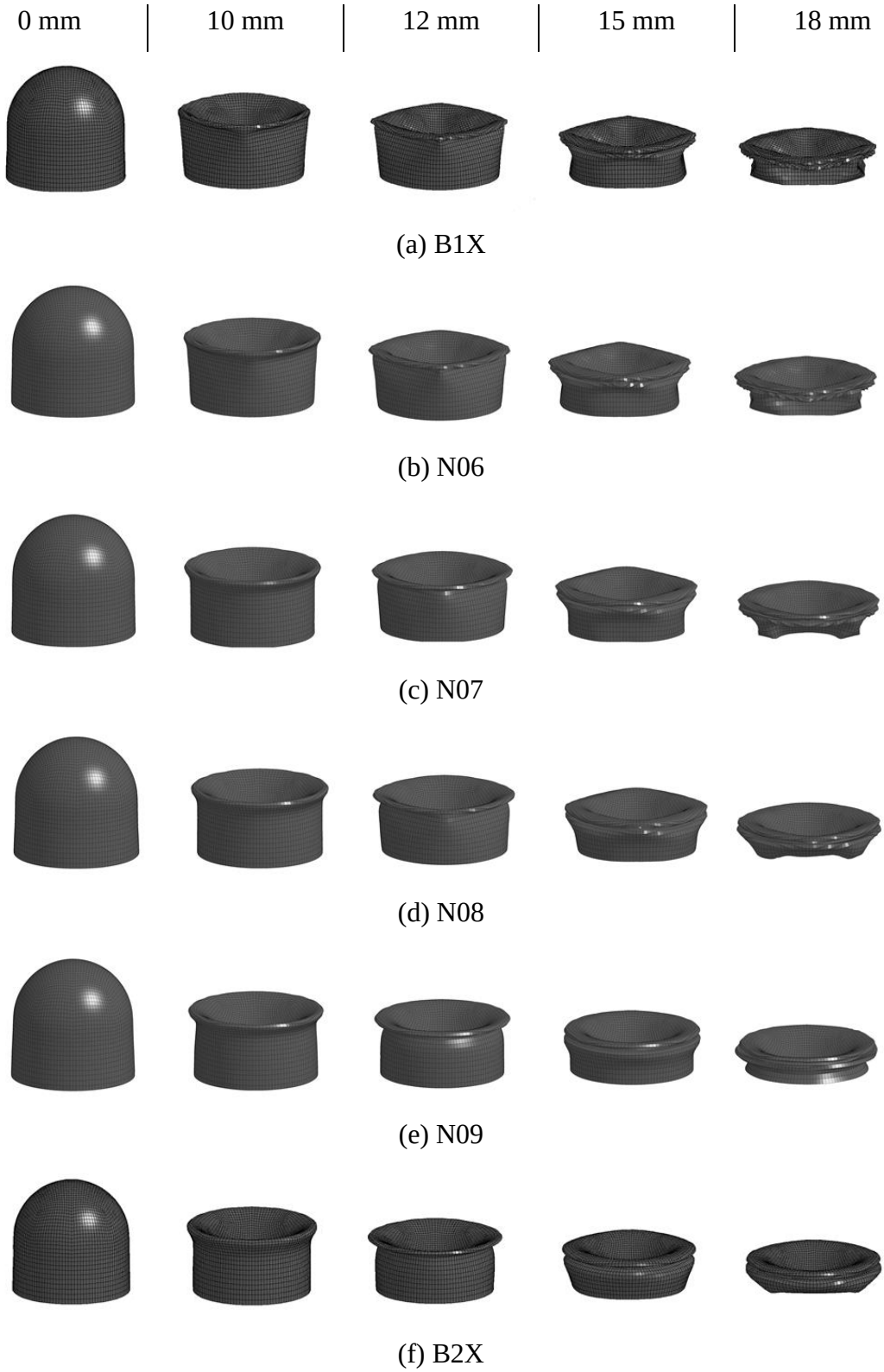

Figure 5.40. The deformation histories of (a) B1X, (b) N06, (c) N07, (d) N08, (e) N09 and (f) B2X specimens at various displacements.

The *SAE* and *CFE* values are given in Figure 5.41. *SAE* values increased as the wall thickness of specimen increased. The highest and the lowest *SAE* values were 91

kJ/kg in N09 and 60 kJ/kg in B1X. The *CFE* values changed depending on the crushing modes of specimens. The highest and the lowest *CFE* values were 0.552 in N07 and 0.493 in N08. Due to the deformation mode changed from asymmetric to axisymmetric in the cylindrical segment, the *CFE* values was calculated minimum at a wall thickness of 0.8 mm.

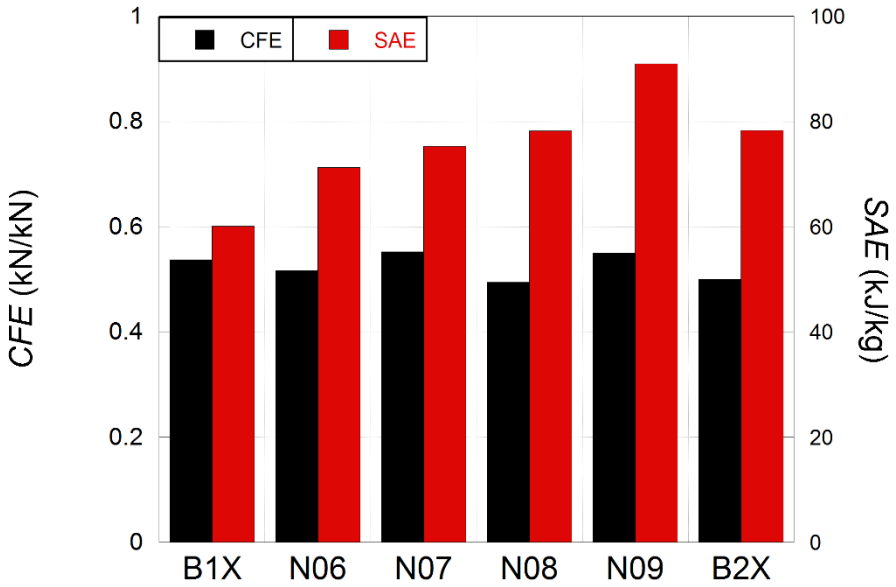

Figure 5.41. *CFE* and *SAE* values of specimens.

CHAPTER 6

CONCLUSIONS

The static and dynamic crushing behaviors of AISI 304L stainless steel combined geometry shells were examined in terms of varying R/t ratios between 7.5-25 and lengths of 13 mm and 23 mm experimentally and numerically in detail.

Based on experimental and numerical observations the following conclusions can be given.

- Having modeled manufacturing process, explicitly numerical crushing behavior of the combined geometry shells correlated well with that of experimental.
- Although the combined geometry shell B1X specimen deformed progressively axisymmetric at quasi-static strain rates with a mode of inward dimpling in the hemi-spherical segment and the formation of folds in the cylindrical segment, the deformation switched to an asymmetric mode in the cylindrical segment with lobe formation at dynamic strain rates and that resulted in the lower crushing loads.
- As R/t ratios decreased with constant thickness, P_i, P_{max} and P_{mean} decreased, however *SAE* values increased at both quasi-static and dynamic strain rates. In addition to this, as R/t decreased for the same radius, P_i, P_{max} and P_{mean} increased and so did *SAE*.
- At quasi-static strain rate levels, all specimens deformed progressively without any failure occurred. However; at dynamic strain rates, failure was observed for B2X and S2X specimens at the junction of the hemi-spherical and the cylindrical segments due to the reduced plastic failure strain at higher strain rates.
- *CFE* values were at almost similar levels quasi-static strain rates for all the specimens. As strain rate increased, *CFE* values decreased for B1X and B2X. There was no significant change in the *CFE* values of S1X specimen, while *CFE* values increased for S2X specimen.

- As R/t values decreased at quasi-static strain rates, *SAE* values increased. In addition, *SAE* values decreased as strain rates increased, but S1X.
- When the energy partitions between the hemi-spherical and the cylindrical segments at quasi-static and dynamic strain rates were considered, the absorbed energy in the hemi-spherical segment increased as the loading rate increased. The energy absorption started at the hemi-spherical segment approximately at 40%. It was observed that the combined geometry shells deformed in a progressive mode.
- At increasing strain rate levels, the increase in crushing load due to the inertia was higher than that of rate sensitivity.
- For constant impact energy, the final deformed length of the specimen increased as the impact velocity increased.
- As the temperature increased, the decrease in the crushing force levels was noted.
- When the mean crushing loads were taken as reference at 50 m/s and at 298, 673, 1073 and 1473 K, the increase in mean crushing force was the same at 298 K and 673 K as the impact velocity increased. Nevertheless, after 1073 K, the higher increase rate in mean crushing force was noted due to the change in deformation mode.
- As the wall thickness of the combined geometry shells increased, the *SAE* values increased. Due to the deformation mode change from asymmetric to axisymmetric, the minimum value of *CFE* was observed at a wall thickness 0.8.

REFERENCES

Abosbaia, A. A. S., E. Mahdi, A. M. S. Hamouda, and B. B. Sahari. 2003. "Quasi-static axial crushing of segmented and non-segmented composite tubes." *Composite Structures* 60 (3):327-343. doi: 10.1016/s0263-8223(02)00341-0.

Abosbaia, A. S., E. Mahdi, A. M. S. Hamouda, B. B. Sahari, and A. S. Mokhtar. 2005. "Energy absorption capability of laterally loaded segmented composite tubes." *Composite Structures* 70 (3):356-373. doi: 10.1016/j.compstruct.2004.08.039.

Ahmad, Zaini, and David P Thambiratnam. 2009. "Dynamic computer simulation and energy absorption of foam-filled conical tubes under axial impact loading." *Computers & Structures* 87 (3):186-197.

Al Galib, D., and A. Limam. 2004. "Experimental and numerical investigation of static and dynamic axial crushing of circular aluminum tubes." *Thin-Walled Structures* 42 (8):1103-1137. doi: 10.1016/j.tws.2004.03.001.

Alkateb, M., E. Mahdi, A. M. S. Hamouda, and M. M. Hamdan. 2004. "On the energy absorption capability of axially crushed composite elliptical cones." *Composite Structures* 66 (1-4):495-501. doi: 10.1016/j.compstruct.2004.04.078.

Alysson L. Vieira, Bruno C. Pockszevnicki, Evandro Q. N. Vera, Danilo R. de, and Márcio E. Silveira Mesquita. 2010. "Hardening and final thickness data in the quasi-static nonlinear analysis of stamping parts." *Mecánica Computacional* XXIX:1913-1924.

Atas, Cesim, and Cenk Sevim. 2010. "On the impact response of sandwich composites with cores of balsa wood and PVC foam." *Composite Structures* 93 (1):40-48. doi: 10.1016/j.compstruct.2010.06.018.

Bao, R. H., and T. X. Yu. 2013. "Impact Crushing and Rebound of Thin-walled Hollow Spheres." *Advances in Engineering Plasticity Xi* 535-536:40-43. doi: DOI 10.4028/www.scientific.net/KEM.535-536.40.

Bottcher, CS, and Steffen Frik. 2003. "Consideration of manufacturing effects to improve crash simulation accuracy." 4th European LS-Dyna users conference.

Cafolla, Janka, Roger W Hall, David P Norman, Iain J McGregor, Corus Automotive, and Siskin Parkway East. 2003. "Forming to crash simulation in full vehicle models." Proc. 4th European LS-DYNA Users Conference DYNAmore GmbH pp. E-11-17–E-11-26.

Calladine, CR, and RW English. 1984. "Strain-rate and inertia effects in the collapse of two types of energy-absorbing structure." *International Journal of Mechanical Sciences* 26 (11):689-701.

Dadrasi, Ali. 2011. "Energy absorption of semi-spherical shells under axial loading." *Australian journal of basic and applied sciences* 5 (11):2052-2058.

Deoliveira, J. G., and T. Wierzbicki. 1982. "Crushing Analysis of Rotationally Symmetric Plastic Shells." *Journal of Strain Analysis for Engineering Design* 17 (4):229-236. doi: Doi 10.1243/03093247v174229.

Doğan, Uluğ Çağrı. 2009. "Effect of strain history on simulation of crashworthiness of a vehicle " Master of Science, Mechanical Engineering, Middle East Technical University.

Dong, X. L., Z. Y. Gao, and T. Yu. 2008. "Dynamic crushing of thin-walled spheres: An experimental study." *International Journal of Impact Engineering* 35 (8):717-726. doi: DOI 10.1016/j.ijimpeng.2007.11.004.

Duarte, Isabel, Matej Vesenjak, Lovre Krstulović-Opara, and Zoran Ren. 2015. "Static and dynamic axial crush performance of in-situ foam-filled tubes." *Composite Structures* 124:128-139. doi: 10.1016/j.compstruct.2015.01.014.

Ghamarian, A., and M. T. Abadi. 2011. "Axial crushing analysis of end-capped circular tubes." *Thin-Walled Structures* 49 (6):743-752. doi: DOI 10.1016/j.tws.2011.01.006.

Goel, Manmohan Dass. 2015. "Deformation, energy absorption and crushing behavior of single-, double- and multi-wall foam filled square and circular tubes." *Thin-Walled Structures* 90:1-11. doi: 10.1016/j.tws.2015.01.004.

Guden, M., S. Yüksel, A. Taşdemirci, and M. Tanoğlu. 2007. "Effect of aluminum closed-cell foam filling on the quasi-static axial crush performance of glass fiber reinforced polyester composite and aluminum/composite hybrid tubes." *Composite Structures* 81 (4):480-490. doi: 10.1016/j.compstruct.2006.09.005.

Gupta, N. K., N. Mohamed Sheriff, and R. Velmurugan. 2008. "Analysis of collapse behaviour of combined geometry metallic shells under axial impact." *International Journal of Impact Engineering* 35 (8):731-741. doi: 10.1016/j.ijimpeng.2008.01.005.

Gupta, N. K., N. M. Sheriff, and R. Velmurugan. 2007. "Experimental and numerical investigations into collapse behaviour of thin spherical shells under drop hammer impact." *International Journal of Solids and Structures* 44 (10):3136-3155. doi: DOI 10.1016/j.ijsolstr.2006.09.014.

Gupta, N. K., N. M. Sheriff, and R. Velmurugan. 2008. "Experimental and theoretical studies on buckling of thin spherical shells under axial loads." *International Journal of Mechanical Sciences* 50 (3):422-432. doi: DOI 10.1016/j.ijmecsci.2007.10.002.

Gupta, N. K., and Venkatesh. 2004. "Experimental and numerical studies of dynamic axial compression of thin walled spherical shells." *International Journal of Impact Engineering* 30 (8-9):1225-1240. doi: DOI 10.1016/j.ijimpeng.2004.03.009.

Gupta, P. K. 2011. "Axial Compression Of Tubular Metallic Shells having combined tube-frusta geometry." International Conference on Structural Engineering, Construction and Management (ICSECM-2011), Sri Lanka.

Gupta, P. K., and N. K. Gupta. 2009. "A study of axial compression of metallic hemispherical domes." *Journal of Materials Processing Technology* 209 (4):2175-2179. doi: 10.1016/j.jmatprotec.2008.05.004.

Gupta, P. K., and N. K. Gupta. 2013. "A study on axial compression of tubular metallic shells having combined tube–cone geometry." *Thin-Walled Structures* 62:85-95. doi: 10.1016/j.tws.2012.07.018.

HIGUCHI, Masahiro, Yasuji HAMAGUCHI, Shun SUZUKI, and Tadaharu ADACHI. 2012. "Dynamic Behavior of Circular Tubes Subjected to High Impact Loading." *実験力学* 12 (Special_Issue):s127-s132.

Hodowany, J, G Ravichandran, AJ Rosakis, and P Rosakis. 2000. "Partition of plastic work into heat and stored energy in metals." *Experimental Mechanics* 40 (2):113-123.

Hoek, Tristan van. 2006. "The History Influence of Forming on the Predicted Crash Performance of a Truck Bumper." M.Sc., Department of Mechanical Engineering, Eindhoven University of Technology.

Hong, Wu, Hualin Fan, Zhicheng Xia, Fengnian Jin, Qing Zhou, and Daining Fang. 2014. "Axial crushing behaviors of multi-cell tubes with triangular lattices." *International Journal of Impact Engineering* 63:106-117.

Karagiozova, D, M Alves, and Norman Jones. 2000. "Inertia effects in axisymmetrically deformed cylindrical shells under axial impact." *International Journal of Impact Engineering* 24 (10):1083-1115.

Kathiresan, M., K. Manisekar, and V. Manikandan. 2014. "Crashworthiness analysis of glass fibre/epoxy laminated thin walled composite conical frusta under axial compression." *Composite Structures* 108:584-599. doi: 10.1016/j.compstruct.2013.09.060.

Kılıçaslan, Cenk, Mustafa Güden, İsmet Kutlay Odacı, and Alper Taşdemirci. 2014. "Experimental and numerical studies on the quasi-static and dynamic crushing responses of multi-layer trapezoidal aluminum corrugated sandwiches." *Thin-Walled Structures* 78:70-78. doi: 10.1016/j.tws.2014.01.017.

Krusper, Aleksandra. 2003. Influences of the Forming Process on the Crash Performance - Finite Element Analysis. Department of Structural Mechanics Chalmers University of Technology and Volvo Car Corporation.

Lee, S, F Barthelat, JW Hutchinson, and HD Espinosa. 2006. "Dynamic failure of metallic pyramidal truss core materials–experiments and modeling." *International Journal of Plasticity* 22 (11):2118-2145.

Leinster, J. C., J. Newell, A. Jennings, and A. N. Kinkead. 1994. "Spherical shells in inelastic collision with a rigid wall—tentative analysis and recent quasi-static testing." *The Journal of Strain Analysis for Engineering Design* 29 (1):17-41. doi: 10.1243/03093247v291017.

Liu, Jiagui, Stéphane Pattofatto, Daining Fang, Fangyun Lu, and Han Zhao. 2014. "Impact strength enhancement of aluminum tetrahedral lattice truss core structures." *International Journal of Impact Engineering*.

Mahdi, E., B. S. Almabrouk, A. M. S. Hamouda, A. S. Mokhtar, Robiah Younus, and H. Sultan. 2006. "Utilization of composite's tensile properties for energy absorbing systems." *Composite Structures* 75 (1-4):29-38. doi: 10.1016/j.compstruct.2006.04.081.

Maker, Bradley N, and Xinhai Zhu. 2000. "Input parameters for metal forming simulation using LS-DYNA." *Livermore Software Technology Corporation* 4:43-46.

Mamalis, A. G., D. E. Manolakos, M. B. Ioannidis, and D. P. Papapostolou. 2006. "The static and dynamic axial collapse of CFRP square tubes: Finite element modelling." *Composite Structures* 74 (2):213-225. doi: 10.1016/j.compstruct.2005.04.006.

Obradovic, Jovan, Simonetta Boria, and Giovanni Belingardi. 2012. "Lightweight design and crash analysis of composite frontal impact energy absorbing structures." *Composite Structures* 94 (2):423-430. doi: 10.1016/j.compstruct.2011.08.005.

Ruan, H. H., Z. Y. Gao, and T. X. Yu. 2006. "Crushing of thin-walled spheres and sphere arrays." *International Journal of Mechanical Sciences* 48 (2):117-133. doi: DOI 10.1016/j.ijmecsci.2005.08.006.

Santosa, Sigit P, Tomasz Wierzbicki, Arve G Hanssen, and Magnus Langseth. 2000. "Experimental and numerical studies of foam-filled sections." *International Journal of Impact Engineering* 24 (5):509-534.

Serope Kalpakjian, Stephen Schmid. 2009. *Manufacturing Engineering and Technology*.

Shahi, V. J., and J. Marzbanrad. 2012. "Analytical and experimental studies on quasi-static axial crush behavior of thin-walled tailor-made aluminum tubes." *Thin-Walled Structures* 60:24-37. doi: DOI 10.1016/j.tws.2012.05.015.

Shojaeefard, M. H., A. Najibi, M. Anbarloei, and M. Yeganeh. 2014. "Experimental and numerical crashworthiness investigation of combined circular and square sections." *Journal of Mechanical Science and Technology* 28 (3):999-1006. doi: DOI 10.1007/s12206-013-1172-x.

Singace, A. A., and H. El-Sobky. 2001. "Uniaxial crushing of constrained tubes." *Proceedings of the Institution of Mechanical Engineers Part C-Journal of Mechanical Engineering Science* 215 (3):353-364. doi: Doi 10.1243/0954406011520760.

Sturt, Richard, Paul Richardson, Andrew Knight, and Trevor Dutton. 2001. "Residual effects of metal forming: their effect on crash results." PROCEEDINGS OF 17TH INTERNATIONAL TECHNICAL CONFERENCE ON THE ENHANCED SAFETY OF VEHICLES. CD ROM.

Tam, LL, and CR Calladine. 1991. "Inertia and strain-rate effects in a simple plate-structure under impact loading." *International Journal of Impact Engineering* 11 (3):349-377.

Tasdemirci, A. 2008. "The effect of tube end constraining on the axial crushing behavior of an aluminum tube." *Materials & Design* 29 (10):1992-2001. doi: DOI 10.1016/j.matdes.2008.04.011.

Tasdemirci, A., G. Tunusoglu, and M. Güden. 2012. "The effect of the interlayer on the ballistic performance of ceramic/composite armors: Experimental and numerical study." *International Journal of Impact Engineering* 44:1-9. doi: 10.1016/j.ijimpeng.2011.12.005.

Tasdemirci, A., A. K. Turan, and M. Guden. 2012. "The effect of strain rate on the mechanical behavior of Teflon foam." *Polymer Testing* 31 (6):723-727. doi: 10.1016/j.polymertesting.2012.05.004.

Tasdemirci, Alper, Selim Sahin, Ali Kara, and Kivanc Turan. 2015. "Crushing and energy absorption characteristics of combined geometry shells at quasi-static and dynamic strain rates: Experimental and numerical study." *Thin-Walled Structures* 86:83-93. doi: 10.1016/j.tws.2014.09.020.

Taşdemirci, A., Ç Ergönenç, and M. Güden. 2010. "Split Hopkinson pressure bar multiple reloading and modeling of a 316 L stainless steel metallic hollow sphere structure." *International Journal of Impact Engineering* 37 (3):250-259. doi: 10.1016/j.ijimpeng.2009.06.010.

Taşdemirci, Alper, Mustafa Güden, Ali Kara, Kıvanç Turan, and Selim Şahin. 2014. Development and optimization of blast-resistant hemi-spherical core sandwich structures. Turkey:The Scientific and Technological Research Council of Turkey (TÜBİTAK).

Updike, D. P. 1972. "On the Large Deformation of a Rigid-Plastic Spherical Shell Compressed by a Rigid Plate." *Journal of Manufacturing Science and Engineering* 94 (3):949-955. doi: 10.1115/1.3428276.

Wadley, Haydn, Kumar Dharmasena, Yungchia Chen, Philip Dudt, David Knight, Robert Charette, and Kenneth Kiddy. 2008. "Compressive response of multilayered pyramidal lattices during underwater shock loading." *International Journal of Impact Engineering* 35 (9):1102-1114.

Welbes, John. 2008. "FAA: NWA jet damage was 'structural failure'." http://www.twincities.com/ci_9818109?source=most_viewed.

Zhang, Guoqi, Bing Wang, Li Ma, Linzhi Wu, Shidong Pan, and Jinshui Yang. 2014. "Energy absorption and low velocity impact response of polyurethane foam filled pyramidal lattice core sandwich panels." *Composite Structures* 108:304-310.

Zhang, Xiong, and Hoon Huh. 2010. "Crushing analysis of polygonal columns and angle elements." *International Journal of Impact Engineering* 37 (4):441-451. doi: 10.1016/j.ijimpeng.2009.06.009.

Zhang, Xiong, Hui Zhang, and Zhuzhu Wen. 2014. "Experimental and numerical studies on the crush resistance of aluminum honeycombs with various cell configurations." *International Journal of Impact Engineering* 66:48-59. doi: 10.1016/j.ijimpeng.2013.12.009.